Synthesis and Doping of Silicon Nanocrystals for Versatile Nanocrystal Inks

A THESIS
SUBMITTED TO THE FACULTY OF THE GRADUATE SCHOOL
OF THE UNIVERSITY OF MINNESOTA
BY

Nicolaas Johannes Kramer

IN PARTIAL FULFILLMENT OF THE REQUIREMENTS
FOR THE DEGREE OF
DOCTOR OF PHILOSOPHY

Prof. Uwe R. Kortshagen, Advisor

May, 2015

© Nicolaas Johannes Kramer 2015
ALL RIGHTS RESERVED

“In rivers, the water that you touch is the last of what has passed and the first of that which comes; so with present time.”

- Leonardo da Vinci

Acknowledgements

My passion for the United States of America started when I was a little boy. I was overwhelmed and inspired by the beautiful national parks, bustling cities and giant cheesecakes. Ever since my family and I went on our yearly trip to the USA I knew that this was the place where I belonged. The American Dream truly exists! After an internship at the Massachusetts Institute of Technology, followed by another research experience at the Colorado School of Mines, I wanted to return on a more permanent basis.

My opportunity came after meeting Prof. Kortshagen at the 2010 Gordon Research Conference on Plasma Processing Science. 6 months later I would land in a cold and snowy Minneapolis to start my Ph.D. in the Kortshagen research group. Not only was this a chance to move to the USA, it also allowed me to continue to work in the fascinating world of nanotechnology. I would like to thank Prof. Kortshagen for this amazing opportunity and the continued support. Your knowledge, coaching and motivation helped me to develop myself tremendously.

Next I would like to thank my current and past group mates. Special thanks goes to David Rowe, Rebecca Anthony, Lance Wheeler, Ting Chen, Narula Bilik, Jeslin Wu, Rick Liptak, Katelyn Schramke, Zvie Razieli, Ben Greenberg, Ryan Gresback, Romain Le Picard, and Jihua Yang. Not only did you offer great support for my research, you also provided plenty of entertainment and made the last four years fly by.

I would also like to show my appreciation to all the members of the High Temperature & Plasma Lab and the research group of Prof. Aydil. I enjoyed the opportunity to share my research and learn from all of you.

My appreciation goes out to my thesis committee members Prof. Hogan, Prof. Dumitrica and Prof. Kakalios. Thank you for your support throughout my Ph.D. and for taking the time to be part of my committee.

I would also like to recognize all the UMN Nanofabrication Center technicians: Gary Olin, Robert Amundson, Kevin Roberts, Lage von Dissen and Rich Mac. Not only did you make sure that my work could always proceed, you also provided some much needed entertainment while working in an underground laboratory.

During my Ph.D. I had the chance to work with a fascinating group of people as part of the Advanced Professional Degree Consulting Club (APDCC). I would like to thank Tim Pearce, Leo Ou, Andy Luo, Mo Sun, and Heng Zhang for the great times. All of you definitely helped me in finding and reaching the next step in my life.

My work would not have been possible without the financial support from the University of Minnesota Doctoral Dissertation Fellowship, the Department of Energy Center for Advanced Photophysics and the Department of Energy Plasma Science Center for Predictive Control of Plasma Kinetics. These centers also provided fruitful collaborations and I would like to thank the members for their help and support.

I was lucky to meet my wonderful girlfriend Julie Archer at the start of my Ph.D. career. You made me realize that there is more in life than science and work. I can't thank you enough for your support, you really made my time here in Minneapolis unforgettable! I would also like to thank Janis and Randy Archer for all their help and the fun times during the last four years. I think you made me a little bit more American.

Finally I would like to thank my parents and sisters for always being there along the way and giving me the opportunities to pursue my dreams. Without your help this Ph.D. journey would have been a lot more difficult. And after 27 years I finally match my Dad, Dr. Nicolaas Kramer III. It took me some time, but now we can have an intellectual conversation accompanied by a nice glass of wine!

Abstract

The impact of nanotechnology on our society is getting larger every year. Electronics are becoming smaller and more powerful, the "Internet of Things" is all around us, and data generation is increasing exponentially. None of this would have been possible without the developments in nanotechnology. Crystalline semiconductor nanoparticles (nanocrystals) are one of the latest developments in the field of nanotechnology.

This thesis addresses three important challenges for the transition of silicon nanocrystals from the lab bench to the marketplace: A better understanding of the nanocrystal synthesis was obtained, the electronic properties of the nanocrystals were characterized and tuned, and novel silicon nanocrystal inks were formed and applied using simple coating technologies.

Plasma synthesis of nanocrystals has numerous advantages over traditional solution-based synthesis methods. While the formation of nanoparticles in low pressure nonthermal plasmas is well known, the heating mechanism leading to their crystallization is poorly understood. A combination of comprehensive plasma characterization with a nanoparticle heating model presented here reveals the underlying plasma physics leading to crystallization. The model predicts that the nanoparticles reach temperatures as high as 900 K in the plasma as a result of heating reactions on the nanoparticle surface. These temperatures are well above the gas temperature and sufficient for complete nanoparticle crystallization.

Moving the field of plasma nanoparticle synthesis to atmospheric pressures is important for lowering its cost and making the process attractive for industrial applications. The heating and charging model for silicon nanoparticles was adapted in Chapter 3 to study plasmas maintained over a wide range of pressures ($10 - 10^5 Pa$). The model considers three collisionality regimes and determines the dominant contribution of each regime under various plasma conditions. Strong nanoparticle cooling at atmospheric pressures necessitates high plasma densities to reach temperatures required for crystallization of nanoparticles. Using experimentally determined plasma properties from the literature, the model estimates the nanoparticle temperature that is achieved during

synthesis at atmospheric pressures. It was found that temperatures well above those required for crystallization can be achieved.

Now that the synthesis of nanocrystals is understood, the second half of this thesis will focus on doping of the nanocrystals. The doping of semiconductor nanocrystals, which is vital for the optimization of nanocrystal-based devices, remains a challenge. Gas phase plasma approaches have been very successful in incorporating dopant atoms into nanocrystals by simply adding a dopant precursor during synthesis. However, little is known about the electronic activation of these dopants. This was investigated with field-effect transistor measurements using doped silicon nanocrystal films. It was found that, analogous to bulk silicon, boron and phosphorous electronically dope silicon nanocrystals. However, the dopant activation efficiency remains low as a result of self-purification of the dopants to the nanocrystal surface.

Next the plasmonic properties of heavily doped silicon nanocrystals was explored. While the synthesis method was identical, the plasmonic behavior of phosphorus-doped and boron-doped nanocrystals was found the be significantly different. Phosphorus-doped nanocrystals exhibit a plasmon resonance immediately after synthesis, while boron-doped nanocrystals require a post-synthesis annealing or oxidation treatment. This is a result of the difference in dopant location. Phosphorus is more likely to be incorporated into the core of the nanocrystal, while the majority of boron is placed on the surface of the nanocrystal. The oxidized boron-doped particles exhibit stable plasmonic properties, and therefore this allows for the production of air-stable silicon-based plasmonic materials which is very interesting for certain applications.

Finally the boron atoms were used to form a Lewis acidic nanocrystal surface chemistry allowing for the creation of ligand-less silicon nanocrystal solutions. This represents an immense step towards an abundant, non-toxic alternative to Pb and Cd-based nanocrystal technologies. The lack of long ligand chains enables the production of dense films with excellent electrical conductivity. This was demonstrated by forming uniform nanocrystal thin-films using simple and inexpensive spray coating techniques.

Contents

Acknowledgements **i**

Abstract **iii**

List of Tables **viii**

List of Figures **ix**

1 Introduction **1**

1.1 Perspective 1

1.2 The Science Behind Nanocrystals 2

1.3 Nonthermal Plasma Synthesis of Nanocrystals 4

1.4 Doping of Semiconductor Nanocrystals 7

1.5 Plasmonic properties of doped nanocrystals 9

1.6 Thesis Overview 11

2 Plasma-induced crystallization of silicon nanoparticles† **14**

2.1 Introduction 14

2.2 Experimental Details 16

2.2.1 Nanoparticle synthesis 16

2.2.2 Nanoparticle characterization 17

2.2.3 Plasma analysis 18

2.2.4 Nanoparticle heating model 19

2.3 Results and discussion 21

2.3.1 Nanoparticle characterization 21

2.3.2 Plasma properties . . . 22
2.3.3 Nanoparticle heating model . . . 24
2.4 Conclusion . . . 28
2.5 Future work . . . 29

3 Requirements for Plasma Synthesis of Nanocrystals at Atmospheric Pressures† 31
3.1 Introduction . . . 31
3.2 Simulation Details . . . 33
3.2.1 Nanoparticle Charging . . . 33
3.2.2 Nanoparticle Heating and Cooling . . . 36
3.3 Results and Discussion . . . 37
3.3.1 Nanoparticle Heating . . . 37
3.3.2 Collisional Regimes . . . 42
3.3.3 Charge Distribution . . . 43
3.3.4 Case Study . . . 45
3.4 Conclusion . . . 46
3.5 Future work . . . 47

4 Doping of Silicon Nanocrystals† 49
4.1 Introduction . . . 49
4.2 Solution-Processed Field Effect Transistors . . . 50
4.3 Doped Si NC FET Characteristics . . . 52
4.4 Size-dependence . . . 55
4.5 Mobility . . . 59
4.6 Conclusion . . . 59
4.7 Future work . . . 60
4.8 Experimental methods . . . 61

5 Plasmonic Properties of Silicon Nanocrystals Doped with Boron and Phosphorus‡ 63
5.1 Introduction . . . 63
5.2 Results and Discussion . . . 65

5.3 Conclusion 77
5.4 Future work 80
5.5 Experimental methods 81

6 Boron-Doped Silicon Nanocrystals in Media Spanning from Hexane to Water‡ 84

6.1 Introduction 84
6.2 Boronated surface 85
6.3 Spray coating 89
6.4 Conclusion 91
6.5 Future Work 92
6.6 Experimental methods 93

References 96

Appendix A. Copyright permissions 114

Appendix B. Self-Assembled Silicon Microstructures from Silicon Nanoparticles 115

Appendix C. Nanoparticle Heating Code 120

List of Tables

2.1 Overview of the plasma conditions for synthesizing 3, 4 and 5 nm nanoparticles in the primary plasma. 17
B.1 Overview of the synthesis conditions for microwire arrays. 116

List of Figures

1.1 **Quantum Confinement.** Size-Dependent emission of silicon nanocrystal solutions excited by an UV source. As the nanocrystal size decreases, the band gap of the nanocrystal increases as a result of quantum confinement effects. This leads to a blue-shift in the nanocrystal emission.[3] . . 3

1.2 **Plasma Synthesis.** Schematic of the nonthermal plasma nanocrystal synthesis system. Silicon nanocrystals are formed by dissociating the silane in an argon plasma. Dopants can be added by introducing phosphine or diborane to the synthesis plasma. An orifice is placed between the synthesis and deposition region to create a strong pressure gradient which accelerates the particles. The nanocrystals are then collected via inertial impaction onto any desired substrate.[13] 6

1.3 **Semiconductor doping.** Schematic of the incorporation of dopants resulting in p-type and n-type silicon. For p-type silicon, a silicon atom is replaced by a boron atom, resulting in a deficiency of electrons. Antimony dopants give rise to n-type silicon, where free electrons are donated to the material. 8

1.4 **Plasmonics in nanocrystals.** Schematic of a plasmon resonance in response to an external electromagnetic field. The free carriers in the silicon nanocrystal resulting from the phosphorus dopants oscillate in response to the light, giving rise to the plasmon resonance.[26] 10

1.5 **Plasmon resonance frequency.** Dependence of the localized surface plasmon resonance frequency on the free carrier concentration in nanocrystals.[31] 11

2.1 **Double plasma experiment.** **(a)** Schematic of the tandem plasma experiment used to study silicon nanoparticle crystallization. Amorphous silicon nanoparticles are formed in a low-power synthesis plasma, followed by heating in a variable-power secondary plasma. Optical emission spectroscopy and capacitance probe measurements are used to determine the properties of the secondary plasma used for heating the nanoparticles. **(b)** Raman spectra from 4 nm nanoparticles as a function of power applied to the secondary plasma. At a critical power of 30 W the crystalline silicon feature at 520 cm^{-1} emerges. **(c)** X-ray diffraction from 4 nm nanoparticles exposed to the secondary plasma as a function of secondary plasma power. Diffractions for silicon nanocrystals emerge when the plasma power exceeds 30 W. **(d)** Transmission electron micrographs of 5 nm diameter silicon nanoparticles when the secondary power is off. This yields amorphous nanoparticles. **(e)** Crystalline nanoparticles are observed in TEM once the secondary plasma power is increased to 40W. 18

2.2 **Surface reactions.** Heating and cooling events occurring on the silicon nanoparticle surface. Heating events are indicated with red dots on the nanoparticle surface while cooling events are shown as blue dots. The electron-ion recombination energy is equal to the argon ionization potential of 15.76 eV. Dangling bond passivation, hydrogen abstraction and hydrogen recombination deliver 3.1, 1.41 and 4.5 eV, respectively. Cooling occurs mainly through collisions with colder gas atoms. At 900 K and higher, thermal desorption of hydrogen starts to play a role, where the energy loss is equal to 1.69 eV for each desorbed hydrogen molecule. 20

2.3 **Plasma characterization.** **(a)** Ion density, **(b)** electron temperature and **(c)** hydrogen density in the second plasma as a function of the secondary plasma power for several different conditions used to operate the primary plasma. The primary plasma conditions are referred to with the size of the nanoparticles they produce. 23

2.4 **Nanoparticle temperature fluctuations.** Time-dependence of nanoparticle temperature calculated from the transient energy balance. The temperatures of each nanoparticle with different size are evaluated at the critical power where the nanoparticles begin to crystallize. This critical power was determined from XRD and Raman scattering data. The nanoparticles in the size range of 3 to 5 nm can reach temperatures significantly above the gas temperature. 25

2.5 **Power dependence.** The temperature of a 4 nm silicon nanoparticle for three different secondary plasma powers. The temperature required for nanoparticle crystallization from Ref.[16] is indicated by the dashed line. The average nanoparticle temperature increases with increasing plasma powers and exceeds the crystallization temperature once the power is equal to or larger than 30 W. 26

2.6 **Heating contributions.** Relative contributions of electron-ion recombination and hydrogen reactions to nanoparticle heating for 3 nm and 5 nm nanoparticles. For 3 nm nanoparticles, both electron-ion recombination and hydrogen reactions equally contribute to nanoparticle heating. For 5 nm nanoparticles hydrogen reactions dominate nanoparticle heating. 27

3.1 **Collisionality regimes.** Schematic illustration of the three collisionality regimes considered in the nanoparticle heating and charging model. Within the capture radius R_0 ions undergo charge-exchange collisions and will eventually be collected by the nanoparticle. In the three regimes considered the ions undergo zero (OML), one (Collision Enhanced), or more than one (Hydrodynamic) collisions within this sphere around the silicon nanoparticle. 34

3.2 **Nanoparticle temperature. (a)** Nanoparticle (NP) temperature as a function of the ion density for a 5 nm silicon nanoparticle at 10^2 Pa and at 10^5 Pa. The dotted line at 770 K represents the experimentally determined temperature required to crystallize 5 nm silicon nanoparticles.[16] For the low-pressure plasma (10^2 Pa) an ion density of 10^{11} cm^{-3} is required for crystallization. This value increases significantly to 4×10^{13} cm^{-3} for atmospheric pressures. **(b)** Effect of the hydrogen density on the nanoparticle temperature at atmospheric pressure (10^5 Pa). Exothermic reactions with hydrogen atoms on the surface of the nanoparticle heats the nanoparticles. These reactions become significant after the hydrogen density exceeds 10^{16} cm^{-3}. 38

3.3 **Nanoparticle temperature variations.** Comparison of the temperature variations of the silicon nanoparticles in plasmas maintained at **(a)** 10^2 Pa and **(b)** 10^5 Pa. At atmospheric pressure (10^5 Pa, $n_i = 4 \times 10^{13}$ cm^{-3}, $T_e = 3eV$ and $n_H = 10^{13}$ cm^{-3}) nanoparticle cooling is faster than that at low pressure (10^2 Pa, $n_i = 10^{11}$ cm^{-3}, $T_e = 3eV$ and $n_H = 10^{13}$ cm^{-3}) (note the difference in time scales in (a) and (b)). In addition, the ion current is enhanced due to an increased ion density and a larger contribution from the hydrodynamic collisional regime. Consequently, the temperature fluctuations are significantly stronger. 40

3.4 **Pressure dependence of temperature variations.** Temporal variation of the nanoparticle temperature at low (10^2 Pa) and atmospheric (10^5 Pa) pressure on common time scale showing the rate at which nanoparticle temperatures fluctuate. Here the ion density is 10^{11} cm^{-3}, the nanoparticle density is 10^8 cm^{-3}, the electron temperature is 3 eV, the hydrogen density is 10^{13} cm^{-3} and the nanoparticles have a diameter of 3 nm. Each instantaneous temperature spike corresponds to an electron-ion recombination or exothermic hydrogen reaction. Under identical plasma conditions, the nanoparticle temperature remains higher at low pressures because additional electron-ion recombination and exothermic hydrogen reactions occur before the nanoparticle cools. At atmospheric pressures the nanoparticle temperature increases briefly and quickly cools to the gas temperature. 41

3.5 **Importance of collisionality regimes.** Comparison of the ion current collection mechanisms to nanoparticle heating for three plasma pressures. In each case, the nanoparticle temperature is shown as a function of the ion density. For the *combined* curve (dotted line) all three mechanisms are included using the probabilities for each regime (equations 8-10). The other curves are the result of calculating the nanoparticle temperature while forcing a specific regime (see text). At low pressures the combined curve follows that predicted by using only the ion current predicted by the OML theory. At intermediate pressure (10^3 Pa), the combined curve shifts closer to the curve predicted by the collision-enhanced (CE) ion current. At atmospheric pressure, the combined curve is mainly predicted by using the hydrodynamic (HY) ion current. 43

3.6 **Charge distribution**. Normalized charge distribution of silicon nanoparticles in plasmas maintained at low pressure (10^2 Pa) and at atmospheric pressure (10^5 Pa) for four different nanoparticle sizes. The increase in the ion current collected by the nanoparticle at atmospheric pressure reduces the negative charge (Q) on the nanoparticles. For a given size, the negative charge on the nanoparticles is smaller at atmospheric pressure than at low pressure. 44

3.7 **Case study.** Nanoparticle temperature as a function of time during atmospheric pressure synthesis under experimental conditions reported by Nozaki *et al.*[81] The nanoparticles reach temperatures that exceed the crystallization temperature for 3 nm silicon nanoparticles. The inset shows the charge distribution of the nanoparticles in the plasma. As a result of the low electron temperature (0.5 eV) and high ion density (10^{15} cm^{-3}) the nanoparticle charge is low. 45

4.1 **FET fabrication.** **(a)** Si NC fabrication process with photographs of a plasma reactor and a suspension of Si NCs in DCB and device structure. **(b)** SEM cross-sectional image of device showing layers, from bottom to top of p+ silicon gate, 130 nm oxide, ∼100 nm Si NC layer, and 60 nm aluminum. **(c)** Photograph of Si NC FET with NC layer partially removed to expose blue oxide, the golden color corresponds to the Si NC thin films (∼30 nm), and gray to the aluminum source and drain top contacts. TEM images of **(d)** large (8-15 nm) and **(e)** small (4-7 nm) Si NCs. 51

4.2 **FET characterization.** Drain-current (I_D)-gate-voltage (V_{GS}) characteristics of doped Si NC thin films FETs **(a)** measured using a fast sweep rate of $10Vs^{-1}$ for (red) P- and (blue) B-doped (dashed) 10% 8-15 nm, (solid) 1% 8-15 nm, (dot) 1% 4-7 nm, (black solid) intrinsic 8-15 nm, and (black dot) intrinsic 4-7 nm Si NCs, **(b)** mobility-normalized I_D-V_{GS} characteristics plotted on a linear scale, and the same devices measured with a slower sweep rate of 1 Vs^{-1} on **(c)** a semi-log scale and **(d)** a non-normalized linear scale. All devices shown have width/length (W/L) of 2000/20 μm and are measured with a drain-source voltage (V_{DS}) of 30 V. 53

4.3 **Doping dependence.** Output characteristics of Si NCs thin films transistors with nominally **(a)** 1% B-doped, **(b)** intrinsic, **(c)** 1% P-doped, and **(d)** 10% (blue) B- and (red) P-doped; diamonds are where V_{DS} = V_{SAT} = V_{GS} - V_T, indicating where the expected transition to saturation behavior, with V_T specified in each panel. 55

4.4 **Threshold voltage.** **(a)** Threshold voltage (V_T) summary as a function of nominal doping concentration and **(b)** μ_{lin} dependence on nominal doping concentration for (red) P, (black) intrinsic, and (blue) B Si NC thin films for (diamond) small 4-7 nm, and (circle) large 8-15 nm Si NC thin films. Error bars are the standard deviation of 5-8 devices fabricated from the same batch of NCs with at least 2 different substrates where each point represents a different batch of NCs, some points are slightly offset for clarity. Lines in (a) are calculated V_T for various active dopant activation efficiencies. Inset: Density of states diagram and the effect of dopants and gate-induced electrons on the Fermi level, E_F. 56

4.5 **FET characteristics of small Si NCs.** Characteristics of Si NC FETs fabricated with small (4-7 nm) Si NCs showing sudden change from intrinsic to metallic behavior. **(a)** I_D-V_{GS} characteristics on a semi-log scale, and **(b)** normalized scaling of conductivity according to percolation theory compared with the (steady-state) off-currents of 4-7 nm P-doped as a function of nominal doping concentration and output characteristics with nominally **(c)** 1% P-doped, **(d)** 2% P-doped, **(e)** 5% P-doped, and **(f)** 10% P-doped. 58

5.1 **Plasmonics of phosphorus-doped and boron-doped Si NCs.** FTIR spectra of as-produced **(a)** phosphorus-doped and **(b)** boron-doped silicon nanocrystals with increasing fractional doping flow rates. For phosphorus-doped Si NCs a LSPR emerges for sufficiently high doping concentrations. A LSPR is not visible for boron-doped Si NCs, even at high doping levels. Dopant surface atoms as well as silicon hydride peaks are observed, as indicated by the blue and orange regions. Spectra are offset for clarity. **(c)** Oxidation of phosphorus-doped and boron-doped Si NCs in air as a function of time. Opposite behavior is observed, with the LSPR disappearing for phosphorus-doped Si NCs while a LSPR develops and blue-shifts during oxidation for boron-doped Si NCs. **(d)** Development of the LSPR for as-produced and subsequent oxidized and etched phosphorus-doped and boron-doped Si NCs. 67

5.2 **EDX on P-doped Si NCs.** Atomic phosphorus concentration in Si NCs obtained from Energy-Dispersive X-Ray spectroscopy (EDX) measurements. An increase in phosphine (PH_3) flow rate directly leads to a larger fraction of phosphorus within the NCs. After HF vapor etching the phosphorus concentration decreases, indicating that oxidation and subsequent etching leads to a removal of phosphorus from the NCs. . . . 68

5.3 **Electron Paramagnetic Resonance spectra for phosphorus-doped, boron-doped and intrinsic Si NCs.** Spectra are shown for as-deposited (red) and oxidized (blue) Si NCs. The spectrum for boron-doped NCs has been magnified by a factor of 5 for clarity. 71

5.4 **XPS measurements.** X-ray Photoelectron Spectroscopy (XPS) spectra for as-produced and oxidized phosphorus-doped and boron-doped silicon NCs. The phosphorus spectrum can be deconvolved into two peaks. The peak at 130 eV corresponds to phosphorus bonded to phosphorus or silicon (red), while the broad peak at 135 eV is a result of oxidized phosphorus (blue). For boron a broad peak at 185 eV originates from trivalent boron (blue) while the higher energy peak at 188 eV corresponds to tetravalent boron (red). The two peaks at 191 eV (red) and 193 eV (orange) are a result of oxygen bonding to boron. 73

5.5 **Effect of oxides on plasmonics.** **(a)** Development of the plasmon resonance during low-temperature air-free annealing of phosphorus and boron-doped Si NCs. As a result of the annealing step the plasmon significantly blue-shifts for phosphorus-doped Si NCs. For boron-doped Si NCs, the annealing treatment is able to generate additional free carriers, leading to a plasmon resonance to develop. **(b)** FTIR spectra of as-produced, oxidized and subsequent annealed at 200°C phosphorus-doped and boron-doped silicon nanocrystals. While the plasmon resonance is removed after oxidation, an annealing treatment is able to bring the plasmon resonance back. **(c)** Development of the plasmon resonance for phosphorus-doped Si NCs after oxidation, subsequent annealing followed by re-oxidation for 1, 2, 3 and 4 days. **(d)** EPR spectra for phosphorus-doped Si NCs. A distinct difference is observed between annealed and (re-)oxidized NCs, agreeing with the FTIR spectra of (c). 75

5.6 **EPR on annealed Si NCs.** Electron Paramagnetic Resonance (EPR) spectra for as-produced (gray) and annealed (red) Si NCs. A reduction in signal is observed for annealed intrinsic NCs as a result of surface restructuring and defect reduction. A feature is also removed from the phosphorus-doped spectra, likely caused by a similar reduction in defects. The boron-doped spectrum does not change significantly after annealing. 76

5.7 **Phosphorus-doped silicon nanocrystal plasmonic overview.** Summary for the plasmonic behavior of phosphorus-doped silicon nanocrystals. A plasmon resonance is observed for as-produced nanocrystals once the doping concentrations exceeds 5%. Post-synthesis treatments allow for further tuning of the resonance position. 79

5.8 **Boron-doped silicon nanocrystal plasmonic overview.** Plasmonic behavior of boron-doped silicon nanocrystals. As-produced nanocrystals do not exhibit a plasmon resonance, but after a post-synthesis annealing or oxidation treatment the plasmonic resonance emerges. 79

6.1 **Lewis acidic Si NC surface.** **(a)** XPS B1s spectrum of Si NCs as they are produced from the plasma reaction. Surface B(III) accounts for ~60% of the boron in the sample. **(b)** FTIR spectra of Si NCs synthesized from SiH_4 only (black), from SiH_4 and 10 atomic percent boron (red), and Si NC sample produced from 10 atomic percent boron after a brief exposure to air. **(c)** Cartoon representation of B segregation to the Si NC surface to form Lewis acidic B(III) groups. **(d, e)** Photographs of biphasic solutions of hexane and DMSO. In (d), oleylamine-capped Si NCs are stable in hexane, and in (e) Si NCs are stable in DMSO without a ligand. (Figure adapted from Lance Wheeler) 86
6.2 **Cosolvent effects on colloidal stability.** **(a)** FTIR spectra of the C=O stretching vibration of NMP taken as a function of time as NMP evaporates from Si NC colloid. **(b)** A photograph of 50% volume mixtures of a variety of cosolvent systems. **(c)** FTIR spectra for films of Si NCs cast from NMP/water mixture of varying volume fractions. Spectra are normalized and offset for clarity. **(d)** FTIR spectra of Si NC film cast from a solution of NMP and 10% water by volume before (green) and after (black) vacuum-treating the sample. Spectra are offset. (Figure adapted from Lance Wheeler) 88
6.3 **Film morphology for spray coated films.** **(a)** Top-view SEM image of web-like film structures resulting from fast solvent evaporation. **(b)** Spherical Si NC agglomerates deposited on top of the NC films during spray coating. 90
6.4 **Uniform thin-film of Si NCs deposited using the spray coating technique.** **(a)** Top-view SEM image of the NC film on a silicon wafer substrate. **(b)** Side-view profile of a ~100 nm thick Si NC thin film. . . 91
B.1 **Film structure dependence on deposition conditions.** Change in film structure for three deposition conditions. **(a)** A small distance (0.5 cm) between orifice and substrate creates dense nanoparticles films. **(b)** By increasing the distance to 1 cm a more porous structure is formed. **(c)** Using a pinhole orifice placed at a distance of 5 cm from the substrate creates very porous structures. 116

B.2 **Effect of annealing.** Significant densification of the as-deposited structures occurs during annealing. Temperatures of up to 1000°C are reached in the rapid thermal annealer for 10 seconds. 117

B.3 **Orifice dependence.** The effect on the deposition structures after annealing for different orifice diameters. 118

Chapter 1

Introduction

1.1 Perspective

Energy utilization and efficiency is currently one of mankind's most challenging problems. The world's energy consumption is 15 Terawatts and is estimated to double by 2050.[1] Not only will reserves of fossil fuels fall short of this demand in the long term, increased environmental awareness requires the use of alternative clean energy sources such as solar power. A back of the envelope calculation will show that, with today's technology, an area of 500.000 square kilometers, or roughly the size of Spain, needs to be covered with solar cells to meet the world's energy demand. Current solar cell production methods are simply too slow and expensive to achieve this, but third-generation solar cells based on novel semiconductor nanocrystals (NCs) have the potential to overcome these hurdles.

Now imagine ink that can turn any surface into a solar cell, or produce electronic display devices such as cell phones or touchpads for a fraction of the cost of current products. While this may sound very futuristic, research on electronic inks is ongoing. The size of the printed electronics market was already $0.53 billion in 2009 and is expected to reach $5.00 billion by 2016.[2]

The main component of electronic inks are nanometer-sized semiconductor crystals (nanocrystals), about 10,000 times smaller than a human hair. They form an ink by dispersing them into a liquid (solvent). Semiconductor materials form the heart of modern electronics and are also the main component of solar cells. Today, the dominant

semiconductor material is silicon. As the principal ingredient of beach sand, it is an abundant and non-toxic material with precisely tunable properties. NC inks promise a new era in semiconductor processing in which thin films are inexpensively printed or sprayed on any desired substrate such as glass or Kapton (a strong and flexible polymer material) to form thin and flexible devices.

Silicon in nanocrystal form is an excellent candidate for use in electronic inks. It is a material that is safe, abundant, inexpensive and efficient in generating energy. Integration with today's silicon-based electronics can also be stimulated if silicon inks are used. In this thesis the synthesis and electronic properties of these silicon nanocrystals and silicon nanocrystal inks are studied in detail. This chapter will first introduce the important concepts to the reader that encompass the work described in this thesis.

1.2 The Science Behind Nanocrystals

A nanocrystal is defined as a material particle with a dimension smaller than 100 nanometers and composed of atoms that are arranged in a crystal lattice. While these nanocrystals still consist of the same material as their bulk counterpart, their properties can be significantly different. There are two fundamental differences: (1) The optical and electronic properties are size-dependent and can deviate significantly from bulk properties and (2) The surface characteristics become much more important due to the high surface-area-to-volume ratio of the nanocrystals. An example of the difference between bulk materials and nanomaterials is the light emission properties of silicon nanocrystals (see Figure 1.1). For bulk silicon, light emission is extremely inefficient due to its indirect band gap. However, once the size of silicon is decreased to 10 nanometers or less, and it crystal structure is free of defects, the nanocrystals are able to efficiently emit light with quantum yields that exceed 60%. In addition, the emission wavelength can be tuned by simply changing the size of the nanocrystals.

In recent years the progress on nanocrystal research and their applications has been tremendous. A better understanding of these nanocrystals has lead to solar cell designs with efficiencies exceeding 9%,[4] next-generation displays with improved colors and contrast,[5] and even efficient low temperature steam generators.[6] These nanocrystals are not just research objects anymore, but are rapidly transitioning into the market place.

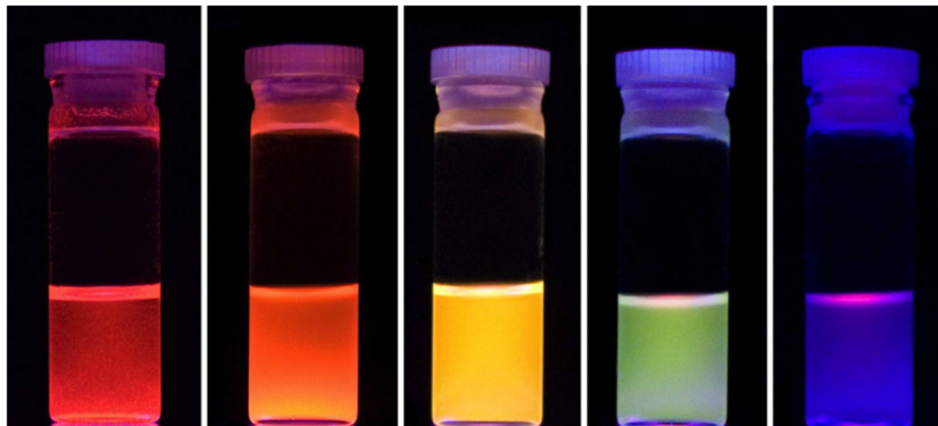

Figure 1.1: **Quantum Confinement.** Size-Dependent emission of silicon nanocrystal solutions excited by an UV source. As the nanocrystal size decreases, the band gap of the nanocrystal increases as a result of quantum confinement effects. This leads to a blue-shift in the nanocrystal emission.[3]

High quality nanoparticles are essential for excellent device performance.[7] In order to fully utilize the nanoparticle properties it is necessary to have a material with a crystalline structure (nanocrystal). Silicon is able to form a perfectly ordered crystal lattice in which each atom forms a strong covalent bond (bond that involves the sharing of electron pairs by two atoms) with its neighboring atoms. The opposite is an amorphous material, in which there is no apparent order within the material. Amorphous nanoparticles typically have higher defect densities and charge carrier trap states, which are detrimental to the electronic and optical properties of the nanomaterials. An amorphous nanoparticle can be transformed to a nanocrystal by supplying enough energy in the form of heat during or after synthesis. Finding the appropriate synthesis conditions to obtain crystalline nanoparticles is therefore of importance, and this will be discussed in detail in this thesis.

The interesting optical and electronic properties of nanocrystals are a result of the physics that arise at these small sizes. Once a material is scaled to sizes that approach the exciton Bohr radius of the material, it starts to exhibit so-called quantum effects. The electronic structure then starts to resemble that of an atom instead of a collection of atoms.[8] This is a result of the electronic wave function of the NC which starts to

extend spatially beyond the physical volume of the NC as the size of the NC decreases. The wave function is thus "confined" to a small volume in space, an effect known as "quantum confinement". As a consequence, the electronic structure of a material is transformed from the continuous band of energy states found in bulk materials to more discrete states found in atoms. A further decrease in NC size leads to a larger separation of the quantized states. The optical properties depend on the separation of these states and can thus be tuned by simply changing its size. For silicon, quantum confinement effects are observed for diameters less than 10 nm.

Depending on the synthesis method, nanocrystals are either collected as a dry powder or film, or produced directly as a nanocrystal solution. Both dry and solution products have their own advantages. A major advantage of nanocrystal inks is their ease of use compared to existing semiconductor processing technologies. A film can very easily be applied to large areas using well-known techniques such as spray coating.[9] To produce a nanocrystal ink, a stable solution of nanocrystals in a solvent needs to be formed, in which the nanocrystals are evenly spaced and isolated from one another. This is traditionally achieved by attaching soap-like organic molecules, or ligands, to the nanocrystal surface to prevent nanocrystals from sticking together.[10,11] Without these ligands the nanocrystals will agglomerate to form large clusters and destabilize the ink. However, when a nanocrystal film is deposited on a substrate, these long ligands are detrimental to the electrical properties as they increase the spacing between nanocrystals and form an electrical barrier for charge carriers. Removing the ligands after deposition is difficult due to the strong covalent bonds that the ligands form with the nanocrystals. A novel approach to form ligand-less colloids is presented in this thesis. These inks allow for closer spacing of nanocrystals during deposition of a film.

1.3 Nonthermal Plasma Synthesis of Nanocrystals

In this work we utilize the unique chemical environment of nonthermal plasmas to synthesize nanocrystals directly in the gas-phase.[12] A nonthermal plasma is a reactive, ionized gas with gas temperatures that are just above room temperature. Using plasmas for nanocrystal synthesis has emerged as a promising alternative to traditional solution-based synthesis routes. It allows for the production of high-quality crystalline

nanoparticles with narrow size distributions without the need of hazardous liquid chemicals or ligands. Since it is a flow-through process, plasma synthesis also allows for high production yields and is scalable for use in industrial settings.

A schematic of a typical low-pressure plasma reactor is illustrated in Figure 1.2. The gases are introduced into a glass tube with a diameter ranging from 1/4" to 1", leading to a pressure of approximately 1 Torr. Argon gas is typically used as the source for electrons and ions. The preferred gaseous molecular precursors are then mixed with the argon. For silicon the most common precursor is silane (SiH_4) while germanium nanoparticles can be synthesized using germane (GeH_4). This example also contains the two dopant gasses phosphine (PH_3) and diborane (B_2H_6). Radio frequency (rf) power is applied to two electrodes to ignite and maintain the plasma.

The non-equilibrium environment of the plasma allows for the dissociation of the gaseous molecular compounds. This is a result of the imbalance of the gas temperature, which remains close to room temperature (∼300-600K), and the electron temperature, which is significantly higher (∼20,000-50,000K). After the gaseous precursors are dissociated the silane radicals will cluster together to form nanoparticles in the plasma. For silicon nanoparticles, the crystallization process (essential for high quality nanocrystals) requires temperatures of 850K or more.[14–16] However, the gas temperature remains close to room temperature during synthesis, allowing the reactor to be touched during NC formation. So how are these nanoparticles able to obtain a crystal structure? This mystery will be solved in Chapters 2 and 3 of this thesis.

The large difference in ion and electron temperature and mobility gives rise to another advantage. The high electron mobility will lead to a negative charge on the nanoparticle surface as well as the reactor walls.[17] Electrostatic repulsion between nanoparticles prevents the nanoparticles from agglomerating with each other, resulting in a narrow size distribution.[18,19] The negative charge on the reactor walls limits nanocrystal losses to the walls, thus increasing production yields.

The nanoparticle properties such as size, composition and crystallinity can be simply tuned by changing the plasma properties. Typically the most important parameters are the pressure, gas flow rates and power applied to the plasma. This controls the residence time in the plasma and the density of energetic species, which in turn will directly affect the nanoparticle properties. For example, to decrease the nanoparticle size, the gas flow

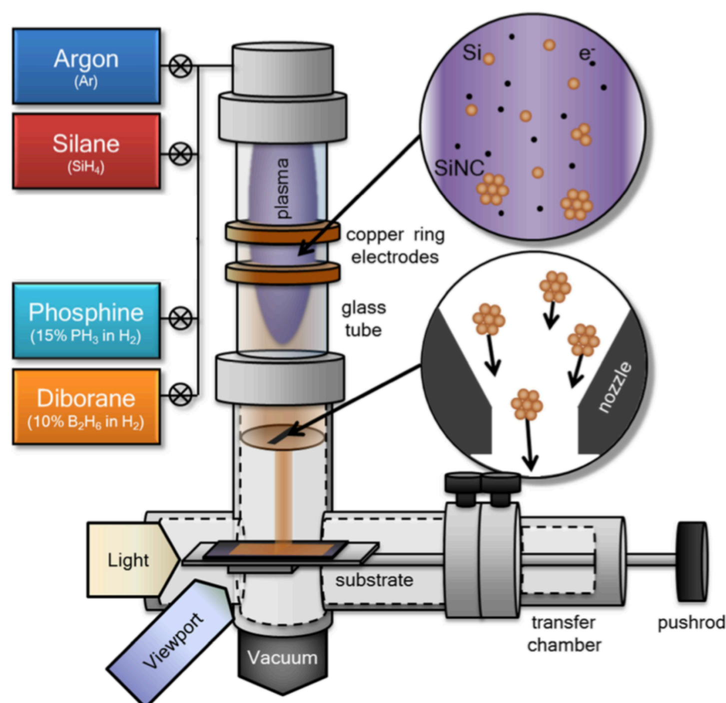

Figure 1.2: **Plasma Synthesis.** Schematic of the nonthermal plasma nanocrystal synthesis system. Silicon nanocrystals are formed by dissociating the silane in an argon plasma. Dopants can be added by introducing phosphine or diborane to the synthesis plasma. An orifice is placed between the synthesis and deposition region to create a strong pressure gradient which accelerates the particles. The nanocrystals are then collected via inertial impaction onto any desired substrate.[13]

rates can be lowered which gives rise to a lower plasma pressure. Now the residence time in the plasma is reduced, leading to smaller nanoparticles.

Another advantage of the plasma synthesis technique is its nanocrystal collection mechanism. In plasma synthesis of nanocrystals we use two mechanisms for nanocrystal collection. Both collection mechanisms allow for the collection of pristine nanocrystals without any ligands on its surface. First the nanocrystals can be collected as a powder by filtering them out of the gas stream. This is achieved by simply placing a mesh downstream of the plasma. An alternative method is to inertially impact the nanocrystals directly onto a substrate.[20,21] This is a very powerful collection mechanism and

allows for the collection of nanocrystals on any desired substrate. Impaction of the nanocrystals is achieved by creating a large pressure difference between the nanocrystal synthesis region and collection region. A gas restriction in the form of an orifice is placed downstream of the synthesis plasma (see Figure 1.2). The role of the orifice is to create a pressure difference between the synthesis and deposition region. This will in turn accelerate the nanoparticles onto a substrate where they are collected for further use.

1.4 Doping of Semiconductor Nanocrystals

Now that we can synthesize high quality semiconductor nanocrystals, the next step is to alter their electronic properties. Unlike metals, pure semiconductors have no "free" electrons that can move easily between atoms since all electrons are involved in covalent bonds, therefore strongly decreasing the conductivity of the material. However, the electronic properties of semiconductors can be tuned by mixing impurities called dopants into the crystal lattice. Impurities have been shown to strongly modify electronic, optical, and magnetic properties of bulk semiconductors. The majority of modern day technologies rely on doped semiconductors, and it is believed that doping of nanocrystals will be important as well for their use in applications. For silicon, typical dopant atoms are phosphorus and boron. For silicon, extra electrons are introduced by replacing a silicon atom with a phosphorus atom (so-called n-type doping). These additional free electrons allow for an electronic current to flow through the material. Adding boron on the other hand leads to "holes" (absence of electrons) in the lattice (p-type doping). Both n-type and p-type silicon is shown schematically in Figure 1.3.

While doping of bulk materials is well understood, introducing dopants at the nanoscale gives rise to new challenges. Introducing even a single impurity atom into a 4 nm nanocrystal of approximately 1000 atoms results in a doping level of $7 \times 10^{19} cm^{-3}$. In a bulk semiconductor, this would constitute extremely heavy doping. Nevertheless, the average number of impurities per nanocrystal is still small, and fluctuations in their location and number can be significant. To minimize such fluctuations, a deeper understanding of the doping process and accurate experimental tools are required to better understand the doping process.

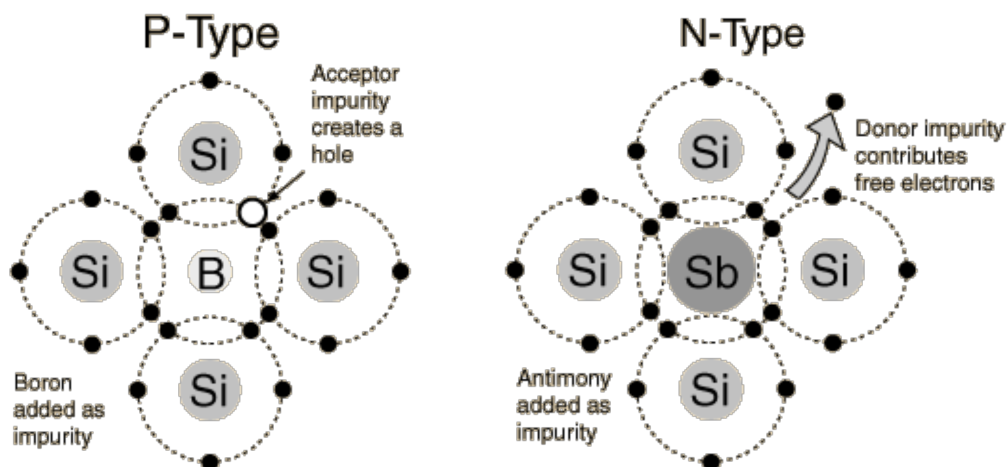

Figure 1.3: **Semiconductor doping.** Schematic of the incorporation of dopants resulting in p-type and n-type silicon. For p-type silicon, a silicon atom is replaced by a boron atom, resulting in a deficiency of electrons. Antimony dopants give rise to n-type silicon, where free electrons are donated to the material.

In recent years nanocrystals have been successfully doped, but their doping concentration is often much lower than expected.[22,23] To understand this we must consider the nanocrystal growth and doping process. In order to successfully dope a nanocrystal, a full incorporation of the dopant atoms in the crystal lattice is required. If the dopant atom is placed on the surface or an interstitial site within the crystal lattice, the dopant is not considered active as it does not provide an electron or hole. For nanocrystals a "self-purification" model was proposed.[24,25] The model suggests that impurities are hard to incorporate due to thermodynamic reasons, leading to the expulsion of the dopants to the surface. This implies that impurity atoms must be able to diffuse readily through the nanocrystals during growth. This explains the lower than expected doping concentration, as the majority of the dopant atoms will diffuse to the surface of the nanocrystal where they are inactive.

An alternative model is the trapped dopant model which is governed by growth kinetics.[23] During nanocrystal growth the dopant atom will adsorb on the surface. In order to incorporate this dopant, additional material must be added to the nanocrystal to trap the dopant atom. For this to occur, the surface must be favorable for impurity

binding. This model also assumes that dopant diffusion during growth is minimal.

Plasma synthesis has proven to be capable of producing highly doped nanocrystals. Dopant incorporation is achieved by simply introducing a gaseous dopant precursor such as phosphine (PH_3) or diborane (B_2H_6) to the synthesis plasma (shown schematically in Figure 1.2).[26–28] The plasma will dissociate the dopant precursor which is followed by the incorporation of the dopant atom in the nanocrystal core or the nanocrystal surface. This doping strategy is significantly easier compared to doping nanocrystals during traditional solution synthesis processes. For silicon nanocrystals, the doping concentration can be easily tuned by changing the ratio of the silane and dopant precursor flow rate. Introducing both dopant precursors allows for "codoping" of the nanocrystals, where both n-type and p-type dopants are incorporated in the nanocrystal. This has shown to lead to significant band gap narrowing in silicon with below bulk band gap emission.[29,30]

1.5 Plasmonic properties of doped nanocrystals

When impurity atoms are incorporated in the lattice of the nanocrystal, additional electrons or holes are donated to the material, as was described in the previous paragraph. Once the doping concentration is high enough, these free carriers will interact with external electromagnetic fields. This is a so-called Localized Surface Plasmon Resonance (LSPR). It arises from the resonant interaction of free charge carriers with the oscillating electromagnetic field of light, which is shown schematically in Figure 1.4.

In recent years, LSPRs has been observed in heavily-doped semiconductor and metal oxide nanocrystals, where it is attributed to the high density of free charge carriers introduced by doping. In contrast to noble metal NCs, the LSPR of semiconductor NCs can be directly tuned by adjusting the doping concentration. However, the density of free charge carriers achievable in these doped NCs is lower than that of noble metals and, as a result, their LSPR is at lower energy or longer wavelength. The correlation between the LSPR frequency and free carrier concentration is shown in Figure 1.5.

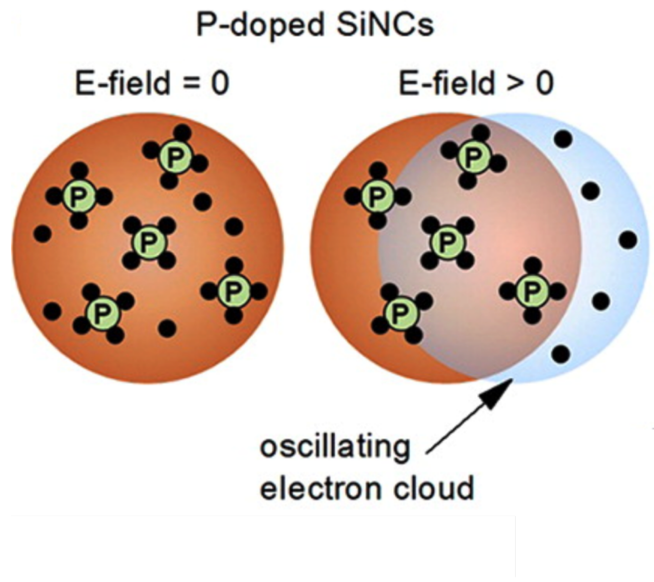

Figure 1.4: **Plasmonics in nanocrystals.** Schematic of a plasmon resonance in response to an external electromagnetic field. The free carriers in the silicon nanocrystal resulting from the phosphorus dopants oscillate in response to the light, giving rise to the plasmon resonance.[26]

By considering the Drude model we can calculate the LSPR frequency (f_{LSPR}).[32] This is given as:

$$f_{LSPR} = \frac{1}{2\pi}\sqrt{\frac{N_{fc}e^2}{\epsilon_0 m_e^*(\epsilon_\infty + 2\epsilon_m)}} \tag{1.1}$$

with N_{fc} the free carrier concentration in the nanocrystals, ϵ_0 the free space permittivity, e the electron charge, ϵ_∞ the high frequency dielectric constant,ϵ_m the dielectric of the surrounding medium and m_e^* the free carrier effective mass.[33] Not only does it allow for the calculation of the required doping concentration for a specific plasmon resonance, the resonance can also be used to estimate the doping concentration in the particle itself. Therefore the plasmonic properties can give insight in the number of active dopants within the nanocrystal. In this work we will use this property of plasmonics to gain a better understanding of the doping process of plasma synthesized nanocrystals.

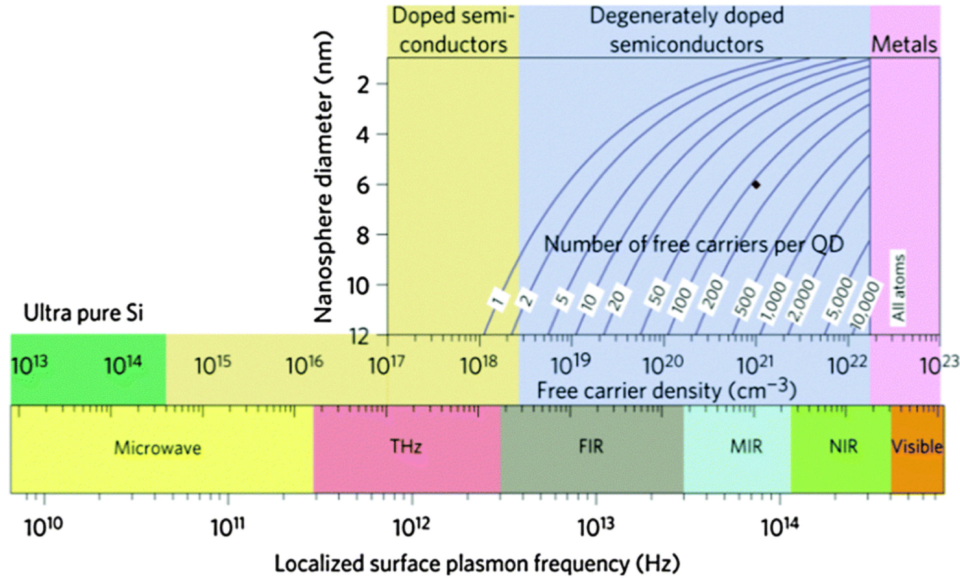

Figure 1.5: **Plasmon resonance frequency.** Dependence of the localized surface plasmon resonance frequency on the free carrier concentration in nanocrystals.[31]

The exciting properties of these plasmon resonances open the door for a wide array of novel nanocrystal applications.[34] Due to their enhanced absorption properties, plasmonic nanocrystals are a rapidly emerging research field with applications in photovoltaics,[35] bio-sensing,[36] photothermal therapy[37] and nano antennas.[38] An air-stable silicon-based plasmonic material is highly desirable for certain applications, and this will be pursued in this work.

1.6 Thesis Overview

Now that the vision of the work and the basic underlaying physics have been introduced, the next step is to further explore some of the unanswered questions and challenges. The focus of this work can be divided into two main topics: understanding the plasma synthesis of nanocrystals and exploring the properties of doped nanocrystals. These two topics will be combined at the end to form versatile silicon nanocrystals inks.

First the plasma synthesis of silicon nanocrystals is explored in Chapter 2. Here a mystery was solved: how do silicon nanoparticles crystallize in nonthermal plasmas if

the gas temperature is close to room temperature? A combination of experimental work and a nanoparticle heating model provides the answer to this question. The content is adapted from a publication in Journal of Physics D: Applied Physics entitled: "Plasma-induced crystallization of silicon nanoparticles". The results provide a much deeper understanding on how nanocrystals form in nonthermal plasmas.

The work is continued in Chapter 3, where the nanoparticle heating model is expanded to allow for the analysis of nanoparticle heating at a wide range of plasma pressures. Forming nanocrystals at atmospheric pressures is highly desirable for industrial processes, but the required conditions for successful synthesis are unknown. In order to understand how these higher pressures affect nanocrystal synthesis we utilize the nanoparticle heating model to predict what the required plasma conditions are in order to produce nanocrystals at atmospheric pressures. This work was published in Journal of Physics D: Applied Physics under the title: "Requirements for Plasma Synthesis of Nanocrystals at Atmospheric Pressures".

Next we change gears slightly and discuss dopant incorporation in silicon nanocrystals in Chapter 4. This work was done in collaboration with Dr. Ryan Gresback and Prof. Tomohiro Nozaki from the Tokyo Institute of Technology. Using solution-processed Field Effect Transistors we were able to determine the doping concentration and electrical properties of p-type and n-type silicon nanocrystals. These results reveal that intentional inclusion of impurities in the core of silicon nanocrystals can effectively be incorporated, resulting in control of the Fermi-level and carrier concentration. Parts of this chapter were published in ACS Nano with the title: "Controlled Doping of Silicon Nanocrystals Investigated by Solution-Processed Field Effect Transistors".

Chapter 5 builds on this work and explores the plasmonic properties of highly doped silicon nanocrystals. While the synthesis for p-type and n-type nanocrystals is identical, the dopants behave very differently. The plasmonic behavior also allows us to gain insight in the dopant position of as-produced and post-synthesis treated nanocrystals. In addition, we are able to produce air-stable silicon-based plasmonic materials. This work was submitted to Nano Letters as "Plasmonic Properties of Boron and Phosphorus Doped Silicon Nanocrystals".

Finally we explore the exciting solubility properties of boron-doped silicon nanocrystals in Chapter 6. Here the previous work comes together to realize an exciting new

frontier in nanocrystal inks. Besides acting as a dopant, we found that boron atoms on the nanocrystal surface allow for the formation of solutions in polar solvents without the need of ligands. This is the result of a Lewis acid-base interaction between the solvent and the nanoparticle. Lance Wheeler did extensive research on the stability mechanism and this work will be submitted for publication in the near future. This chapter also covers the use of spray coating techniques to form thin and uniform nanocrystal films using the boron-doped silicon nanocrystal inks. Reid Herd deserves most of the credit for optimizing these films as part of his undergraduate research opportunities program.

Chapter 2

Plasma-induced crystallization of silicon nanoparticles†

2.1 Introduction

Using low-pressure nonthermal plasmas for the synthesis of silicon, germanium and indium phosphide nanoparticles is well-established.[39–45] Electrons in nonthermal plasmas can reach temperatures as high as 5 eV, and can dissociate molecular precursors such as silane and silicon tetrachloride upon collision to form reactive radicals.[44,46] These radicals react to nucleate and grow nanometer sized particles. The nanoparticles formed in nonthermal plasmas tend to be negatively charged due to the significantly larger mobility and temperature of the electrons compared to the heavier positive ions.[47–49] The negative charge on the particles reduces agglomeration and coalescence significantly,[50,51] leading to much narrower and well-defined particle size distributions compared to other aerosol-based nanoparticle synthesis processes. Moreover, charging reduces, and even eliminates, diffusion losses to the walls of the reactor.[52] The residence time of the particles in the plasma offers excellent control of the particle size.[39] Depending on the synthesis conditions, the nanoparticles can be amorphous or crystalline.[53]

†Portions of this chapter have been published in the manuscript by Nicolaas J. Kramer, Rebecca J. Anthony, Meenakshi Mamunuru, Eray S. Aydil and Uwe R. Kortshagen in Journal of Physics D: Applied Physics (doi:10.1088/0022-3727/47/7/075202, 2014)

The ability to produce crystalline group IV and III-V materials makes plasma synthesis an attractive method. However, one aspect of the plasma synthesis technique that is still poorly understood is nanoparticle heating, which is believed to be necessary for the formation of crystalline particles. Obtaining crystalline particles is critical for many optical and electronic applications, since amorphous particles typically have higher defect densities and charge carrier trap states, which are often detrimental to the electronic and optical properties of nanomaterials.[53] Moreover, knowledge of the nanoparticle temperature is critical for the successful incorporation of dopants into nanoparticles.[54,55]

While the melting and crystallization temperatures are lower for nanoparticles compared to their bulk counterparts,[56] nanoparticles of covalently bonded semiconductors still requires relatively high temperatures for crystallization. For instance, a recent study showed that crystallization of 4 nm, 6 nm, 8 nm and 10 nm diameter silicon nanoparticles requires temperatures of 773 K, 1073 K, 1173 K and 1273 K, respectively.[16] In a different study, crystallization temperatures for silicon particles larger than 10 nm were reported to be higher than 1047 K.[14] In contrast, the gas temperature in non-thermal plasmas is only 300 to 500 K,[39] well below the temperatures required for crystallization, even for the smallest nanoparticles. Thus, the nanoparticles must be heated by the plasma to several hundreds of Kelvin above the gas temperature in order to crystallize. While several groups reported that it is possible for particles to exceed the gas temperature in plasmas,[57–59] these temperatures were still not sufficient for crystallization of silicon nanoparticles.

Previously, Anthony *et.al* demonstrated an increase in silicon nanoparticle crystallinity with increasing power delivered to the plasma,[53] which suggests that increasing nanoparticle temperature is responsible for crystallization. However, possible nanoparticle heating mechanisms have thus far only been investigated through computational models.[49,60,61] These studies found that the temperature of small (< 5 nm) nanoparticles never reaches a steady state on the scale of the residence time, and that their temperatures can frequently spike to more than 1000 K. However, when the nanoparticles grow larger (> 5 nm), the magnitude of the temperature spikes reduces significantly and the particle temperature can reach steady state.

In situ measurement of the nanoparticle temperature in a plasma is difficult, but the

nanoparticles themselves can serve as thermometers, as their crystallinity and surface will change depending on the conditions they experience in the plasma. Here we present an approach that combines detailed plasma characterization with modeling to elucidate the heating mechanisms that lead to nanoparticle crystallization. In this approach, amorphous silicon nanoparticles are produced in a low-power plasma and subsequently injected into a second variable-power plasma. Here after, the first plasma used to synthesize the amorphous nanoparticles is also referred to as the primary plasma while the second plasma used to crystallize the nanoparticles is referred to as the secondary plasma. This approach decouples the nanoparticle synthesis and nanoparticle heating. The nanoparticle size can be varied by changing the synthesis conditions in the first plasma; this allows the investigation of the crystallization process for different nanoparticle sizes.

2.2 Experimental Details

2.2.1 Nanoparticle synthesis

Silicon nanoparticles are formed in a continuous-flow low-pressure plasma reactor from an argon-silane-helium gas mixture, as described in detail previously.[39] The reactor consists of a borosilicate glass tube through which the reactant gases flow (argon and 5% silane diluted in helium). Figure 2.1a shows a schematic of the experimental setup. We supplied radio frequency (rf) power at 15 W and 13.56 MHz to ring electrodes in the upper region of the glass tube to form the amorphous silicon nanoparticles. The size of the particles is controlled by adjusting the flow rate of argon gas through the reactor tube between 18 and 60 standard cubic centimeters per minute (sccm) while maintaining a constant pressure of 200 Pa. For example, the nanoparticle size is decreased by increasing the argon flow rate and consequently the argon-to-silane ratio in the plasma while the pressure and silane flow rate are kept constant. This decreases the residence time of the nanoparticles in the plasma and the partial pressure of silane, leading to the formation of smaller nanoparticles. The silane (5% diluted in helium) flow rate is kept constant at 5 sccm while the argon flow rate is set to 18, 35 and 60 sccm to form 5, 4 and 3 nm nanoparticles, respectively. The size distributions are relatively monodisperse, with a typical standard deviation of 10%.[39] An overview of the plasma

conditions can be found in Table 2.1.

Table 2.1: Overview of the plasma conditions for synthesizing 3, 4 and 5 nm nanoparticles in the primary plasma.

Nanoparticle size (nm)	Argon (sccm)	He/SiH_4 (5%) (sccm)	Pressure (Pa)	Primary plasma power (W)	Secondary plasma residence time (ms)
3	60	5	180	15	2.8
4	35	5	190	15	4.6
5	18	5	195	15	8.3

A second electrode in the lower half of the glass tube creates a second plasma with powers ranging from 5 W to 50 W, as read from the power supply. The actual plasma power will be lower due to losses in the matching network. The second plasma will couple directly to the grounded flange of the reactor. An orifice downstream of the second plasma controls the pressure and accelerates the nanoparticles into the nanoparticle collection region. A glass substrate placed at the end of a moveable pushrod and positioned below the orifice collects the nanoparticles. This substrate can be pulled into an enclosure without breaking vacuum, which allows for air-free transportation of the nanoparticles. Agglomeration of the nanoparticles is avoided by reducing the distance between the two plasmas without overlapping them. If the distance between the two plasmas is too large, the nanoparticles lose their charge and agglomerate. When the secondary plasma power is sufficiently high, these agglomerates can coalesce due to the high nanoparticle temperature leading to an apparent growth of the particles in the second plasma.[62] When all of the silane gas is consumed in the primary plasma and agglomeration is minimized, the particle size does not change in the secondary plasma.

2.2.2 Nanoparticle characterization

X-ray diffraction (XRD) from nanoparticles was collected using a Bruker-AXS Microdiffractometer with a 2.2 kW sealed Cu x-ray source. The nanoparticle diameter is calculated from the Scherrer equation. Raman scattering from the nanoparticles was collected with a Witec alpha300 R confocal Raman microscope, UHTS300 spectrometer and DV401 CCD detector. An Omnichrome argon ion laser with 514.5 nm excitation and 50 mW maximum output power illuminated the sample. Nanoparticles collected on lacy-carbon grids were examined with a Tecnai G2 F30 transmission electron microscope (TEM).

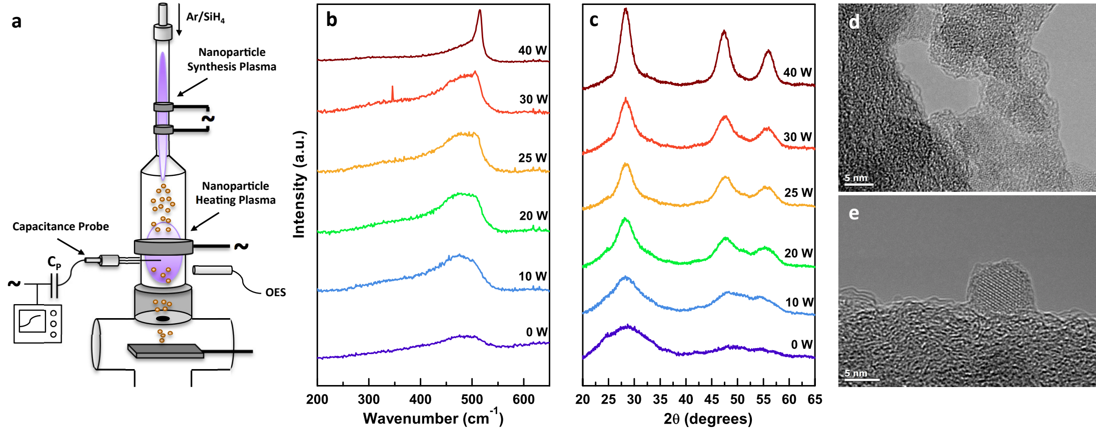

Figure 2.1: **Double plasma experiment.** **(a)** Schematic of the tandem plasma experiment used to study silicon nanoparticle crystallization. Amorphous silicon nanoparticles are formed in a low-power synthesis plasma, followed by heating in a variable-power secondary plasma. Optical emission spectroscopy and capacitance probe measurements are used to determine the properties of the secondary plasma used for heating the nanoparticles. **(b)** Raman spectra from 4 nm nanoparticles as a function of power applied to the secondary plasma. At a critical power of 30 W the crystalline silicon feature at 520 cm^{-1} emerges. **(c)** X-ray diffraction from 4 nm nanoparticles exposed to the secondary plasma as a function of secondary plasma power. Diffractions for silicon nanocrystals emerge when the plasma power exceeds 30 W. **(d)** Transmission electron micrographs of 5 nm diameter silicon nanoparticles when the secondary power is off. This yields amorphous nanoparticles. **(e)** Crystalline nanoparticles are observed in TEM once the secondary plasma power is increased to 40W.

2.2.3 Plasma analysis

The heating and cooling reactions on the nanoparticle surface are displayed schematically in Figure 2.2. These reactions depend on the electron temperature, hydrogen density and ion density. Ion densities in the second plasma are measured using an electrostatic capacitive probe.[63] The probe consists of a 5.5 mm long, 0.8 mm diameter tungsten wire connected to a 1 nF capacitor. The probe is driven by an rf power supply at 1 MHz while the voltage of the capacitor is measured with an oscilloscope. The rf generator charges the capacitor through the negative self-biasing of the probe. The signal from the rf generator is periodically chopped, resulting in discharging of the

capacitor from the positive ions collected by the probe. The rate at which the capacitor discharges is directly proportional to the ion flux,[63,64] and the ion density in the plasma can be calculated by assuming that the Bohm criterion relates the ion flux to the ion density. This approach is particularly useful for dusty plasmas, because deposition occurring on the probe itself does not affect the measurements.[63,64]

Optical emission from the second plasma is collected (see Figure 2.1a) with an optical fiber connected to the entrance slit of a monochromator. A Corona model previously discussed in[60] and not repeated here was used to interpret the emission spectrum and to obtain the atomic hydrogen density. Briefly, this Corona model assumes that the excited states are populated via direct excitations from the ground states while depopulation occurs by radiative de-excitation. The hydrogen density in the plasma can be obtained by measuring the ratio of the hydrogen emission line intensity to the argon emission line intensities. The standard deviation of the hydrogen density is obtained by comparing the hydrogen densities calculated using multiple argon/hydrogen line ratios. The electron temperature is then estimated to be the value at which the overall standard deviation is minimum.[65] For more details the reader is referred to.[60]

2.2.4 Nanoparticle heating model

The nanoparticle temperature (T_p) was calculated from the transient particle energy balance,

$$\frac{4}{3}\pi r^3 \rho C \frac{dT_p}{dt} = G - L \tag{2.1}$$

where ρ is the silicon mass density, C is the heat capacity, G is the heating term and L is the cooling term as previously described in.[60] Briefly, particles are heated through electron-ion recombination at their surface and through reactions involving hydrogen atoms, as shown in Figure 2.2. The main loss is due to conduction to the background gas. As the gas density is significantly higher than the ion density and hydrogen density, we consider this loss term as a continuous process. Radiative cooling is negligible compared to conductive cooling because the nanoparticle diameter is smaller than the emitted wavelength.[66]

As described in,[60] equation (2.1) is solved by discretizing the expression using a

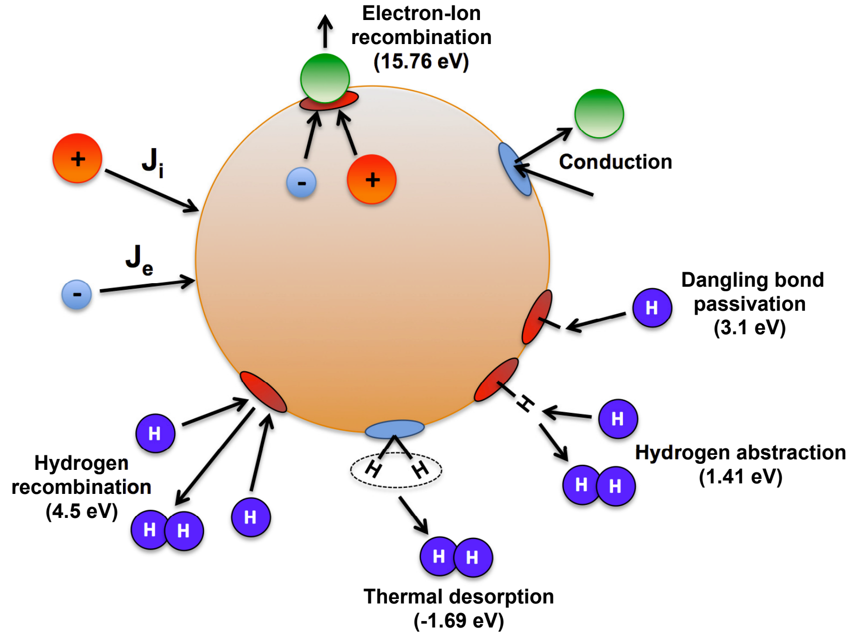

Figure 2.2: **Surface reactions.** Heating and cooling events occurring on the silicon nanoparticle surface. Heating events are indicated with red dots on the nanoparticle surface while cooling events are shown as blue dots. The electron-ion recombination energy is equal to the argon ionization potential of 15.76 eV. Dangling bond passivation, hydrogen abstraction and hydrogen recombination deliver 3.1, 1.41 and 4.5 eV, respectively. Cooling occurs mainly through collisions with colder gas atoms. At 900 K and higher, thermal desorption of hydrogen starts to play a role, where the energy loss is equal to 1.69 eV for each desorbed hydrogen molecule.

typical time step of 10^{-10} seconds. Initially the temperature of the nanoparticle is equal to the gas temperature, and the particle does not have any charge or hydrogen on its surface. A Monte Carlo approach is applied to select either an ion or electron to collide with the nanoparticle.[67] The hydrogen reactions occurring at the nanoparticle surface are evaluated from a separate secondary loop. The model keeps track of the charge, temperature, and hydrogen coverage of the nanoparticle at each time step. These quantities determine the probability of electron-ion recombination and hydrogen reactions. The input parameters such as the ion density, electron temperature and hydrogen density are obtained from the plasma diagnostics, as described in Section

2.2.3. Equilibrium conditions are reached after less than a millisecond. Further details are described in.[60] A copy of the nanoparticle heating code can be found in Appendix C.

2.3 Results and discussion

2.3.1 Nanoparticle characterization

We synthesized amorphous nanoparticles under identical conditions in the first plasma and injected them into the second plasma. We then studied whether these amorphous nanoparticles are crystallized under different plasma powers in the second plasma to study their crystallization. The nanoparticle size was varied by adjusting the argon flow rate, and experiments were conducted for 3 nm, 4 nm, and 5 nm nanoparticles. Figures 2.1b and 2.1c show the XRD and Raman spectra from 4 nm nanoparticles as a function of power used to maintain the second plasma. The XRD patterns clearly show an increase in silicon nanoparticle crystallinity as the secondary plasma power is increased. Raman scattering confirms this trend. In Figure 2.1b, the Raman scattering peak at 520 cm^{-1} originates from crystalline silicon, whereas the broad peak around 480 cm^{-1} is typically observed from amorphous silicon. These data also confirm that nanoparticles produced in the first plasma are amorphous, because there are no crystalline peaks in the XRD or the Raman spectra when the second plasma is not turned on (0 W).

Figures 2.1b and 2.1c show that above a threshold power the nanoparticles exiting the second plasma are completely crystallized. For 3 nm nanoparticles, this threshold power is 20 W; both Raman spectra and XRD show fully developed crystalline peaks at this power. The crystallization threshold power increases to 30 W and 40 W for 4 nm and 5 nm nanoparticles, respectively. The nanoparticle size and crystallinity were also characterized using TEM. For example, the bright-field images in Figure 2.1d and 2.1e show the transformation of 5 nm amorphous nanoparticles to nanocrystals. TEM images also show that the nanoparticle size does not increase significantly upon crystallization. This indicates that the nanoparticles do not coalesce or continue to grow in the second plasma. In summary, the TEM, XRD and Raman spectroscopy studies are consistent and confirm the existence of a threshold power required for crystallization.

2.3.2 Plasma properties

We measured the electron temperature (T_e), the ion density (n_i), and the hydrogen density (n_H) as a function of power used to maintain the second plasma and determined the respective values of these properties needed to crystallize the amorphous nanoparticles made in the first plasma. These values were used as inputs to our model for determining the nanoparticle temperature as a function of time during the transit through the second plasma.

Figure 2.3a shows the ion densities as a function of second plasma power for the primary plasma conditions used to produce the three different nanoparticle sizes. Hereafter and in all figures, these plasma conditions will be referred to with the size of the nanoparticles they produce. As expected, the ion density increases with increasing plasma power. The ion density increases faster with increasing power for plasma conditions under which smaller nanoparticles are synthesized. This is caused by the difference in argon flow rates. This change in argon flow rate is used to synthesize the different sized nanoparticles while maintaining a constant pressure. To decrease the nanoparticle size, the argon flow rate is increased which in turn increases the argon/silane ratio, reduces the partial pressure of silane, and decreases the nanoparticle residence time in the plasma. The resulting change in the gas composition affects the ion density and variation with plasma power.

Figures 2.3b and 2.3c show the electron temperature and the hydrogen atom density as a function of the secondary plasma power for the three different primary plasma conditions that yield 3, 4 and 5 nm silicon nanoparticles. The electron temperature found for the conditions under which 5 nm particles are produced is significantly higher compared to the others. This increase in electron temperature could be caused by the reduced argon partial pressure. As the silane is diluted in helium, the partial pressure of helium will be highest for 5 nm nanoparticles, causing an increase in electron temperature. The slight decrease in electron temperature for increasing powers can be explained by higher ion and electron densities at higher powers, leading to a lowering of the electron temperature.

The hydrogen density is also a strong function of the secondary plasma power and the primary plasma conditions used for making different size nanoparticles. For example, the hydrogen density is the largest under the conditions used for making 5 nm nanoparticles

because the silane-to-argon ratio and, consequently, the silane partial pressure are the highest. Increasing the argon flow rate dilutes the silane and the hydrogen density decreases.

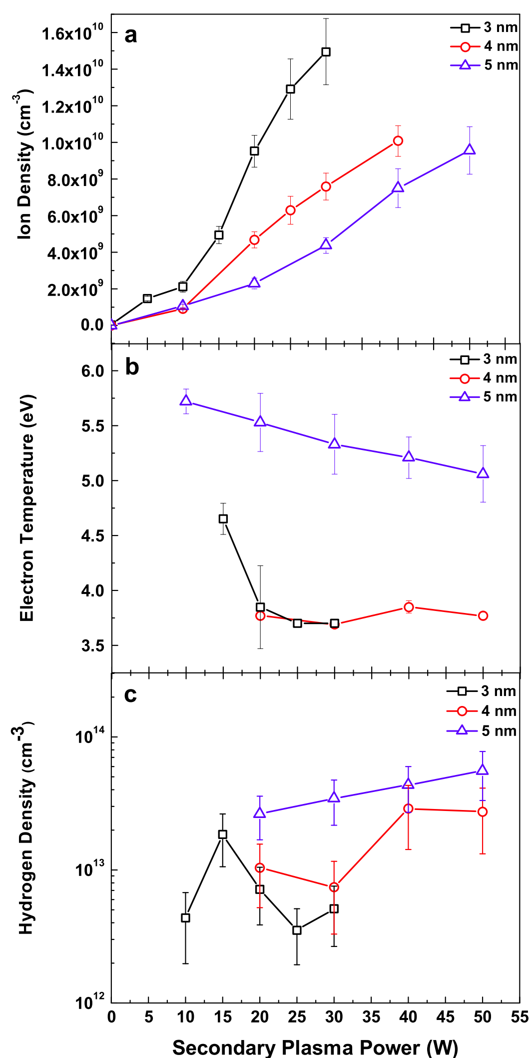

Figure 2.3: **Plasma characterization.** **(a)** Ion density, **(b)** electron temperature and **(c)** hydrogen density in the second plasma as a function of the secondary plasma power for several different conditions used to operate the primary plasma. The primary plasma conditions are referred to with the size of the nanoparticles they produce.

The gas temperature in the plasma was measured by placing a thermocouple directly into the secondary plasma. To measure the temperature the plasma was switched off briefly. The temperature values ranged from 370 K up to 430 K, depending on the applied power to the plasma. This agrees with typical gas temperatures that are found in nonthermal plasmas.[39]

2.3.3 Nanoparticle heating model

The electron temperature, ion density and hydrogen density were used as inputs to the nanoparticle heating model. Figure 2.4 shows the calculated nanoparticle temperature as a function of the three nanoparticle sizes. While the gas temperature is only 400 K, the nanoparticles reach much higher temperatures, sufficient to crystallize the amorphous nanoparticles injected from the primary plasma. The 3 nm particles show more frequent and much larger temperature fluctuations than the 5 nm particles because of their smaller mass. While the average temperature of these 3 nm particles is close to the gas temperature, the fluctuations are large enough to raise their instantaneous temperature to as high as 700 K. Conduction to the background gas causes the rapid cooling after every heating event. The temperature exponentially decays within microseconds after every heating event occurs.

Raman spectra show that a large fraction of the nanoparticles are still amorphous, even at the threshold plasma power for all three sizes. While the average nanoparticle temperature is sufficient for crystallization, there will be a distribution in both the temperature as well as the size of the nanoparticles. Thus, some fraction of the nanoparticles will still remain below the critical crystallization temperature, while a large portion reach the temperatures required for crystallization. When the power is increased further, more of the nanoparticles reach temperatures higher than the crystallization temperature and the fraction of nanocrystals increases.

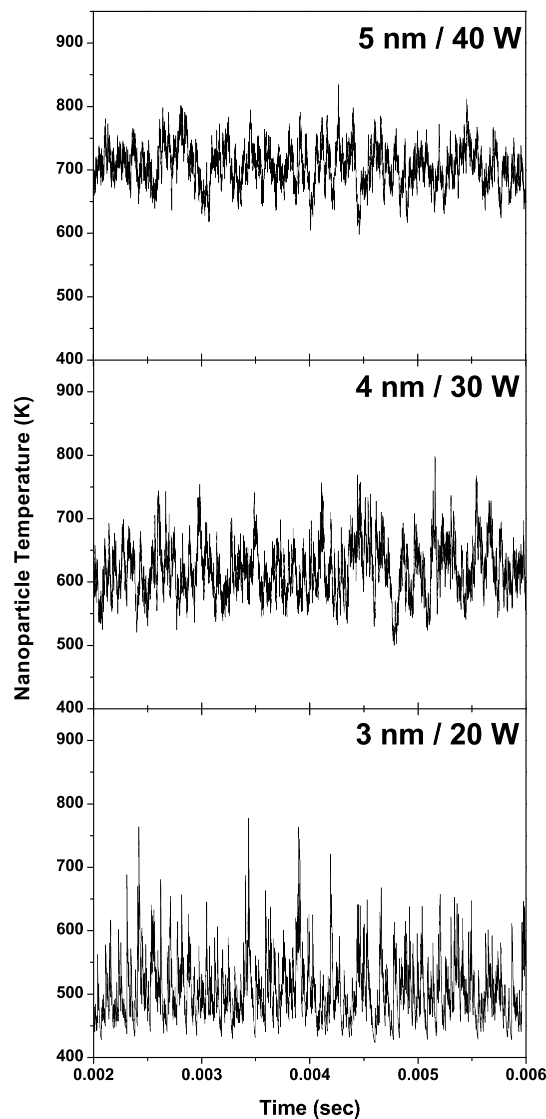

Figure 2.4: **Nanoparticle temperature fluctuations.** Time-dependence of nanoparticle temperature calculated from the transient energy balance. The temperatures of each nanoparticle with different size are evaluated at the critical power where the nanoparticles begin to crystallize. This critical power was determined from XRD and Raman scattering data. The nanoparticles in the size range of 3 to 5 nm can reach temperatures significantly above the gas temperature.

Comparison of the 4 nm nanoparticle temperature presented in Figure 2.4 with XRD and Raman spectra suggests that the critical crystallization temperature is between 600 and 700 K for 4 nm nanoparticles. This is reached when the secondary plasma power is at or above 30 W. Figure 2.5 shows the calculated nanoparticle temperatures for powers below and above this threshold power. Indeed, Figure 2.5 shows that, at 20 W, the average nanoparticle temperature decreases to approximately 550 K, well below the temperature required for crystallization. However, at higher plasma powers (40 W) the nanoparticle temperature increases to 750 K. This agrees with the trend seen from *ex-situ* nanoparticle analysis, where the nanoparticles remained amorphous for low plasma powers, indicating insufficient nanoparticle heating. This supports the hypothesis that nanoparticle heating is the mechanism for nanoparticle crystallization.

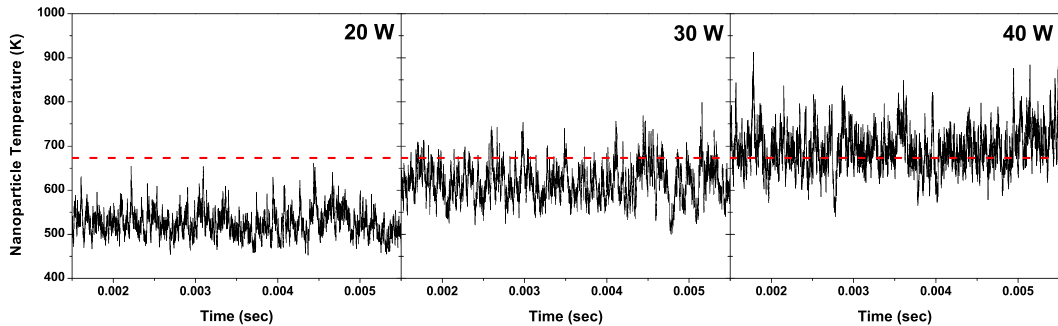

Figure 2.5: **Power dependence.** The temperature of a 4 nm silicon nanoparticle for three different secondary plasma powers. The temperature required for nanoparticle crystallization from Ref.[16] is indicated by the dashed line. The average nanoparticle temperature increases with increasing plasma powers and exceeds the crystallization temperature once the power is equal to or larger than 30 W.

Figure 2.4 also shows that the average nanoparticle temperature increases with increasing size. This increase is due to the increase in the hydrogen density and the electron temperature, as shown in Figure 2.3. As the nanoparticle mass increases, the individual stochastic recombination events and reactions that release energy do not cause significant temperature spikes anymore. However, higher electron temperature and larger hydrogen densities increase the heating rate for 5 nm particles. This increase is despite decreasing ion densities. Thus the 5 nm particles can still reach temperatures

that are sufficiently high for crystallization.

The relative importance of heating due to electron-ion recombination and heating due to reactions of radicals on the nanoparticle surface is shown in Figure 2.6 for 3 nm and 5 nm nanoparticles. For 3 nm nanoparticles, the electron-ion recombination events and hydrogen reactions both contribute about equally to the nanoparticle heating, leading to nanoparticle temperatures well above the gas temperature. When time-averaged heating contributions are calculated, the contribution of electron-ion recombination is 43% while hydrogen reactions contribute 57% of the total nanoparticle heating. However, the temperature spikes are the result of the more energetic electron-ion recombination events and enable the nanoparticles to reach temperatures of up to 700 K.

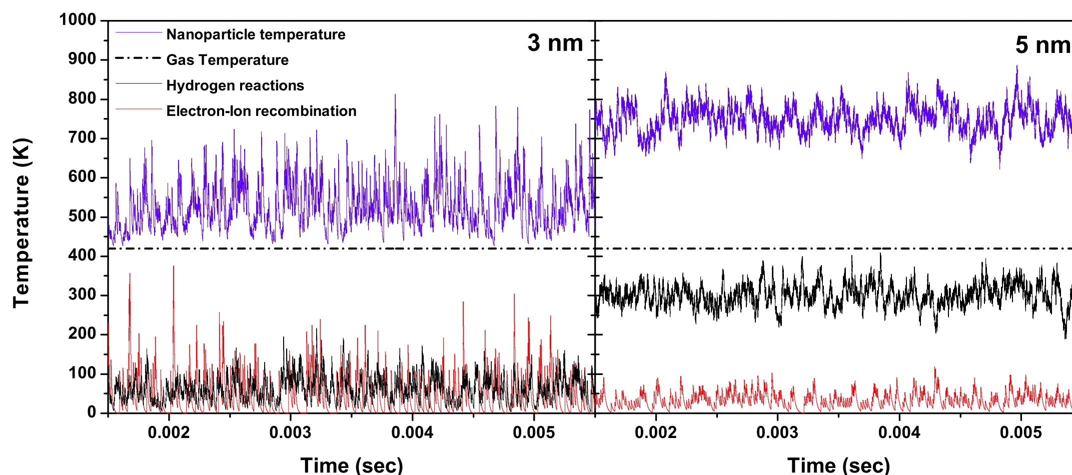

Figure 2.6: **Heating contributions.** Relative contributions of electron-ion recombination and hydrogen reactions to nanoparticle heating for 3 nm and 5 nm nanoparticles. For 3 nm nanoparticles, both electron-ion recombination and hydrogen reactions equally contribute to nanoparticle heating. For 5 nm nanoparticles hydrogen reactions dominate nanoparticle heating.

The dominant heating mechanism for 5 nm nanoparticles is different. The heating due to electron-ion recombination is reduced significantly, caused by the increase in mass of the nanoparticle and the lower ion density. The dominant nanoparticle heating mechanism is hydrogen atom reactions on the nanoparticle surface because the

hydrogen density is higher under the conditions used for synthesizing the 5 nm nanoparticles. This is the case even though the energy released for each reaction is far lower than the electron-ion recombination reactions. Integration shows that for these plasma conditions, hydrogen reactions deliver 90% of the energy to heat the particle to the crystallization temperature.

2.4 Conclusion

Here we studied the crystallization mechanism during nonthermal plasma synthesis of silicon nanoparticles. We decoupled the nanoparticle synthesis from nanoparticle heating by separating them into two separate plasma regions using a tandem plasma configuration. Using this approach, we were able to determine the electron temperature, ion density and hydrogen density required for complete crystallization of silicon nanoparticles with various sizes, and determine the physical processes that lead to nanoparticle heating. As the nanoparticles become larger, the plasma power required for crystallization increases. From *ex-situ* nanoparticle characterization we found that the critical threshold powers were 20 W, 30 W and 40 W for nanoparticle sizes of 3 nm, 4 nm and 5 nm, respectively.

The electron temperature, ion density and hydrogen density in the secondary plasma were measured using ion-flux probe and optical emission spectroscopy. Using these measured plasma properties the nanoparticle temperature is calculated by integrating the nanoparticle energy balance. It was found that the nanoparticle temperature is significantly higher than the gas temperature. For plasma conditions at which the nanoparticles become crystalline, the nanoparticles reach temperatures which are sufficient for crystallization, confirming that the nanoparticles crystallize due to heating in the plasma. For the smaller 3 nm nanoparticles, both electron-ion recombination and hydrogen reactions contribute to the increase in nanoparticle temperature. However, for 5 nm particles the main contribution to nanoparticle heating are the reactions of hydrogen atoms on the nanoparticle surface. This study allowed us to determine the necessary plasma conditions for the formation of crystalline silicon nanoparticles, and gave valuable insight into the physical origin of nanoparticle crystallization. While we focused on silicon nanoparticles, the approach used in this article is applicable to other

materials as well. Thus, this method can promote a better understanding of the general processes of particle crystallization in plasmas and could even be used to predict the viability of achieving crystalline nanoparticles of new materials via a nonthermal plasma synthesis.

2.5 Future work

Plasma synthesis of nanocrystals has proven to be a powerful synthesis method with numerous advantages over solution-based methods. In this study additional insight was obtained in the crystallization process of silicon nanoparticles in nonthermal plasmas. There is however a need for experimental verification of the temperature predictions that were obtained using the nanoparticle heating model. Unfortunately this is not an easy task, as the small size and short residence times make such an experiment tedious.

There is currently extensive modeling work in progress on the nanoparticle systems by a collaboration between the groups of Prof. Kushner (University of Michigan) and Prof. Girshick (University of Minnesota). The goal is to model the nonthermal nanocrystal synthesis plasma from top to bottom. A comparison between the model predictions and the experimentally acquired values in this study would be of great value.

An alternative is to investigate the crystallization of other materials besides silicon. The Kortshagen group is able to produce a wide range of materials that all rely on the unique plasma chemistry. The model can be adjusted to include the change in gas species and plasma characteristics. Germanium would be a good candidate as it is very similar to silicon and easy to set up. An agreement between the crystallization behavior of silicon and germanium would provide additional confidence in the heating model of this study.

Finally an area that remains unexplored is gas heating. Instead of having the plasma heat the nanoparticles in order to crystallize them, hot gasses can be injected into the plasma or the gas can be externally heated to provide energy for crystallization. To avoid agglomeration or sintering at high temperatures a low-power plasma should be maintained in the region of elevated temperature. Such an experiment would also help validate the nanoparticle heating model that was presented in this work.

Acknowledgements

This work was supported in part by the DOE Plasma Science Center for Predictive Control of Plasma Kinetics. Partial support by the NSF/DOE Partnership in Basic Plasma Science through grants DOE/DE-SC0002391 and NSF CBET-0903842 is acknowledged, which provided support for NK, MM and URK. Parts of this work were carried out in the Characterization Facility, University of Minnesota, which receives partial support from NSF through the MRSEC program.

Chapter 3

Requirements for Plasma Synthesis of Nanocrystals at Atmospheric Pressures†

3.1 Introduction

Plasma synthesis and crystallization of nanoparticles is an exciting new frontier both for plasma science as well as materials research. The unique ability of plasmas to produce nanocrystals of high melting point materials through selective nanoparticle heating in a background gas that remains at room temperature has already enabled the high throughput synthesis of a wide range of semiconductor nanocrystals.[39,44,68–71] Low pressure plasmas have also been used to dope nanocrystals and to decorate their surface with organic ligands.[21,27,54,72–75] While there are already some industrial applications of low pressure plasma synthesized nanocrystals,[76] such as silicon inks for solar cell applications, some applications may benefit from the lower cost generally associated with atmospheric plasma processing.

Nanoparticle heating in the plasma is crucial for nanocrystal synthesis of high melting point semiconductors. A key question is whether adequate nanoparticle heating can

†Portions of this chapter have been published in the manuscript by Nicolaas J. Kramer, Eray S. Aydil and Uwe R. Kortshagen in Journal of Physics D: Applied Physics (doi:10.1088/0022-3727/48/3/035205, 2015)

be achieved at atmospheric pressure to induce the crystallization of nanoparticles that nucleate and grow in the plasma. To date, the mechanisms of nanoparticle charging and heating in nonthermal plasmas have only been studied at low pressures.[15,77–79] It was found that exothermic electron-ion recombinations and hydrogen atom reactions on the surface of the nanocrystal can heat the nanoparticles that have nucleated and grown in the plasma to temperatures that exceed the temperatures required for crystallization. Collisions with electrons also ensure that the nanocrystals are negatively charged which significantly reduces agglomeration in the plasma. Understanding the kinetics of the interactions of electrons, ions and hydrogen atoms with nanocrystals during synthesis is critical for designing an effective synthesis system.

Recent studies have shown that silicon nanocrystals with very narrow size distributions can be synthesized using atmospheric plasmas.[80,81] The fundamental processes that lead to nanoparticle charging and heating are significantly different at atmospheric pressure than at low pressures. At atmospheric pressure, particles acquire charge through hydrodynamic, mobility driven collection of ions rather than through orbital motion which is prevalent at low pressures. Moreover, nanoparticle heating reactions have to compete with strong nanoparticle cooling through convection and conduction to the neutral gas which is about 100-1000 times faster at atmospheric pressure than at low pressures.

A number of sophisticated models for particle charging over a wide range of pressures have been developed in the literature on dusty plasmas[82–84] and aerosols.[85,86] Gatti and Kortshagen developed a simple analytical model which accurately predicts the collision frequency of ions with particles for pressures between 10^{-5} and 10^{5} Pa.[87] This model describes a wide range of collision regimes, ranging from the collisionless orbital motion limited (OML) regime[88] to the highly collisional hydrodynamic regime.[82] The ion current to the nanoparticles was taken to be the sum of three components: the collisionless OML current, the collision-enhanced transition regime current, and the hydrodynamic current over the collisional regime. These three components are weighted with their respective probabilities of ions performing zero (OML), one (Collision-Enhanced), and more than one collision (Hydrodynamic) within a sphere around the particle defined by the capture radius. Within this capture radius, ions undergo charge-exchange collisions

with neutrals but are eventually captured by the particle. This model allows one to accurately predict the nanoparticle charge and ion collision frequency at pressures ranging from very low to atmospheric. Accurate modeling of particle charge and ion collision frequencies across a wide range of pressures also enables the estimation of nanoparticle temperatures for a wide range of pressures and plasma conditions.

Here, making use of the Gatti and Kortshagen model, a nanoparticle heating and charging model is presented that is applicable over a wide range of pressures. Nanoparticle heating reactions such as electron-ion recombination and exothermic hydrogen surface reactions are treated stochastically through a Monte Carlo approach while nanoparticle cooling through conduction and convection is modeled using a continuum approach. The model provides insight into the plasma requirements for synthesizing semiconductor nanocrystals at atmospheric pressure. In addition, using our model, we estimate the temperature and charge distribution of silicon nanocrystals in atmospheric plasmas based on experimentally determined conditions from literature.

3.2 Simulation Details

3.2.1 Nanoparticle Charging

We simulated the charge and temperature of silicon nanoparticles with diameters between $3 - 50$ nm for plasmas maintained at pressures ranging from $1 - 10^5$ Pa. In order to calculate the net charge on the nanoparticles, we calculated both the electron and ion current collected by the nanoparticle. For pressures considered here, the ion current to the particle depends on charge-exchange collisions. However, the electron current collected by the particle can be considered close to that given by an equilibrium distribution of electrons in the repulsive potential around the particle. Assuming a Maxwell-Boltzmann electron energy distribution, the electron current can be calculated from

$$I_e = \pi a^2 n_e \left(\frac{8kT_e}{\pi m_e}\right)^{\frac{1}{2}} exp\left(\frac{eV_P}{kT_e}\right) \tag{3.1}$$

where T_e and m_e are the electron temperature and mass, a is the nanoparticle radius, n_e is the electron density and V_P is the nanoparticle potential.

The electron density is calculated using the electroneutrality condition,

$$n_e = n_i - Qn_p, \tag{3.2}$$

where n_i is the ion density, n_p is the nanoparticle density, and Q is the average charge per nanoparticle.

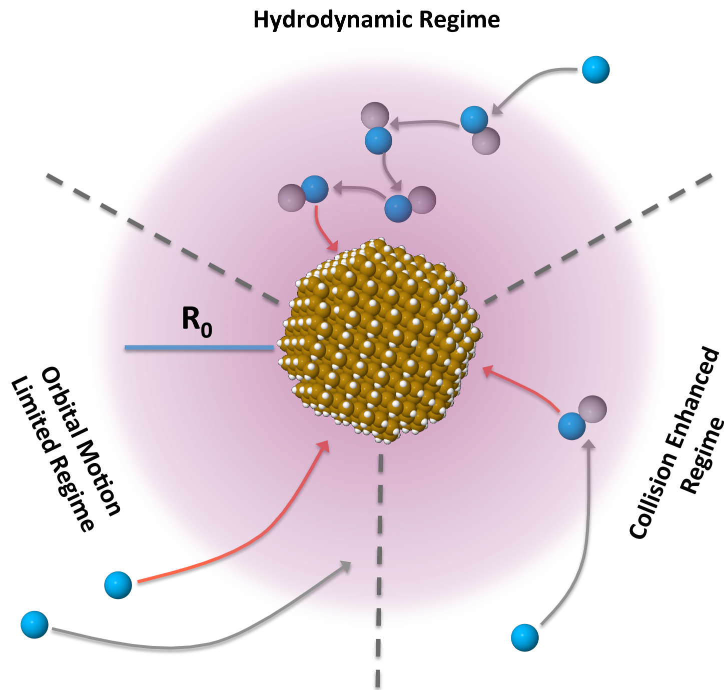

Figure 3.1: **Collisionality regimes.** Schematic illustration of the three collisionality regimes considered in the nanoparticle heating and charging model. Within the capture radius R_0 ions undergo charge-exchange collisions and will eventually be collected by the nanoparticle. In the three regimes considered the ions undergo zero (OML), one (Collision Enhanced), or more than one (Hydrodynamic) collisions within this sphere around the silicon nanoparticle.

The ion current collected by the nanoparticle is calculated using the model developed by Gatti and Kortshagen.[87] In this model the ion current is comprised of three components: a collisionless OML current, an intermediate collision-enhanced transition regime current, and the hydrodynamic current for the highly collisional regime. These regimes are illustrated schematically in Figure 3.1. The three components of the ion current are weighted by the probabilities P_0, P_1 and $P_{>1}$, which quantify, respectively, the probability of an ion approaching the particle to undergo zero, one, or more than one collisions inside the capture radius. The capture radius, R_0, of an ion with kinetic energy E_{kin} is defined through the equation $E_{kin} + U(R_0) = 0$, where $U(r)$ is the potential energy of the ion approaching the nanoparticle.[89] Approximating $U(r)$ with the linearized Yukawa potential gives the expression[87]

$$R_0(E_{kin}) = \frac{e|V_P|a\left(1 + \frac{a}{\lambda_{DL}}\right)}{E_{kin} + e|V_P|\frac{a}{\lambda_{DL}}} \approx \frac{e|V_P|a}{E_{kin}}. \tag{3.3}$$

In equation (3.3) λ_{DL} is the linearized Debye length.[90] The simplified expression is valid for small nanoparticles with $a \ll \lambda_{DL}$. Accounting for all three components of the ion current allows us to accurately calculate the ion current for a wide range of pressures and nanoparticle sizes. With these assumptions, the ion current collected by the nanoparticle can be written as

$$I_i = P_0 I_i^{OML} + P_1 I_i^{CE} + P_{>1} I_i^{HY}, \tag{3.4}$$

where the OML, the collision-enhanced and the hydrodynamic ion currents are[89]

$$I_i^{OML} = \pi a^2 \nu_{i,th} n_i \left(1 - \frac{eV_P}{kT_i}\right), \tag{3.5}$$

$$I_i^{CE} = \pi(\alpha R_0)^2 n_i \nu_{i,th}, \tag{3.6}$$

$$I_i^{HY} = 4\pi a n_{i,0} \mu_i |V_P|. \tag{3.7}$$

In equation (3.5)-(3.7) n_i is the ion density, $\nu_{i,th}$ is the thermal velocity of the ions, and μ_i is the ion mobility. The corresponding probabilities are calculated from[91]

$$P_0 = exp\left(-\frac{\alpha R_0}{\lambda_i}\right), \tag{3.8}$$

$$P_1 = \frac{\alpha R_0}{\lambda_i} exp\left(-\frac{\alpha R_0}{\lambda_i}\right), \tag{3.9}$$

$$P_{>1} = 1 - P_0 - P_1. \tag{3.10}$$

The factor $\alpha = 1.22$ is a result of the energy dependence of the capture radius when averaged over a Maxwellian distribution of ion energies, while λ_i is the collision mean free path of the ions.

3.2.2 Nanoparticle Heating and Cooling

Using the rates for electron and ion collection by the particle discussed above we can calculate the nanoparticle temperature (T_p) by solving the transient energy balance on the nanoparticle:

$$\frac{4}{3}\pi r^3 \rho C \frac{dT_p}{dt} = G - L. \tag{3.11}$$

In this balance, ρ is the silicon mass density, C is the heat capacity, and G and L are the heating and cooling rates, respectively, as discussed in references[60] and.[77] Briefly, particles are heated through electron-ion recombination and exothermic hydrogen atom reactions on their surface. The main energy loss mechanism is by conduction and convection to the background gas, which is treated using a continuum model. Radiative cooling is negligible compared to conduction and is not included in this model.[79]

Equation (3.11) is solved by discretizing the expression using a time step of 10^{-12} seconds.[60] A small time step is required for high pressure simulations, because the collision frequency and cooling rate are significantly higher than those at low pressures. Using a Monte Carlo approach, the model selects either an ion or an electron to collide with the nanoparticle.[67] The hydrogen reactions occurring at the nanoparticle surface are determined using a separate Monte Carlo loop. The charge, the temperature, and the hydrogen coverage of the nanoparticle are tracked as a function of time and updated at each time step. These quantities determine the probability of an electron or an ion

colliding with the nanoparticle and the type of hydrogen reactions that occur on the nanoparticle surface. The input parameters to the simulation are the ion density, the electron temperature and the hydrogen density. These input parameters were varied systematically to study the effects of plasma conditions on nanoparticle heating for a range of pressures. Specifically, we focussed on determining the plasma conditions needed for sufficient nanoparticle heating to induce crystallization. Further details of the nanoparticle heating model are described in.[60] See Appendix C for a copy of the nanoparticle heating code.

3.3 Results and Discussion

3.3.1 Nanoparticle Heating

Figure 3.2a shows the effect of the ion density on the nanoparticle temperature in plasmas maintained at low pressure (10^2 Pa) and at atmospheric pressure (10^5 Pa). The nanoparticle density, the hydrogen density and the electron temperature were kept constant at values shown on the respective figures. Low pressure plasmas used for nanocrystal synthesis typically operate at a pressure of approximately 10^2 Pa. The average nanoparticle temperatures predicted by the model are plotted as bold lines while the ranges of stochastic temperature variations are shown by the shaded areas. The dotted line at $\sim$770 K is the experimentally determined temperature required to crystallize 5 nm silicon nanoparticles.[16] Increasing the ion density increases the frequency of electron-ion recombinations on the nanoparticle surface which in turn raises the nanoparticle temperature. It is clear from Figure 3.2a that, in order to reach the temperatures required for crystallization, significantly higher ion densities are required in plasmas maintained at atmospheric pressure compared to low pressure. This is a consequence of the much faster cooling rate at atmospheric pressure, which will be discussed shortly. While not shown, we found that increasing the electron temperature also increases the ion current and results in higher nanoparticle temperatures.

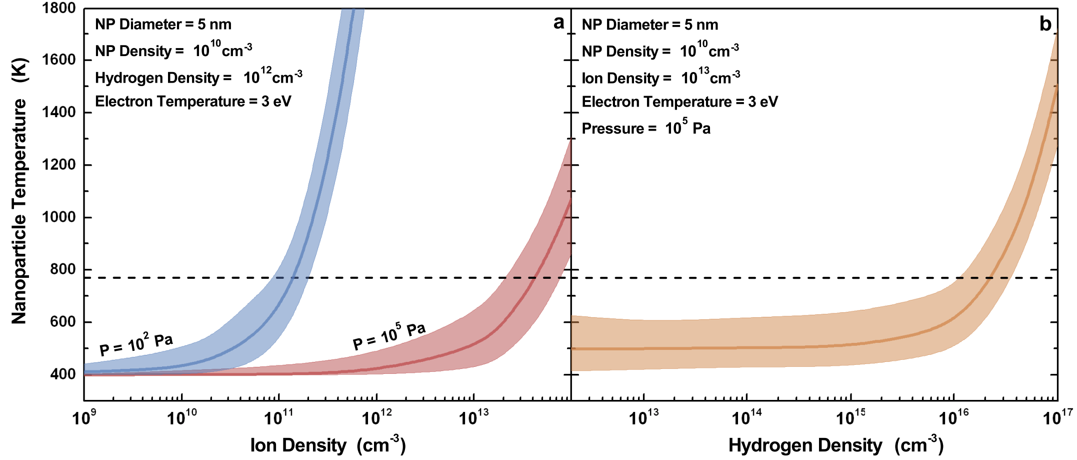

Figure 3.2: **Nanoparticle temperature.** **(a)** Nanoparticle (NP) temperature as a function of the ion density for a 5 nm silicon nanoparticle at 10^2 Pa and at 10^5 Pa. The dotted line at 770 K represents the experimentally determined temperature required to crystallize 5 nm silicon nanoparticles.[16] For the low-pressure plasma (10^2 Pa) an ion density of 10^{11} cm^{-3} is required for crystallization. This value increases significantly to 4×10^{13} cm^{-3} for atmospheric pressures. **(b)** Effect of the hydrogen density on the nanoparticle temperature at atmospheric pressure (10^5 Pa). Exothermic reactions with hydrogen atoms on the surface of the nanoparticle heats the nanoparticles. These reactions become significant after the hydrogen density exceeds 10^{16} cm^{-3}.

The hydrogen density also plays an important role in nanoparticle heating. Figure 3.2b shows the nanoparticle temperature as a function of the hydrogen density for a plasma maintained at atmospheric pressure. Increasing the hydrogen density increases the rate of exothermic hydrogen reactions on the nanoparticle surface. This in turn increases the nanoparticle temperature. A higher hydrogen density can be realized by addition of hydrogen gas during nanoparticle synthesis or by increasing the silane flow rate.

Figure 3.3 shows the temperature as a function of time for 5 nm silicon nanoparticles at two different pressures, 10^2 and 10^5 Pa. These simulations were conducted under plasma conditions where the nanoparticle temperature is close to that required

for crystallization (see Figure 3.3 caption for conditions). Note the difference in the time scales in the graphs for 10^2 and 10^5 Pa. The nanoparticle temperature is significantly higher than the gas temperature in both cases but the temperature fluctuations are much stronger at atmospheric pressure. At atmospheric pressure the nanoparticles cool 100-1000 times faster than at low pressure (10^2 Pa). This difference in the cooling rate is clearly visible when the nanoparticle temperatures at atmospheric and at low pressure are plotted on the same time scale as shown in Figure 3.4 for 3 nm silicon nanoparticles. In order to compare the results for the two pressures, the ion density, the electron temperature and the hydrogen density were kept constant (see Figure 3.4 caption). In the plasma maintained at atmospheric pressure, the nanoparticle temperature increases sharply when an exothermic electron-ion recombination or hydrogen reaction occurs on its surface. However, the nanoparticle also cools down rapidly to the gas temperature. The nanoparticle temperature increases to a similar value in the plasma maintained at low pressure but cooling is much slower. The result is a higher time-averaged nanoparticle temperature, because the next heating event can occur before the nanoparticle temperature decreases to the gas temperature. Consequently, a much higher ion density is required at atmospheric pressures in order to compete with rapid cooling and to raise the nanoparticle temperature to levels needed for crystallization.

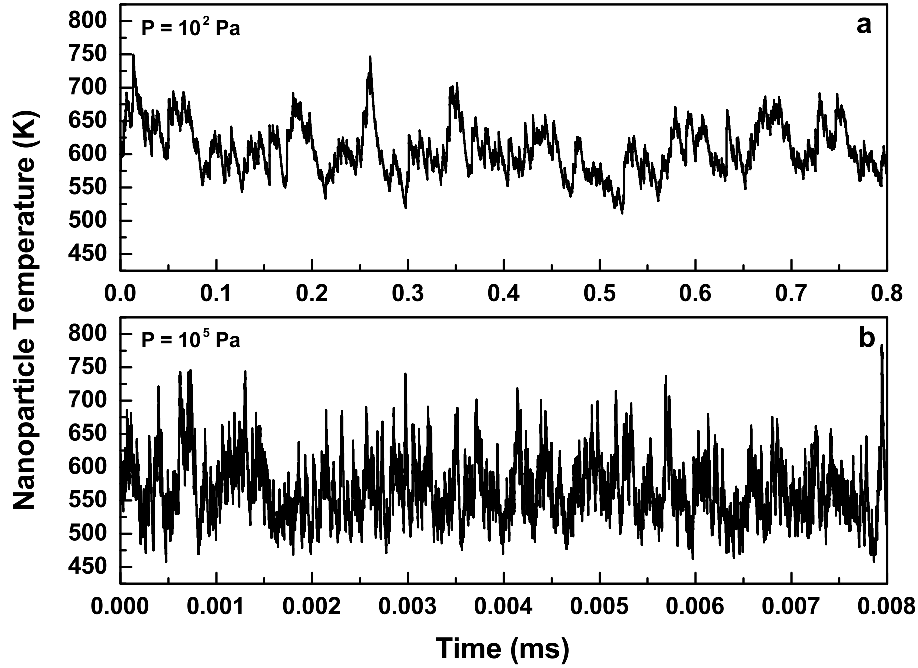

Figure 3.3: **Nanoparticle temperature variations.** Comparison of the temperature variations of the silicon nanoparticles in plasmas maintained at **(a)** 10^2 Pa and **(b)** 10^5 Pa. At atmospheric pressure (10^5 Pa, $n_i = 4 \times 10^{13}$ cm^{-3}, $T_e = 3eV$ and $n_H = 10^{13}$ cm^{-3}) nanoparticle cooling is faster than that at low pressure (10^2 Pa, $n_i = 10^{11}$ cm^{-3}, $T_e = 3eV$ and $n_H = 10^{13}$ cm^{-3}) (note the difference in time scales in (a) and (b)). In addition, the ion current is enhanced due to an increased ion density and a larger contribution from the hydrodynamic collisional regime. Consequently, the temperature fluctuations are significantly stronger.

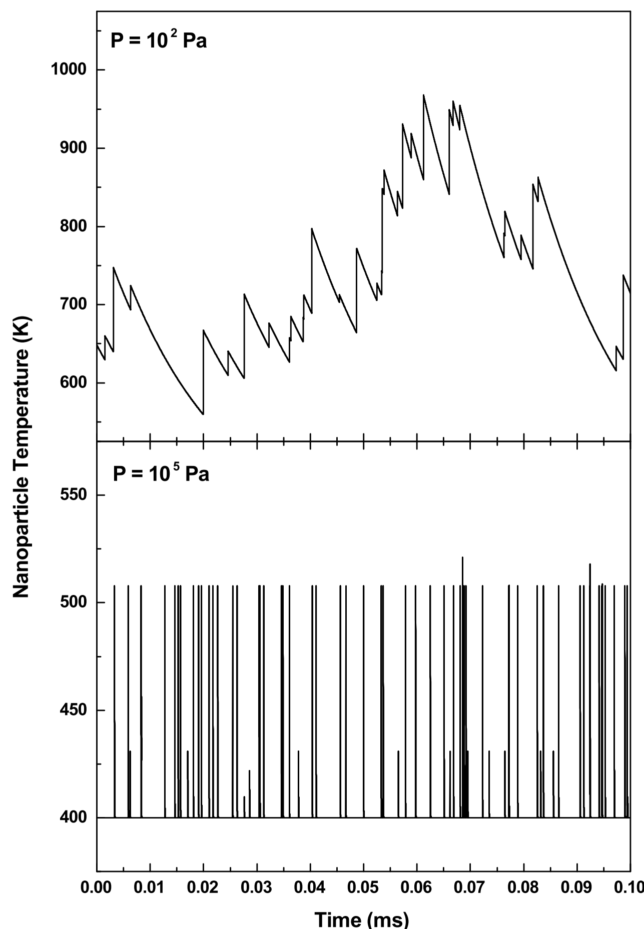

Figure 3.4: **Pressure dependence of temperature variations.** Temporal variation of the nanoparticle temperature at low (10^2 Pa) and atmospheric (10^5 Pa) pressure on common time scale showing the rate at which nanoparticle temperatures fluctuate. Here the ion density is 10^{11} cm^{-3}, the nanoparticle density is 10^8 cm^{-3}, the electron temperature is 3 eV, the hydrogen density is 10^{13} cm^{-3} and the nanoparticles have a diameter of 3 nm. Each instantaneous temperature spike corresponds to an electron-ion recombination or exothermic hydrogen reaction. Under identical plasma conditions, the nanoparticle temperature remains higher at low pressures because additional electron-ion recombination and exothermic hydrogen reactions occur before the nanoparticle cools. At atmospheric pressures the nanoparticle temperature increases briefly and quickly cools to the gas temperature.

3.3.2 Collisional Regimes

Next we analyze the relative importance, as a function of pressure, of the three mechanisms that contribute to the ion current collected by the nanoparticles. Figure 3.5 shows the nanoparticle temperature as a function of the ion density for 5 nm silicon nanoparticles at three different pressures (10, 10^3 and 10^5 Pa). For the *combined* curve, the nanoparticle temperature was calculated by summing contributions from all three mechanisms with respective currents multiplied by the corresponding probabilities (equation 3.4). The total ion current captured by the nanoparticle is the sum. The other three curves were calculated by forcing one of the three regimes in the nanoparticle heating model and using only one of the three ion current components in the simulation. This was done by setting the respective probability to 1 for each of the mechanism while setting the remaining two to zero. At low pressure (10 Pa), the *combined* nanoparticle temperature curve closely follows that predicted using only the OML current. However, when the pressure is increased to 10^3 Pa, the model deviates significantly from the values predicted using only the OML current. Using only the OML current at the intermediate pressure regime significantly underpredicts the nanoparticle temperature at intermediate pressures. This illustrates the importance of collisions within the capture radius and the shortcomings of the OML theory at higher pressures. At atmospheric pressure, the hydrodynamic contribution to the ion current is greatest. As a result the ion current collected by the nanoparticle is higher compared to the current predicted by the OML and collision-enhanced theories in the low and intermediate pressure regimes, respectively. Consequently, the nanoparticle temperature is also higher. While the ion mobility decreases with increasing pressure, the nanoparticle potential will increase as well, allowing the hydrodynamic ion current to remain larger than the OML and collision-enhanced current at atmospheric pressures.

Figure 3.5 also shows the importance of including all three regimes rather than relying solely on the OML theory at low pressures or solely the hydrodynamic ion current at high pressures. All three mechanisms need to be considered in order to calculate an accurate nanoparticle temperature. This is especially true for intermediate pressures, where all three components contribute to the ion current. These contributions also change as a function of the nanoparticle size. For example, for larger nanoparticles, the hydrodynamic contribution will increase at lower pressures. For smaller nanoparticles

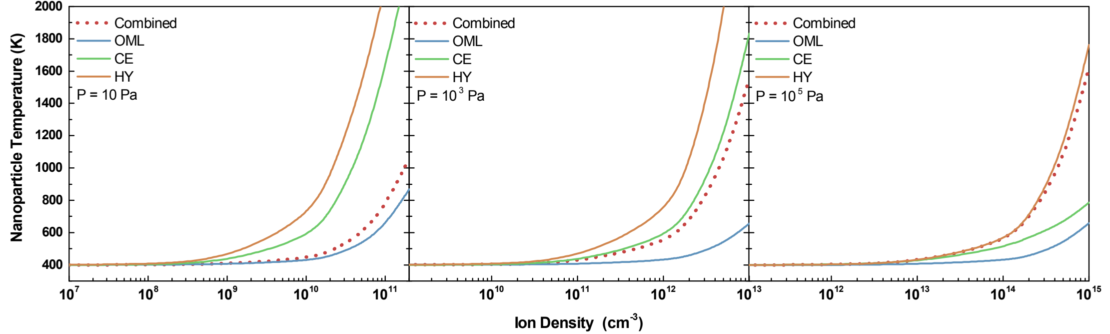

Figure 3.5: **Importance of collisionality regimes.** Comparison of the ion current collection mechanisms to nanoparticle heating for three plasma pressures. In each case, the nanoparticle temperature is shown as a function of the ion density. For the *combined* curve (dotted line) all three mechanisms are included using the probabilities for each regime (equations 8-10). The other curves are the result of calculating the nanoparticle temperature while forcing a specific regime (see text). At low pressures the combined curve follows that predicted by using only the ion current predicted by the OML theory. At intermediate pressure (10^3 Pa), the combined curve shifts closer to the curve predicted by the collision-enhanced (CE) ion current. At atmospheric pressure, the combined curve is mainly predicted by using the hydrodynamic (HY) ion current.

on the other hand the OML contribution becomes more important.

3.3.3 Charge Distribution

Nanoparticle charging in the plasma is responsible for achieving monodisperse size distributions because repulsion between charged particles reduces agglomeration. Thus it is important to understand the effect of pressure on the charge distribution. The charge distributions at 10^2 and 10^5 Pa are shown in Figure 3.6 for four different nanoparticle sizes. All other plasma parameters input into the model were kept constant and were the same as listed on Figure 3.6. Comparing the charge distributions at these two pressures shows that the average charge on the nanoparticle and the entire distribution shift to lower values when the pressure is increased from 10^2 to 10^5 Pa. The average number of charge that the nanoparticles acquire at 10^5 Pa is approximately half of what they acquire at 10^2 Pa. This is a result of the larger ion current collected by the nanoparticles at atmospheric pressure. At atmospheric pressure, the hydrodynamic ion current

contribution is larger than that from the OML current (see Figure 3.5), resulting in a decrease of the net negative charge that the nanoparticles acquire in the plasma. The average and the entire distribution shifts to higher values with increasing nanoparticle size at both pressures because the electron current collected by the nanoparticle increases with increasing size. The smaller charge at atmospheric pressure may result in increased agglomeration.

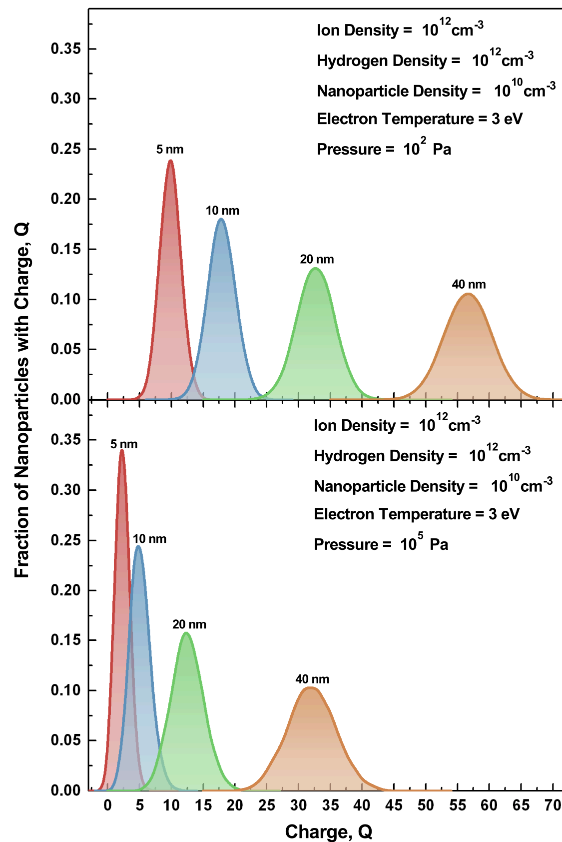

Figure 3.6: **Charge distribution**. Normalized charge distribution of silicon nanoparticles in plasmas maintained at low pressure (10^2 Pa) and at atmospheric pressure (10^5 Pa) for four different nanoparticle sizes. The increase in the ion current collected by the nanoparticle at atmospheric pressure reduces the negative charge (Q) on the nanoparticles. For a given size, the negative charge on the nanoparticles is smaller at atmospheric pressure than at low pressure.

3.3.4 Case Study

Finally we used experimentally measured plasma properties reported in the literature to estimate the temperature of silicon nanoparticles synthesized at atmospheric pressures. Nozaki *et al.* reported the formation of silicon nanocrystals with a diameter of 3 nm using an atmospheric pressure microplasma.[81] We used the experimental conditions and plasma properties in our nanoparticle heating model to gain insight into the effect of the plasma conditions on the nanoparticle crystallinity. Nozaki *et al.* reported electron densities ranging from 2×10^{14} cm^{-3} to 1.1×10^{15} cm^{-3} and an electron temperature of approximately 0.5 eV.

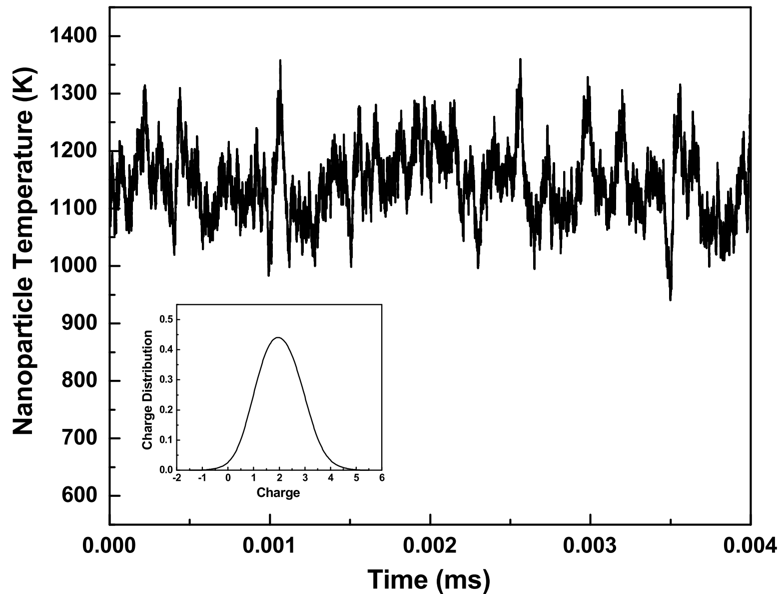

Figure 3.7: **Case study.** Nanoparticle temperature as a function of time during atmospheric pressure synthesis under experimental conditions reported by Nozaki *et al.*[81] The nanoparticles reach temperatures that exceed the crystallization temperature for 3 nm silicon nanoparticles. The inset shows the charge distribution of the nanoparticles in the plasma. As a result of the low electron temperature (0.5 eV) and high ion density (10^{15} cm^{-3}) the nanoparticle charge is low.

The nanoparticle temperature predicted by our model using these values is shown in Figure 3.7 as a function of time. We find an average temperature of approximately 1150 K which is well above the temperature required for crystallization of silicon nanoparticles. While the electron temperature is relatively low, it is compensated by a large ion density which helps nanoparticles reach high temperatures. However, the low electron temperature and high ion density also result in a very low nanoparticle charge. The charge distribution for these conditions are shown in the inset of Figure 3.7. The model predicts that the nanoparticles obtain on average only 2 charges.

3.4 Conclusion

We developed a heating and charging model for silicon nanoparticles that may be used under a wide range of pressures and plasma conditions. Using this model we examined the conditions required to heat nanoparticles in plasmas maintained at atmospheric pressure to sufficiently high temperatures for crystallization during their synthesis. For 5 nm silicon nanoparticles, ion densities greater than 10^{13} cm^{-3} or hydrogen densities exceeding 10^{16} cm^{-3} are required for nanoparticle crystallization. These values are significantly higher than those required for low pressure plasmas. Fast heating by ion and hydrogen reactions are required to compete with the faster cooling rate at atmospheric pressure.

The model also gave insight into the importance of including all the relevant collisionality regimes to calculate the ion current collected by the nanoparticles. The model covers a wide range of collisionality from the collisionless (OML) regime to the highly collisional hydrodynamic regime. The ion current collected by the nanoparticle in the lowest pressure regime is accurately described by OML theory. For nanocrystal synthesis at atmospheric pressures on the other hand, we found that the hydrodynamic contribution to the ion current is the most important. This also affects the charge distribution of the nanoparticles at atmospheric pressures, as the ion current to the nanoparticle is increased resulting in a smaller nanoparticle charge.

Finally we estimated the nanoparticle temperature in atmospheric plasmas by using published experimental data on plasma properties. The model predicted that the

nanoparticle temperature can indeed exceed the crystallization temperature at atmospheric pressure. While we focused on silicon nanoparticles, the approach is applicable to other materials as well.

The results of this study provide insight into the plasma conditions needed when designing an atmospheric pressure plasma nanocrystal synthesis reactor. Knowledge of the ion density, electron temperature and hydrogen density allows for the estimation of the nanoparticle temperature during synthesis. Suitable plasma conditions can therefore be chosen when designing a nanocrystal synthesis reactor operating at atmospheric pressures. A plasma that achieves ion densities exceeding 10^{13} cm^{-3} or hydrogen densities of 10^{16} cm^{-3} or higher is recommended for high melting-point materials such as silicon. Experimental verification of the theoretical estimations of the nanoparticle temperature during atmospheric pressure synthesis is highly desirable. Investigating the change of nanoparticle properties as a function of plasma conditions would be a first step in achieving this.

3.5 Future work

Atmospheric plasmas have been applied in numerous applications in recent years. Examples are plasma medicine applications such as wound treatment where atmospheric pressures cannot be avoided. However, very little work has been reported for nanocrystal synthesis using atmospheric plasmas. This computational study explored the required plasma conditions for silicon nanocrystal synthesis at atmospheric pressures. A comparison with experiments is however highly desired in order to further validate this model. Graduate student Narula Bilik is currently designing such an experiment, where silicon nanocrystals will be produced at atmospheric pressures. Not only is the crystal structure of the nanoparticles important, the predicted agglomeration of nanoparticles as a result of a low number of electronic charges on the nanoparticles should also be explored. These experiments would be able to further validate the model that was presented in this work.

Exploring the synthesis of new materials using atmospheric pressure plasmas is another exciting area of research. The first step is to design a reactor that is able to

produce high quality and uniform nanocrystals. The biggest challenge will be to design a stable and uniform plasma with a high nanoparticle production yield. At high pressures filamentary plasmas are often observed. These should be avoided in order to obtain a uniform plasma which is necessary for consistent nanocrystal production. Once this is established, new materials can be explored which would be very interesting for industrial applications. Examples are aluminum-doped zinc oxide nanocrystals for transparent conductors or silicon-germanium nanocrystals for thermoelectric materials.

Atmospheric pressure plasmas also allow for the use of advanced aerosol tools such as dynamic mobility analyzers. The nanoparticles can be flown directly into these aerosol instruments for size determination and size selection, which is hard to achieve with conventional low-pressure plasmas. Now the size can be directly analyzed and tuned while operating the plasma, and a much smaller size distribution can be obtained directly from the gas phase by size selection. This would make the plasma synthesis technique of nanocrystals even more powerful.

Acknowledgements

This work was supported by the DOE Plasma Science Center for Predictive Control of Plasma Kinetics.

Chapter 4

Doping of Silicon Nanocrystals†

4.1 Introduction

Now that we obtained a better understanding of the plasma synthesis of silicon nanocrystals (Si NCs), the next step is to investigate and enhance the electronic properties of these Si NCs. This will be the main focus for the second half of this thesis. In order to further tune the electronic properties of NCs, understanding the controlled incorporation of dopants is essential. Doping of semiconductor NCs is of great interest for increasing the performance of devices as it adds additional control of the number of carriers and the Fermi level in nanocrystal films.[55] However, effective doping of semiconductor NCs remains a challenge. Due to the small size of the NCs, the introduction of a few impurity atoms may lead to their expulsion to the surface (so-called self-purification) or compromise the crystal structure.[55,92] Therefore only a fraction of the dopants atoms are electronically active whereas the majority of the dopant atoms are expected to remain on the NC surface. Impurities also inherently create a heavily doped NC under strong quantum confinement, and the electronic and optical properties in those circumstances are significantly different compared to pristine NCs.

Colloidal synthesis techniques have been successful in forming high quality NCs but have only recently been able to dope CdSe[93–95] and PbSe NCs.[96,97] Gas-phase plasma

†Portions of this chapter have been published in the manuscript by Ryan Gresback, Nicolaas J. Kramer, Yi Ding, Ting Chen, Uwe R. Kortshagen and Tomohiro Nozaki in ACS Nano. (doi:10.1021/nn500182b, 2014)

synthesis methods[98] on the other hand have been successfully applied for both n-type and p-type doped NCs. Here doping is achieved by simply introducing the gaseous dopant precursors in the gas-phase during nanoparticle formation.[27,73,99]

In this chapter the *in situ* doping of plasma synthesized silicon nanocrystals with phosphorus and boron is discussed. By using Field-Effect Transistor (FET) measurements we were able to investigate the electronic activation as well as obtain the carrier mobility and Fermi level of boron and phosphorus-doped Si NCs. We investigate two sizes of Si NCs, namely, large (8-12 nm) and small (4-7 nm), to elucidate potential size-dependent effects. Degenerately-doped Si NCs also gave rise to localized surface plasmon resonances (LSPR), which will be discussed in more detail in Chapter 5. Not only did the dopants affect the electronic properties of the NCs, the dopant atoms also proved to be extremely valuable for the formation of stable NC solutions without the need of ligands by placing boron on the NC surface. This will be further discussed in Chapter 6.

4.2 Solution-Processed Field Effect Transistors

Here the dopant activation efficiency was determined for carefully prepared films of electronically coupled doped Si NCs. Thin film field effect transistors (FETs) are particularly useful in providing information about the mobility of carriers and the Fermi level of NC films. Comparison with the nominal dopant concentration enables us to derive the dopant activation efficiency in Si NCs in a functional electronic film. We investigate two sizes of Si NCs, large (8-15 nm) and small (4-7 nm).

Si NC suspensions ("inks") are produced by the addition of solvent (1,2-dichlorobenzene, DCB) to freestanding boron and phosphorus-doped Si NCs produced using a nonthermal plasma process, which was described in Chapters 1-3, followed by ultrasonication. The nominal concentration of dopants is defined as $N_{a,nom} = n_{Si} \times [PH_3]/([SiH_4] + [PH_3])$ or $N_{a,nom} = n_{Si} \times 2[B_2H_6]/([SiH_4] + 2[B_2H_6])$, where $[PH_3]$, $[SiH_4]$, and $[B_2H_6]$ are the precursor flow rates of phosphine, silane, and diborane, respectively and n_{Si} is the atomic density of silicon ($5 \times 10^{22} cm^{-3}$). The Si NC suspensions used in this study appear cloudy but stable over long periods of time (days to months). Figure 4.1a shows a photograph of a Si NC suspension in DCB and an overview of the steps for Si NC

thin film FET fabrication.

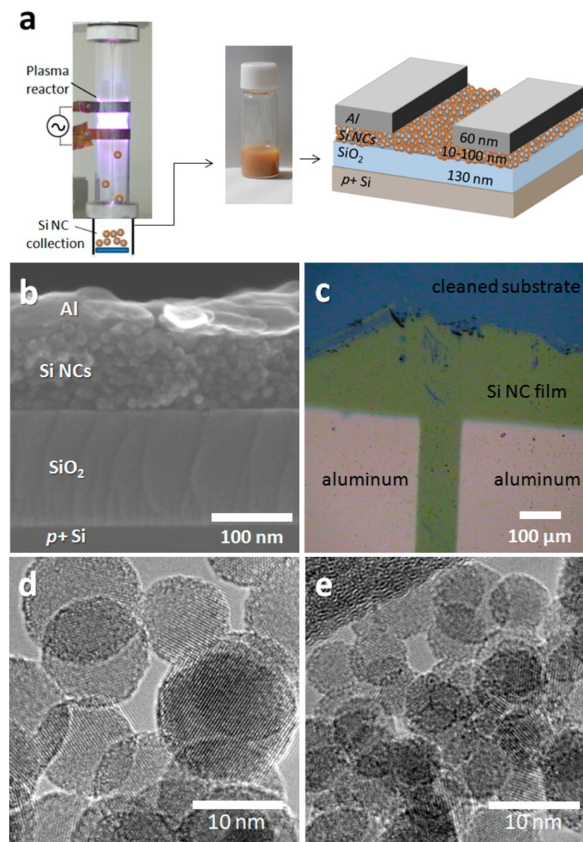

Figure 4.1: **FET fabrication.** **(a)** Si NC fabrication process with photographs of a plasma reactor and a suspension of Si NCs in DCB and device structure. **(b)** SEM cross-sectional image of device showing layers, from bottom to top of p+ silicon gate, 130 nm oxide, ∼100 nm Si NC layer, and 60 nm aluminum. **(c)** Photograph of Si NC FET with NC layer partially removed to expose blue oxide, the golden color corresponds to the Si NC thin films (∼30 nm), and gray to the aluminum source and drain top contacts. TEM images of **(d)** large (8-15 nm) and **(e)** small (4-7 nm) Si NCs.

FETs were fabricated by successive spin-coating (1000 rpm) of Si NC dispersions onto cleaned doped (p+) silicon wafers with a 130 nm thermal oxide as the gate dielectric. While the thickness of the Si NC thin film scaled roughly linearly with the number of coatings, there was a significant batch-to-batch difference in the number of coatings required for similar thicknesses. The thickness of the thin film could be rationally estimated by its reflected color due to thin-film interference; a dark gold reflected color

was used in this study, which corresponded to a thickness of about 10-40 nm, unless otherwise noted. Top aluminum contacts (60 nm) were thermally evaporated with a shadow mask with a width (W) of 2000 μm and a channel length (L) of 20 μm, unless otherwise noted.

Si NC thin films fabricated by successive spin-coating are observed to be closely packed and form a continuous film over the entire substrate without cracks. Figure 4.1b shows a cross-sectional SEM image of a Si NC thin films FET fabricated from large NCs, with diameters of 8-15 nm. The Si NC thin films typically have about 2-5 monolayers of thickness variation, with a few large (order of 100s of nm) agglomerates. Figure 4.1c shows an optical image of a device with the Si NC layer partially removed to show the difference in color between the gate oxide (blue) and Si NC film (golden). The golden color of the thin films corresponds to a thickness of $\sim$10-40 nm and transitions to different colors with increasing thickness, for example, pink at $\sim$40-80 nm and green-blue at $\sim$80-120 nm, due to thin films interference effects. Typical transmission electron microscope (TEM) images of the large (8-15 nm) and small (4-7 nm) Si NCs are shown in Figure 4.1d,e. As previously described, Si NCs synthesized with a nonthermal plasma can be highly crystalline by properly selecting plasma parameters.

4.3 Doped Si NC FET Characteristics

Figure 4.2 shows typical drain-current (I_D)-gate-voltage (V_{GS}) characteristics for intrinsic and doped Si NC thin films made with large and small NCs. For devices made with nominally low (less than $\sim$1%) dopant concentrations, n-type behavior is observed. For films fabricated from nominally high phosphorus and boron concentrations ($\sim$10%), FETs show minimal to no gating behavior as would be expected for degenerately doped Si, where the heavily doped Si NCs approach the metallic regime. The trace for nominally 10% boron large Si NCs shows a slight decrease in I_D with increasing V_{GS} while the trace for nominally 10% phosphorus large Si NCs shows nearly constant current. Importantly, the threshold voltage (V_T), where the device "turns on" is observed to be strongly dependent on the doping type and concentration. This is clearly shown in Figure 4.2b where the traces have been normalized for variations in the mobility.

Figure 4.2 also shows the difference between fast (10 Vs^{-1}) and slow (1 Vs^{-1})

sweep rates of the gate-voltage (V_{GS}). For slow sweep rates, a significant hysteresis is observed along with lower "off" currents; while for fast sweep rates the hysteresis is significantly reduced but off currents can be significant. The observed hysteresis is attributed to screening of carriers caused by traps, likely at the gate-oxide/NC interface or NC surface,[100,101] and the creation or removal of defects related to silicon-hydride species.[102,103] For nominally low doped Si NCs the on/off ratio varied between 10^1 and 10^4 where the off current was also dependent on NC film thickness and aforementioned sweep rate of V_{GS}.

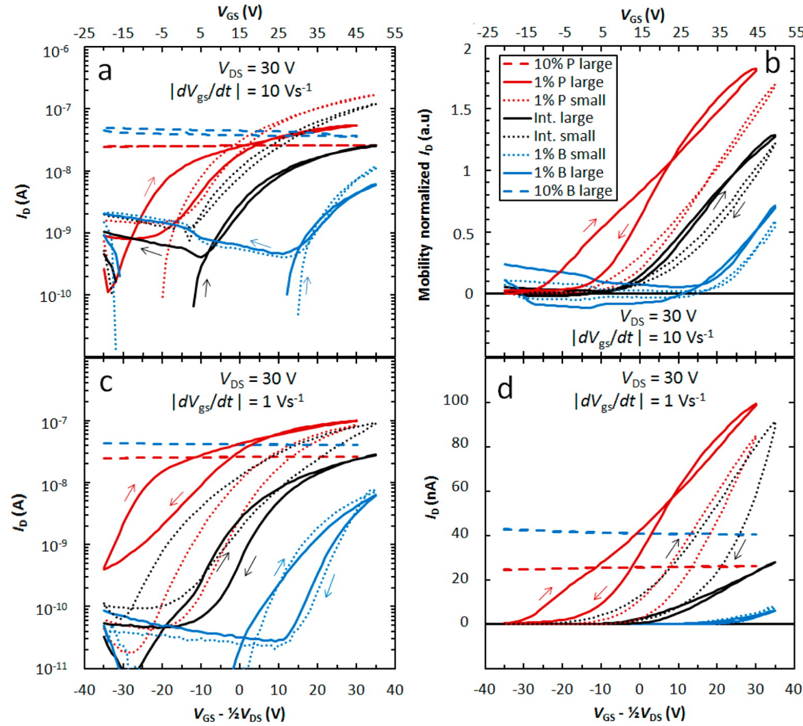

Figure 4.2: **FET characterization.** Drain-current (I_D)-gate-voltage (V_{GS}) characteristics of doped Si NC thin films FETs **(a)** measured using a fast sweep rate of $10Vs^{-1}$ for (red) P- and (blue) B-doped (dashed) 10% 8-15 nm, (solid) 1% 8-15 nm, (dot) 1% 4-7 nm, (black solid) intrinsic 8-15 nm, and (black dot) intrinsic 4-7 nm Si NCs, **(b)** mobility-normalized I_D-V_{GS} characteristics plotted on a linear scale, and the same devices measured with a slower sweep rate of 1 Vs^{-1} on **(c)** a semi-log scale and **(d)** a non-normalized linear scale. All devices shown have width/length (W/L) of 2000/20 μm and are measured with a drain-source voltage (V_{DS}) of 30 V.

From the I_D-V_{GS} traces the threshold voltage (V_T) and the linear mobility (μ_{lin})

can be determined as the x-intercept and slope of the linear region, respectively, based on the gradual channel approximation:[104]

$$I_D = (W/L)C_{ox}\mu_{lin}\left[V_{GS} - \left(\frac{1}{2}V_{DS} + V_T\right)\right]V_{DS} \tag{4.1}$$

where C_{ox} is the specific capacitance of the gate oxide, and V_{DS} is the applied voltage of the drain electrode with respect to source electrode, and W and L are the channel width and length, respectively. V_T can provide valuable insight into the properties of the Si NC thin films, specifically with respect to the Fermi-level. The dependence of V_T on doping type and concentration was confirmed from the output characteristics and typical output characteristics are shown in Figure 4.3 for large Si NCs. The expected saturation above the saturation voltage (V_{SAT} = V_{GS} - V_T) is evident for low nominally doped Si NCs and is marked by diamonds, where V_T was determined from the I_D-V_{GS} traces. For 10% phosphorus and boron-doped Si NCs there is no gating behavior which further confirms the degenerate doping.

In Figure 4.4a V_T is plotted as a function of nominal dopant concentration. V_T is shown to be strongly dependent on the nominal doping type and concentration. Increasing the nominal doping concentration of boron leads to higher positive V_T and, conversely, higher concentrations of phosphorus leads to more negative V_T. The expected V_T for a FET can be calculated with the gradual channel approximation assuming bulk-like properties of the Si NC layer. In Figure 4.4a the calculated V_T are shown for various dopant activation efficiency η as a function of nominal doping concentration ($N_{a,nom}$) where the dopant activation efficiency η is defined as $N_{a,act} = \eta N_{a,nom}$, with $N_{a,act}$ the actual extrinsic carrier density. A comparison between the experimental results and V_T predicted by the model reveals that boron behaves as a p-type dopant that lowers the Fermi-level, requiring higher positive gate voltages to accumulate charges in the channel, and phosphorus behaves as an n-type dopant that raises the Fermi-level, as shown in the inset of Figure 4.4a. The efficiencies of dopant activation ($\sim 10^{-2}$-10^{-4}) are similar to EPR measurements of phosphorus doped Si NCs synthesized using a different gas-phase synthesis method.[105] As Si NCs in that study were covered in a native oxide and defects at that Si/SiO_x interface may lead to dopant compensation, it is not obvious why the dopant activation efficiency is similar to our study that is based on

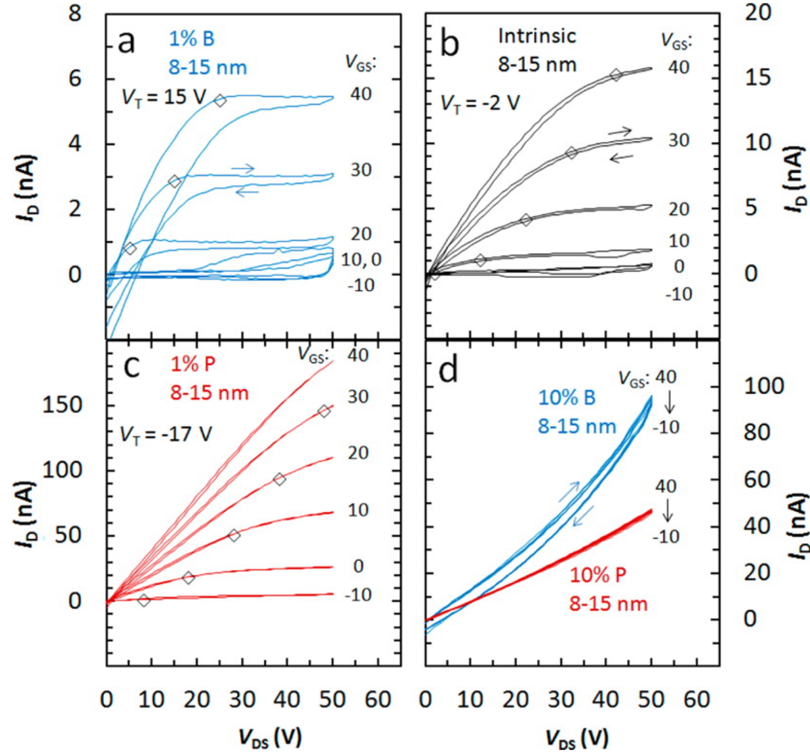

Figure 4.3: **Doping dependence.** Output characteristics of Si NCs thin films transistors with nominally **(a)** 1% B-doped, **(b)** intrinsic, **(c)** 1% P-doped, and **(d)** 10% (blue) B- and (red) P-doped; diamonds are where $V_{DS} = V_{SAT} = V_{GS}$ - V_T, indicating where the expected transition to saturation behavior, with V_T specified in each panel.

largely oxide-free Si NCs.

4.4 Size-dependence

In large NCs V_T changes over a large range as doping behavior shifts gradually between semiconducting and metallic-like, while for small phosphorus doped NCs a sharp transition is observed from low off-currents (<1 nA) to high off-currents (10's of nA). This is evident in both the I_D-V_{GS} and output characteristics as shown in Figure 4.5. We attribute this behavior to the expected semi-discrete wavefunctions of Si NCs in films and the expected distribution of number of dopants in individual NCs. This distribution of dopants is expected to result in ensembles of NCs made of NCs that are either doped or

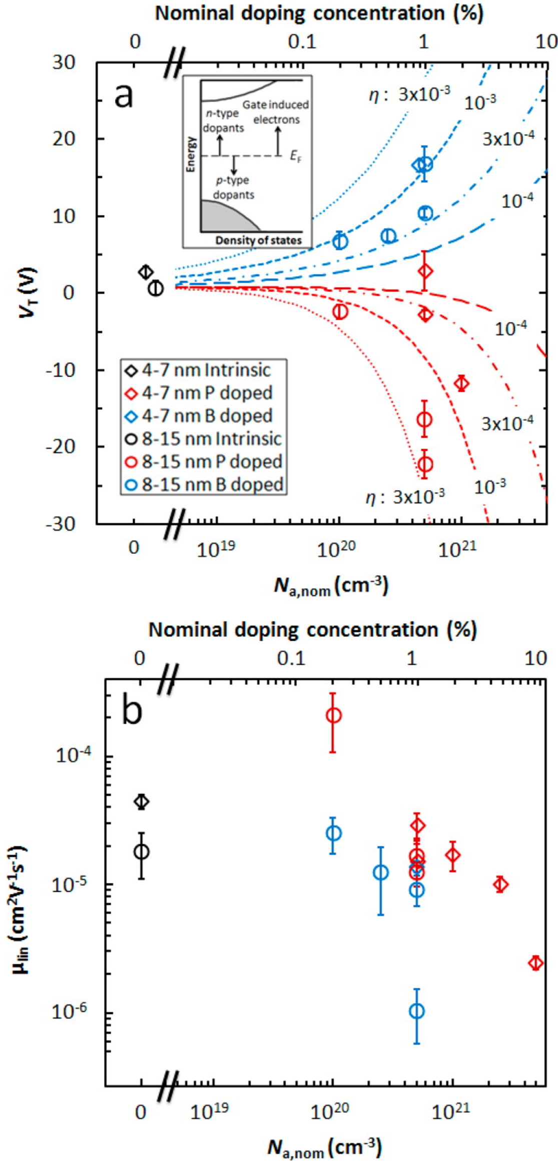

Figure 4.4: **Threshold voltage. (a)** Threshold voltage (V_T) summary as a function of nominal doping concentration and **(b)** μ_{lin} dependence on nominal doping concentration for (red) P, (black) intrinsic, and (blue) B Si NC thin films for (diamond) small 4-7 nm, and (circle) large 8-15 nm Si NC thin films. Error bars are the standard deviation of 5-8 devices fabricated from the same batch of NCs with at least 2 different substrates where each point represents a different batch of NCs, some points are slightly offset for clarity. Lines in (a) are calculated V_T for various active dopant activation efficiencies. Inset: Density of states diagram and the effect of dopants and gate-induced electrons on the Fermi level, E_F.

intrinsic. This issue becomes especially evident for small NCs, where a small NC would be either intrinsic or degeneratively doped by a single active dopant. For example in a 4 nm Si NC, one active phosphorus dopant would result in a degenerative doping concentration of $3.13 \times 10^{19} cm^{-3}$, while for a large (12 nm) NC with one active phosphorus dopant, the doping concentration of $1.11 \times 10^{18} cm^{-3}$ would be nearly degenerate and result in V_T of -21 V in our device structure (assuming bulk-like properties). This binary nature of doping in small NCs leads to the observed increased off-currents due to conduction paths consisting of degenerate NCs along with additional gate-induced pathways of intrinsic NCs.

We assume the probability ρ_n of a single NC having n number of dopants follows Poisson statistics:

$$\rho_n = N_d^n/n!\, exp(-N_d) \tag{4.2}$$

where N_d is the average number of active dopants per NC ($N_d = \eta N_{d,nom}(4/3\pi r^3 n_{si})$), η is taken from Figure 4a, and r is the average radius of the NC. For a small NC where one or more dopants result in a degenerate NC, the fractional concentration of degenerate NCs is given by x = (1 - p_0).

According to percolation theory for a film made of a fraction of conducting (x) and insulating $(1 - x)$ spheres, there is a percolation transition near a threshold x_c and the film is insulating below this value, typically about 0.27.[106,107] Above this threshold the conductivity scales as $\sigma \propto (x - x_c)^t$, where t is in the range ~1.1-1.8, depending on a variety of factors including geometry, size dispersion, and packing of the film.[107] In Figure 4.5b the normalized scaling of conductivity $(x - x_c)^t/(1 - x_c)^t$ is compared to the off-current as a function of nominal doping concentration, where we assume a t of 1.73 and an r of 5 nm. The close agreement in trends between percolation theory and the experimental results supports the previous assumption that small NCs are either intrinsic or degenerate.

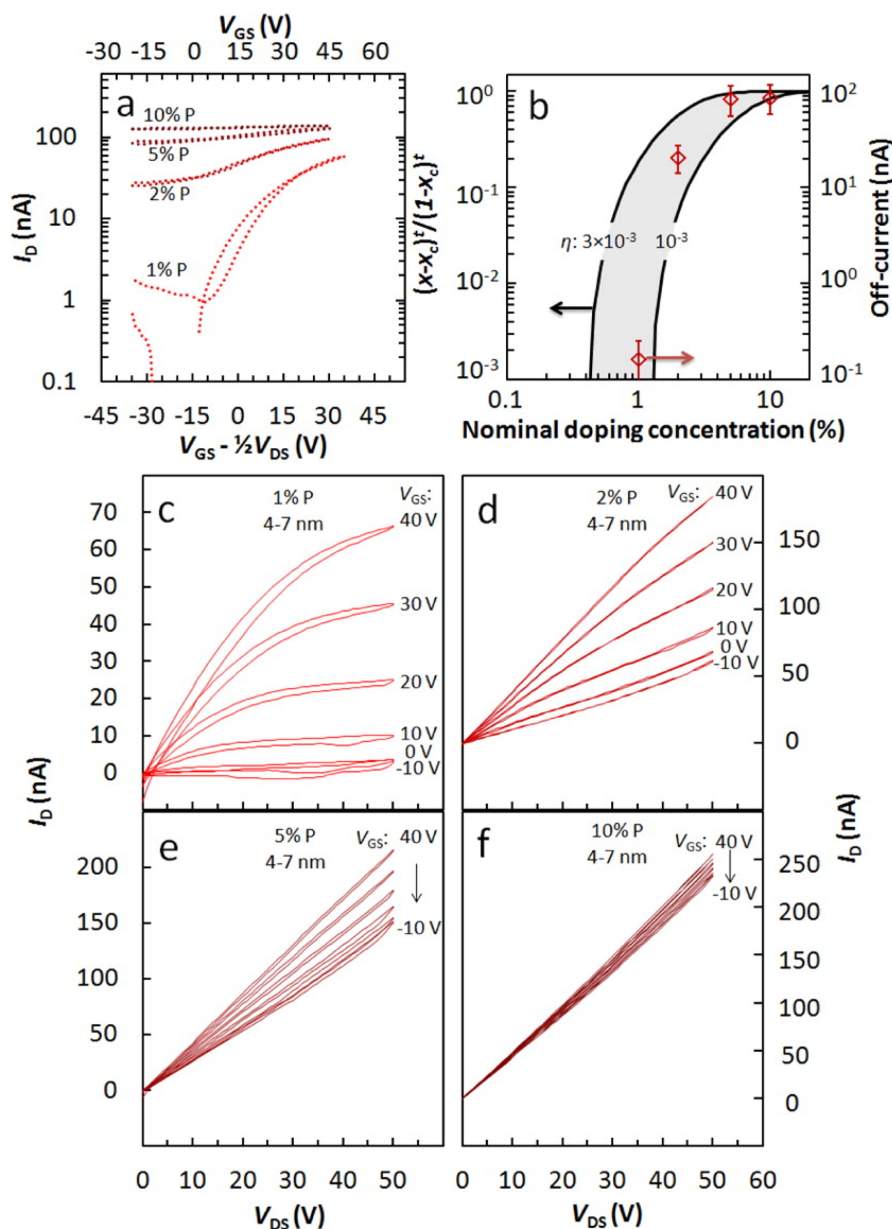

Figure 4.5: **FET characteristics of small Si NCs.** Characteristics of Si NC FETs fabricated with small (4-7 nm) Si NCs showing sudden change from intrinsic to metallic behavior. **(a)** I_D-V_{GS} characteristics on a semi-log scale, and **(b)** normalized scaling of conductivity according to percolation theory compared with the (steady-state) off-currents of 4-7 nm P-doped as a function of nominal doping concentration and output characteristics with nominally **(c)** 1% P-doped, **(d)** 2% P-doped, **(e)** 5% P-doped, and **(f)** 10% P-doped.

4.5 Mobility

A wide range of electron mobilities for the Si NC films, from $<10^{-6}$ to 5×10^{-4} $cm^2V^{-1}s^{-1}$ was found, with a summary of the size and dopant concentration dependence shown in Figure 4.4b. A general trend of decreasing mobility with increasing dopant concentration is apparent. This is likely responsible for the decrease in current observed for high nominally doped NCs compared to the on-current of less doped NCs (as shown in Figure 4.2). Films of small NCs along with phosphorus doped NCs tended to have the higher mobilities, however there was significant variation between batches of NC made with identical synthesis conditions. Theoretical results predict a wide range of factors that influence the mobility in Si NC films including oxide thickness between NCs, NC size and size distribution, and disorder in the packing structure.[108,109] Rigorous efforts were made to avoid oxidation in the samples examined in this study, and only minimal oxidation is evident as seen in typical FTIR spectra. We can therefore exclude the influence of a large amount of oxide between NCs. However a small amount of oxide may act as scattering centers which reduces the mobility. Further investigation is necessary to elucidate the mobility-limiting mechanism.

4.6 Conclusion

In summary, the threshold voltage of Si NC FETs was found to be strongly dependent on dopant concentration and type, consistent with changes in the Fermi-level of Si NC thin films caused by dopant activation with an efficiency of 10^{-3} - 10^{-4} of the nominal precursor concentration. Large NCs exhibited a continuum between intrinsic and degenerate doping, while small NCs show a sharp transition to degenerate doping, suggesting that the wave functions of NCs are still discrete. These results reveal that intentional inclusions of impurities in the core of Si NCs such as phosphorus and boron can effectively dope of Si NC resulting in control of the Fermi-level and carrier concentration which is desirable for the development of functional Si NC based devices.

4.7 Future work

Now that we have established a better understanding of doping in nanocrystals, the next step is to improve device performance. In a collaboration with Ting Chen the transport properties and mechanism for doped nanocrystal films are being investigated. A tremendous improvement in conductivity is observed when dopants are incorporated into the nanocrystals, agreeing with the FET results in this work. However, there are two main improvements that can be made to these systems.

First the size distribution of the silicon nanocrystals remains relatively large. Size-selection can be applied to narrow this size distribution, and this would offer the possibility of forming 2D super lattices and band-like transport. An increase in performance is expected for more uniform thin films. In addition, it would also further verify the size effects that were observed in this study.

A second area for improvement is the removal of the amorphous shell that is present around the nanocrystals.[110] As a result of the plasma synthesis technique, about 2 monolayers of amorphous silicon is present on the nanocrystals. This amorphous silicon acts as a barrier for electron transport, and therefore it is desired to remove it. In order to do that we first have to obtain a better understanding of the mechanism that leads to the formation of the amorphous layer. It has been suggested to the nanoparticle temperature is too low in the afterglow of the plasma where the nanocrystal are largest. When silane radicals absorb on the nanocrystal there is insufficient energy for crystallization. Possible solutions for the removal of the amorphous layer are the incorporation of an etching step after synthesis, or introducing extra heat during the synthesis to crystallize the thin layer of amorphous silicon.

In this work only purely boron or phosphorous doped Si NCs were studied. It is also possible to introduce both dopants during synthesis and form codoped Si NCs. Preliminary work showed that particles can be tuned from n-type, to ambipolar, to p-type behavior, by changing the ratio of boron to phosphorus. It would be interesting to obtain a better understanding of the dopant mechanism and position for codoped NCs.

Finally we should explore alternative plasma-synthesized materials such as germanium, silicon-germanium alloys and oxides. Not only is the doping of these materials

poorly understood, the transport properties could potentially be significantly better compared to silicon. A comprehensive transistor study would further enhance our understanding of these materials.

4.8 Experimental methods

Nanocrystal synthesis. Si NCs were synthesized in a nonthermal plasma as previously described, where continuous gas flow of silane, argon and phosphine (15% in hydrogen) or diborane (10% in hydrogen) were introduced into a quartz reactor tube with 110W of RF power applied to ring electrodes. The "small" nanocrystals were synthesized using a 12×0.61 mm orifice and an argon flow rate of 55 sccm. For the larger nanocrystals the orifice spacing was reduced to 12×0.5 mm with an argon flow rate of 35 sccm. The nanocrystal size was verified using X-Ray Diffraction and Transmission Electron Microscopy.

Nanocrystal inks. Suspensions of Si NC "inks" were prepared by the addition of anhydrous 1,2-dichlorobenzene (DCB, Sigma Aldrich) to dry Si NC powders with concentrations of about 2 $mg\ ml^{-1}$. Dispersions were formed by using a tip-ultrasonicator (Sonic & Materials, Inc - VCX130PB) at 25% power for 1 minute. The resulting dispersions were cloudy but did not show significant flocculation over the period of several days to months.

FET production. Thin-film field effect transistors were fabricated by successive spin-coating (1000 rpm) of Si NC dispersions onto cleaned doped (p+) silicon wafers with a 130 nm thermal oxide as the gate dielectric. While the thickness of the Si NC thin-film scaled roughly linearly with the number of coatings, there was significant batch-to-batch difference in the number of coatings required for similar thicknesses. The thickness of the thin-film could be rationally estimated by its reflected color due to thin-film interference; a dark gold reflected color was used in this study that corresponded to a thickness of about 10-40 nm, unless otherwise noted. Top aluminum contacts (60 nm) were thermally evaporated with a shadow mask with width (W) of 2000 μm and channel length (L) of 20 μm, unless otherwise noted.

FET measurements. FETs were measured at room temperature with a Keithley Semiconductor Characterization System (Model SCS-4200) in a nitrogen purified glovebox with oxygen and water concentrations of <1 ppm. The synthesis, handling, and measurements of FETs were performed without exposure to air.

ATR-FTIR. ATR-FTIR spectroscopy (JASCO, 6100) was performed under vacuum with a ZnSe ATR crystal. Solutions of Si NCs in DCB were deposited onto the ATR crystal and the analysis chamber was immediately evacuated with a roughing pump under a small flow of nitrogen gas and DCB was completely evaporated prior to acquiring spectra. The samples experienced a brief (<2 minutes) exposure to air and the FTIR analysis was performed after device fabrication and characterization. Air-free FTIR spectroscopy of chlorine terminated NCs was performed in transmission mode air-free cell with thallium bromoiodide (KRS-5) windows with a layer of NCs deposited on one window.

SEM. SEM was performed with a JEOL-6700F and TEM was performed on a FEI Tecnai G2 30 operating at 200 kV.

Acknowledgement

The work of R.G., D.Y., and T.N. was supported by the Funding Program for Next Generation World-Leading Researchers (GR040). R.G. was also partially supported by the Japanese Society for the Promotion of Science, Research Fellowship for Young Scientists (DC1). The work of N.J.K. and U.R.K. was supported by the DOE Plasma Science Center for Predictive Control of Plasma Kinetics. U.R.K. also acknowledges partial support by the Army Office of Research under MURI Grant W911NF-12-1-0407. T.C. is supported primarily by the National Science Foundation through the University of Minnesota MRSEC under Award Number DMR-0819885. Part of this work was carried out in the College of Science and Engineering Characterization Facility, University of Minnesota, which has received capital equipment funding from the NSF through the UMN MRSEC program. We thank K. Iwazumi for assistance with FTIR measurements.

Chapter 5

Plasmonic Properties of Silicon Nanocrystals Doped with Boron and Phosphorus‡

5.1 Introduction

A localized surface plasmon resonance (LSPR) describes the collective oscillation of free charge carriers, which are dielectrically confined in a nanoparticle, in response to an external electromagnetic field. These resonances emerge for degenerately-doped nanocrystals in which the free-carrier concentration is high. Now that we have established a successful route for nanocrystal doping, as was described in the previous chapter, we can use these properties to explore their plasmonic behavior. In this chapter the plasmonic properties of phosphorus-doped and boron-doped silicon nanocrystals are studied. The findings enable improved control of the plasmonic response of silicon nanocrystals in the infrared and provide air-stable plasmonic silicon nanomaterials.

‡Portions of this chapter were submitted to Nano Letters for publication under the authorship of Nicolaas J Kramer, Katelyn S. Schramke and Uwe R. Kortshagen.

Nanocrystals (NCs) that exhibit a localized surface plasmon resonance (LSPR) have attracted attention for a wide range of applications from photothermal therapies,[111] to bioimaging and biosensing,[112,113] plasmonic enhancement of solar cells,[114] nanoelectronics,[115] hot electron generation for photocatalysis and photovoltaics,[116] and electrochromic materials.[117] A variety of materials have been proposed for plasmonic applications spanning a wide range of wavelengths.[118] In recent years degenerately doped semiconductor NCs have attracted significant attention. Contrary to noble metal NCs,[119] in which the carrier density is fixed, the position of the LSPR of doped semiconductor NCs can be tuned by adjusting the free carrier concentration of the NCs.[31]

Several strategies have been applied to control the free carrier concentration and the resulting LSPR of semiconductor NCs. The most common strategies are the extrinsic doping of semiconductors with n-type or p-type dopants,[120–123] the self-doping of compound semiconductors through the tuning of the NC composition,[124,125] and the doping through NC-solvent interactions.[126] Doping of semiconductor NCs allows for control over the LSPR wavelength while the NC size or shape remain unaffected. However, like many nanomaterials, doped semiconductor NCs suffer from oxidation and the strong influence of the NC surface conditions which may negatively impact their plasmonic properties. For instance, metal chalcogenides NCs such as copper sulfide become increasingly doped during oxidation, resulting in an LSPR blue-shift.[127] Also, adsorbed surface species can trap free carriers such as in zinc oxide NCs where the plasmonic response may be completely eliminated through surface hydroxyl groups.[128]

Silicon NCs are potentially interesting nanomaterials for plasmonic applications in the infrared due to silicon's low cost and low toxicity. Recently, localized surface plasmon resonances were observed in highly phosphorus-doped and boron-doped silicon nanocrystals (Si NCs) produced via nonthermal plasma synthesis.[122,123] However, the details of the influence of the NC surface on dopant activation and plasmonic response are still poorly understood. Rowe *et al.* reports tunable LSPRs of phosphorus-doped Si NCs right after the synthesis and kept under air-free conditions.[122] In contrast, Zhou *et al.* do not observe LSPRs of as-produced Si NCs, but report the occurrence of LSPRs only after long-time oxidation.[123] They suggest that long-time oxidation leads to a reduction of surface defect states that can trap free carriers and reduce the plasmonic response. In this paper, we study the evolution of the LSPRs of phosphorous-doped

and boron-doped Si NCs during oxidation and after post-synthesis annealing. Based on our results, we suggest that the plasmonic response of silicon NCs is determined by oxidation-induced generation or removal of free carriers. We interpret these results in the view of surface doping and trap generation. The oxidation-induced changes in free carrier concentration can be reversed upon removal of the surface oxide through etching. Low temperature annealing leads to an overall increased activation of free carriers. Our results provide a better understanding of the effect of surface conditions and oxidation on the plasmonic response of Si NCs and suggest viable routes to achieve air-stable plasmonic Si NCs with controlled LSPRs in the infrared range of the spectrum.

5.2 Results and Discussion

Freestanding boron and phosphorus-doped Si NCs, with an average size of 8 nm, are produced using a nonthermal plasma process which has been described previously.[98,99,122] The indicated fractional dopant flow rates are defined as $X_P = [PH_3]/([SiH_4]+[PH_3]) \times 100\%$ and $X_B = 2[B_2H_6]/([SiH_4]+2[B_2H_6]) \times 100\%$, where $[PH_3]$, $[SiH_4]$ and $[B_2H_6]$ are the gaseous precursor flow rates of phosphine, silane and diborane, respectively. The Si NCs are deposited directly onto a glass substrate, silicon wafer or an aluminum-coated silicon wafer for further analysis. Fourier Transform Infrared Spectroscopy (FTIR) measurements of as-produced NCs are performed in a nitrogen-purged glovebox environment.

Figures 5.1a and 5.1b show the FTIR spectra of as-produced phosphorus-doped and boron-doped Si NCs with increasing fractional dopant flow rates. These results illustrate a significant difference in plasmonic behavior between the two doping cases. For sufficiently high doping concentrations, a plasmon resonance emerges for phosphorus-doped Si NCs. The plasmon peak position blue shifts for increasing fractional dopant flow rates as a result of the increased doping concentration. Using the peak position of the plasmon resonance,[31] we find a free carrier concentration of 1.9×10^{20} cm^{-3} for a fractional dopant flow rate of 30%. Assuming a nanoparticle size of 8 nm we estimate that highly phosphorus-doped Si NCs contain approximately 100 active phosphorus dopants per NC. In addition, there is a phosphorus-hydride stretch visible at 2276 cm^{-1} that becomes more pronounced for higher doping concentrations. This suggests that the

surface of the NC also contains a significant amount of phosphorus which is likely inactive.[129] The as-produced NCs do not show any sign of oxidation as is confirmed by the absence of silicon oxide features in the spectra.

In contrast to phosphorus-doped Si NCs, the as-produced boron-doped Si NCs show no plasmon resonance, even at high fractional dopant flow rates. The boron-hydride, amorphous boron and boron-oxide stretches at 2500 cm^{-1}, 1800 cm^{-1} and 1400 cm^{-1} respectively indicate that boron is placed on the surface of the Si NC during synthesis. The lack of a plasmon resonance must be a result of the significantly smaller free carrier density compared to phosphorus-doped Si NCs. This difference in phosphorus and boron incorporation efficiency has been shown by various computational models,[130–132] in which the lower active boron concentration in Si NCs was attributed to the larger formation energy of boron compared to phosphorus in Si NCs. As a result, the boron atoms prefer to reside on or near the surface of the Si NC where it does not affect the free carrier concentration.[133]

To investigate the role of the surface properties on the plasmonic properties we perform post-synthesis oxidation and annealing treatments. Figure 5.1c shows the effect of oxidation on phosphorus-doped and boron-doped Si NCs as a function of oxidation time. Opposite behavior is again observed during oxidation. For the case of phosphorus-doped Si NCs, the LSPR vanishes as the NCs oxidize. A strong Si-O-Si bridging feature appears at 1050 cm^{-1} and a back-bonded oxide at 2300 cm^{-1}. This suggests that oxidation of phosphorus-doped NCs reduces the number of free carriers, as the LSPR disappears after four hours of air exposure.

When boron-doped Si NCs are exposed to oxygen, a LSPR emerges and blue shifts as the particles oxidize. Therefore this suggests that during oxidation additional free carriers are generated. As a result, this allows for the production of air-stable plasmonic Si NCs, which is an important step for the use of these plasmonic NCs in applications. The mechanism of free carrier generation or removal and the role of the surface will be investigated in the remainder of this chapter.

The effect of oxide removal was studied to better understand the role of the oxide. Once the doped Si NCs are fully oxidized, the oxide shell is removed using hydrofluoric acid (HF) vapor followed by measurement of the FTIR spectra of oxide-free Si NCs. The FTIR spectra of the etched Si NCs are shown in Figure 5.1d. For phosphorus-doped

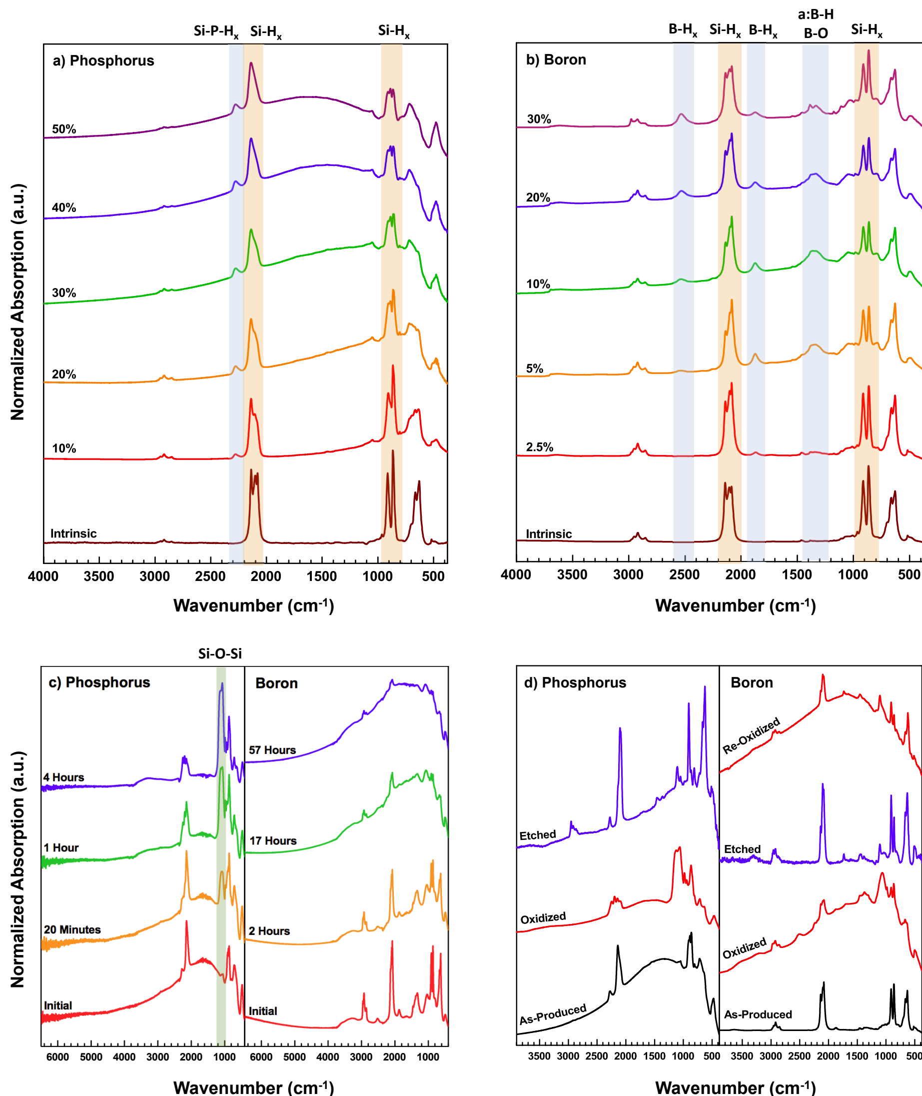

Figure 5.1: **Plasmonics of phosphorus-doped and boron-doped Si NCs.** FTIR spectra of as-produced **(a)** phosphorus-doped and **(b)** boron-doped silicon nanocrystals with increasing fractional doping flow rates. For phosphorus-doped Si NCs a LSPR emerges for sufficiently high doping concentrations. A LSPR is not visible for boron-doped Si NCs, even at high doping levels. Dopant surface atoms as well as silicon hydride peaks are observed, as indicated by the blue and orange regions. Spectra are offset for clarity. **(c)** Oxidation of phosphorus-doped and boron-doped Si NCs in air as a function of time. Opposite behavior is observed, with the LSPR disappearing for phosphorus-doped Si NCs while a LSPR develops and blue-shifts during oxidation for boron-doped Si NCs. **(d)** Development of the LSPR for as-produced and subsequent oxidized and etched phosphorus-doped and boron-doped Si NCs.

Si NCs, the plasmon resonance returns after removal of the oxide but is red-shifted with respect to its original position. This implies that phosphorus dopants are removed during etching, which is also confirmed by EDX measurements (see Figure 5.2). The complete removal of the oxide is confirmed by the lack of the two silicon oxide peaks in the FTIR spectrum. Similar behavior was observed by Zhou *et al.*, where a strong plasmonic resonance appeared after removal of the oxide.[123]

For boron-doped Si NCs the plasmon resonance disappears after etching and the new spectrum resembles the spectrum of as-produced NCs. When the boron-doped Si NCs reoxidize, the plasmon resonance returns, confirming the need of an oxide shell for a plasmon resonance to develop. The peak position of the plasmon is not significantly affected by the etching and oxidation step, indicating that the free carrier density remains constant.

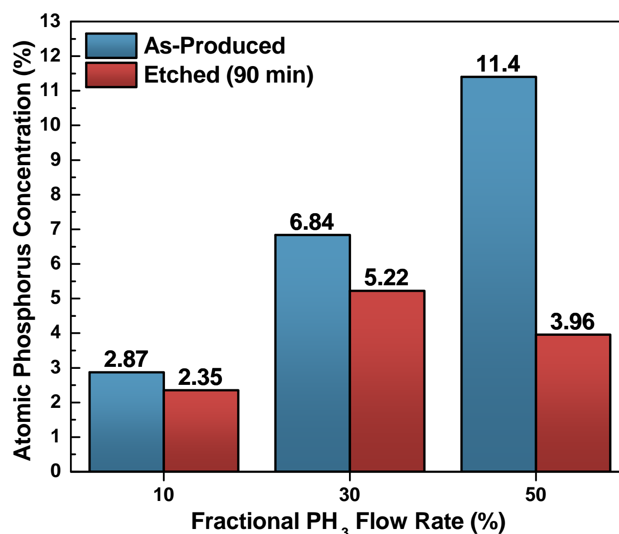

Figure 5.2: **EDX on P-doped Si NCs.** Atomic phosphorus concentration in Si NCs obtained from Energy-Dispersive X-Ray spectroscopy (EDX) measurements. An increase in phosphine (PH_3) flow rate directly leads to a larger fraction of phosphorus within the NCs. After HF vapor etching the phosphorus concentration decreases, indicating that oxidation and subsequent etching leads to a removal of phosphorus from the NCs.

Previously it has been suggested that a silicon oxide shell is required for plasmonic behavior, as it would provide a passivation route that reduces surface defect states.[123] Our findings contradict this theory, since plasmonic behavior is only observed for oxidized boron-doped Si NCs. On the other hand, for phosphorus-doped Si NCs, the plasmonic properties deteriorate during oxidation. This suggests that the plasmonic response of silicon NCs is determined by oxidation-induced generation or removal of free carriers on the surface of the nanocrystal.

Doping is traditionally achieved by substitutional placement of impurities into the core of the material. However, it has been demonstrated that doping can also be achieved via electron exchange between a semiconductor and surface dopants.[134,135] If the lowest unoccupied molecular orbital of the surface dopant is close to the valance band maximum of the semiconductor, it will acquire an electron from the semiconductor. As a result, additional free carriers will be generated near the surface of the semiconductor. Similar behavior is observed for the case of boron-doped Si NCs, where the dopants reside on the surface and free carriers are generated after oxidation, suggesting that surface doping is responsible for the generation of free carriers.

In addition to the change in plasmonic behavior, we also observe the effect of doping on the oxidation rate of the Si NCs. The Cabrera-Mott oxidation mechanism of the Si NCs is considered for a better understanding of the effect of dopants on oxidation. This theory describes ionic diffusion of oxygen through the oxide shell driven by a self-generated electric field across the oxide film. This electric field results from electron tunneling between the Fermi level of the silicon core and the acceptor levels of chemisorbed oxygen at the oxide surface. Phosphorus-doped Si NCs have a significantly enhanced oxidation rate compared to intrinsic Si NCs while boron doping strongly reduces the oxide growth rate, as shown in Figure 1c. This effect can be explained by considering the enhancement or suppression of the electric field by adding or removing free carriers, as described by the Cabrera-Mott oxidation model.[136] Additional free carriers from activated phosphorus atoms raise the Fermi level leading to an increased electric field strength, resulting in increased oxidation rates, whereas boron doping decreases the electric field strength. The reduction in oxidation speed therefore confirms that additional holes are successfully introduced in boron-doped Si NCs.

Electron Paramagnetic Resonance (EPR) measurements were performed to gain

insight into the number and type of defects at the surface of both types of doped Si NCs. These measurements further verify the oxidation-induced generation and removal of free carriers. Figure 5.3 shows the EPR spectra of intrinsic, boron-doped and phosphorus-doped Si NCs. As-produced and oxidized spectra are shown in red and blue respectively. Two types of defects are visible for intrinsic Si NCs. A g-value of 2.0055 is assigned to threefold-coordinated Si in a randomly distorted environment (D centers).[137] After oxidation the line shape and g-value change as a result of the formation of an oxide shell around the nanocrystals (P_b centers), which leads to trivalent silicon atoms at the interface of the silicon core and the oxide.[138]

As-produced phosphorus-doped Si NCs exhibit a broad absorption with a g-value of 1.998. This is attributed to conduction electrons from active dopant atoms.[139–143] After oxidation the magnitude of the broad feature reduces significantly and a traditional oxide signal appears, similar to oxidized un-doped NCs. This confirms that oxidation is reducing the number of conduction electrons and generates trap states while a silicon oxide shell is formed, which is consistent with FTIR results, where the plasmonic response is lost during oxidation.

For the boron-doped Si NCs very little signal is observed. The high concentration of boron atoms on the surface of the Si NC has been shown to lead to a passivation of the surface.[144] In contrast to phosphorus-doped Si NCs, oxidation of the boron-doped Si NCs does not give rise to any further change of the spectrum. The lack of signal from P_b-centers, even after two weeks of oxygen exposure, implies that the boron-doped Si NCs do not form a traditional silicon oxide shell. Alternatively, there could be a thin boron oxide shell on the surface that provides free carriers.

Using X-ray Photoelectron Spectroscopy (XPS) we further analyze the NC surface and dopant activation. Figure 5.4 shows the XPS spectra of phosphorus-doped and boron-doped NCs in as-produced and oxidized states. The phosphorus-doped Si NCs spectrum contains two features. The peak located at $\sim$135 eV results from phosphorus bonded to oxygen. This peak is present for as-produced particles and is likely caused by the short air exposure during sample loading. A second peak at a lower binding energy of $\sim$130 eV is a result of phosphorus bonded to phosphorus or silicon.[145] After oxidation the low energy peak decreases in intensity compared to the higher energy oxide peak. This shows that a large fraction of phosphorus atoms, previously bonded to phosphorus

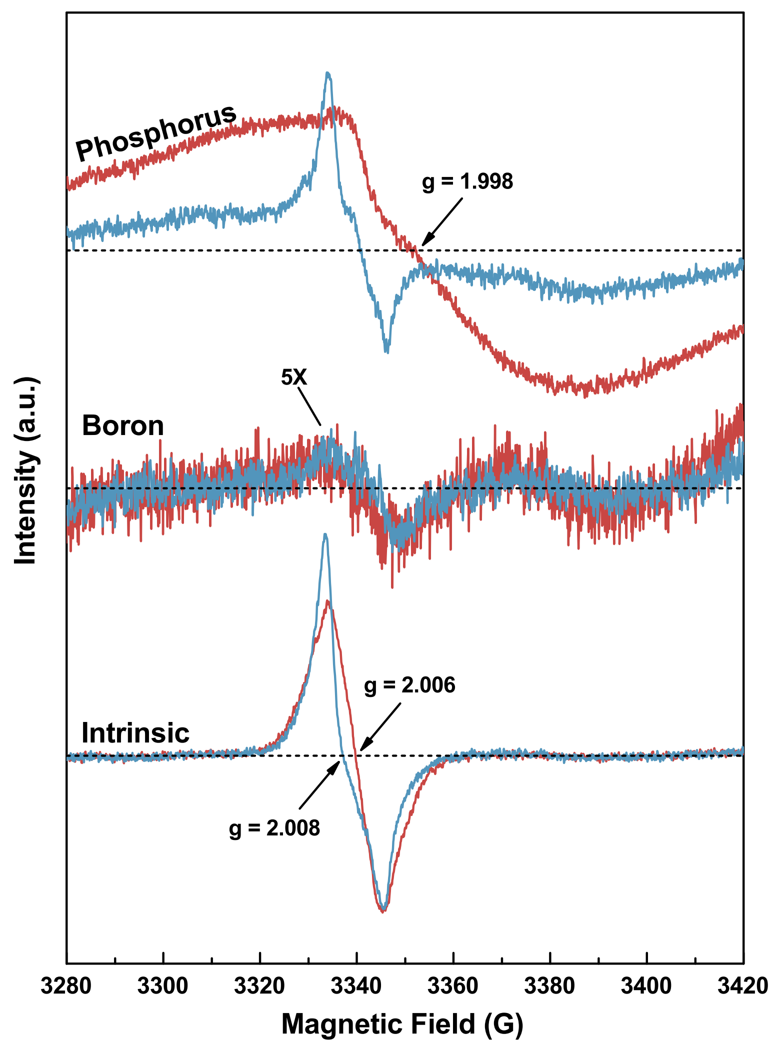

Figure 5.3: **Electron Paramagnetic Resonance spectra for phosphorus-doped, boron-doped and intrinsic Si NCs.** Spectra are shown for as-deposited (red) and oxidized (blue) Si NCs. The spectrum for boron-doped NCs has been magnified by a factor of 5 for clarity.

or silicon atoms, are now bonded to oxygen atoms. The phosphorus-oxide is likely to be inactive and susceptible to removal with the oxide during etching, agreeing with the FTIR and EDX results.

The boron XPS spectrum can be deconvolved into four peaks.[146–148] A broad peak at a low binding energy of ∼185 eV is the contribution from the trivalent state of boron (B(III)). The feature at ∼189 eV results from boron atoms bonded to four silicon or boron atoms. The two higher energy peaks originate from boron atoms that are attached to an electronegative atom such as oxygen.

The XPS spectra in Figure 5.4 indicate that a large fraction of trivalent boron is present on the surface of the NC. Based on peak analysis, the fraction of trivalent boron of as-produced Si NCs is approximately 75%. After oxidation this fraction does not decrease significantly. The spectrum of oxidized Si NCs shows a slight increase in intensity for the peaks corresponding to boron bonded to oxygen. This is contrary to phosphorus, which shows a significant increase in oxygen bonding after oxidation. Similar results were observed in EPR, suggesting that a thin boron-oxide film is forming around the nanocrystal core. It is expected that this boron-oxide layer is responsible for introducing free carriers and leading to plasmonic effects, as was described previously with the surface doping mechanism.

Now that the role of the oxide shell is understood we explore the effect of surface modification through post-synthesis annealing. Low temperature annealing of Si NCs has proven to be capable of reducing the defect concentration by an order of magnitude.[137] Therefore it is expected that plasmonic properties of Si NCs are enhanced by annealing as well. The effect of low-temperature annealing in a nitrogen environment is shown in Figure 5.5a. Here the FTIR spectra of phosphorus-doped and boron-doped Si NCs are plotted as a function of the annealing temperature. The Si NCs were annealed on a hotplate in an oxygen-free glovebox environment for 10 minutes at each specified temperature. During annealing we observe a LSPR for both phosphorus-doped and boron-doped Si NCs, as well as a blue shift of the LSPR peak position for increasing temperatures. The blue-shift of the LSPR during annealing of the phosphorus-doped Si NCs corresponds to an increase in free carrier density from $3.45 \times 10^{20}\ cm^{-3}$ to $1.16 \times 10^{21}\ cm^{-3}$. An annealing treatment is thus able to generate additional free carriers for both phosphorus-doped and boron-doped Si NCs. This is very likely a result

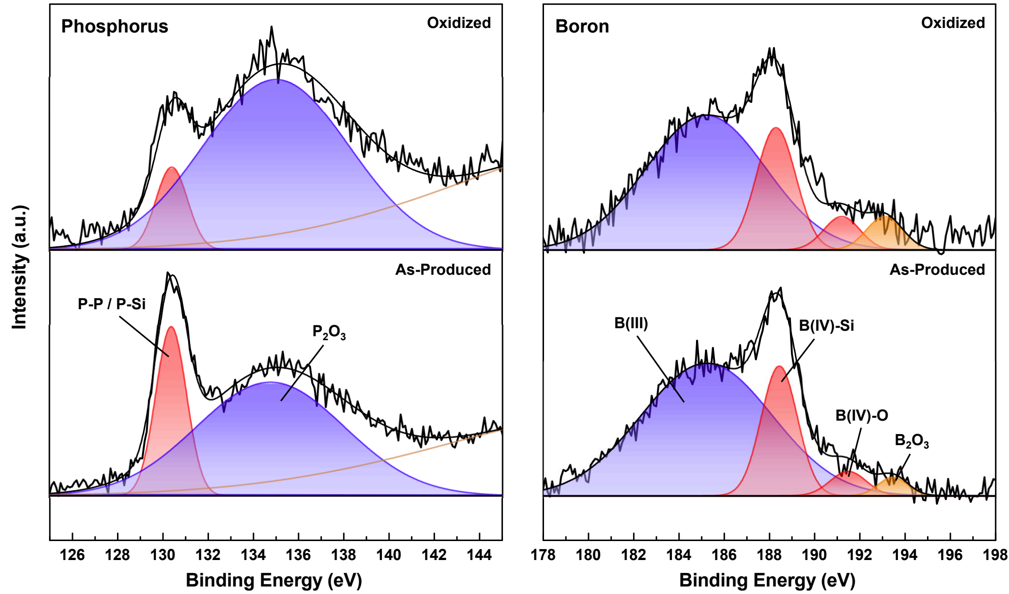

Figure 5.4: **XPS measurements.** X-ray Photoelectron Spectroscopy (XPS) spectra for as-produced and oxidized phosphorus-doped and boron-doped silicon NCs. The phosphorus spectrum can be deconvolved into two peaks. The peak at 130 eV corresponds to phosphorus bonded to phosphorus or silicon (red), while the broad peak at 135 eV is a result of oxidized phosphorus (blue). For boron a broad peak at 185 eV originates from trivalent boron (blue) while the higher energy peak at 188 eV corresponds to tetravalent boron (red). The two peaks at 191 eV (red) and 193 eV (orange) are a result of oxygen bonding to boron.

of the decrease in surface defects, as confirmed by EPR measurements (see Figure 5.6).

The effect of an annealing treatment on oxidized NCs was analyzed and is shown in Figure 5.5b. Interestingly, the LSPR of oxidized phosphorus-doped NCs returns during the annealing treatment, while oxidized boron-doped Si NCs show a slight blue-shift. Similar to as-produced Si NCs, annealing is also able to generate additional free carriers in oxidized Si NCs. While the exact mechanism is unclear at this point, a decrease in defects is likely also responsible for this behavior.

We further investigate the behavior of annealed particles with an oxide shell using FTIR (Figure 5.5c) and EPR (Figure 5.5d). In Figure 5.5c we expose annealed

phosphorus-doped Si NCs to air for subsequent re-oxidation. After 1 day a plasmon resonance is still visible, albeit reduced in size. The spectra stabilize after 3 days of oxidation. The EPR measurements in Figure 5.5d confirm this behavior. After annealing of the oxidized Si NCs a broad signal reappears with a g-value identical to as-produced Si NCs. Once the particles re-oxidize for 1 day the broad signal reduces significantly in size and an oxide feature returns, agreeing with the behavior observed in Figure 5.5c.

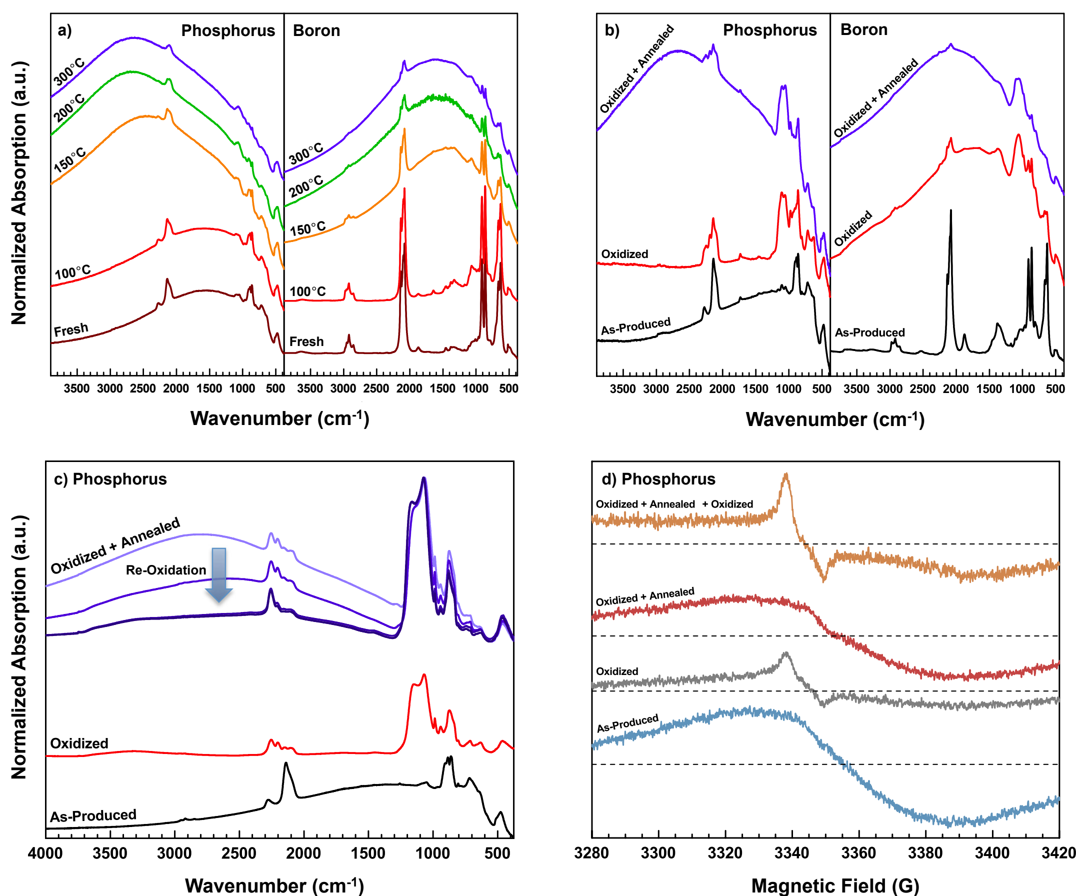

Figure 5.5: **Effect of oxides on plasmonics.** **(a)** Development of the plasmon resonance during low-temperature air-free annealing of phosphorus and boron-doped Si NCs. As a result of the annealing step the plasmon significantly blue-shifts for phosphorus-doped Si NCs. For boron-doped Si NCs, the annealing treatment is able to generate additional free carriers, leading to a plasmon resonance to develop. **(b)** FTIR spectra of as-produced, oxidized and subsequent annealed at 200°C phosphorus-doped and boron-doped silicon nanocrystals. While the plasmon resonance is removed after oxidation, an annealing treatment is able to bring the plasmon resonance back. **(c)** Development of the plasmon resonance for phosphorus-doped Si NCs after oxidation, subsequent annealing followed by re-oxidation for 1, 2, 3 and 4 days. **(d)** EPR spectra for phosphorus-doped Si NCs. A distinct difference is observed between annealed and (re-)oxidized NCs, agreeing with the FTIR spectra of (c).

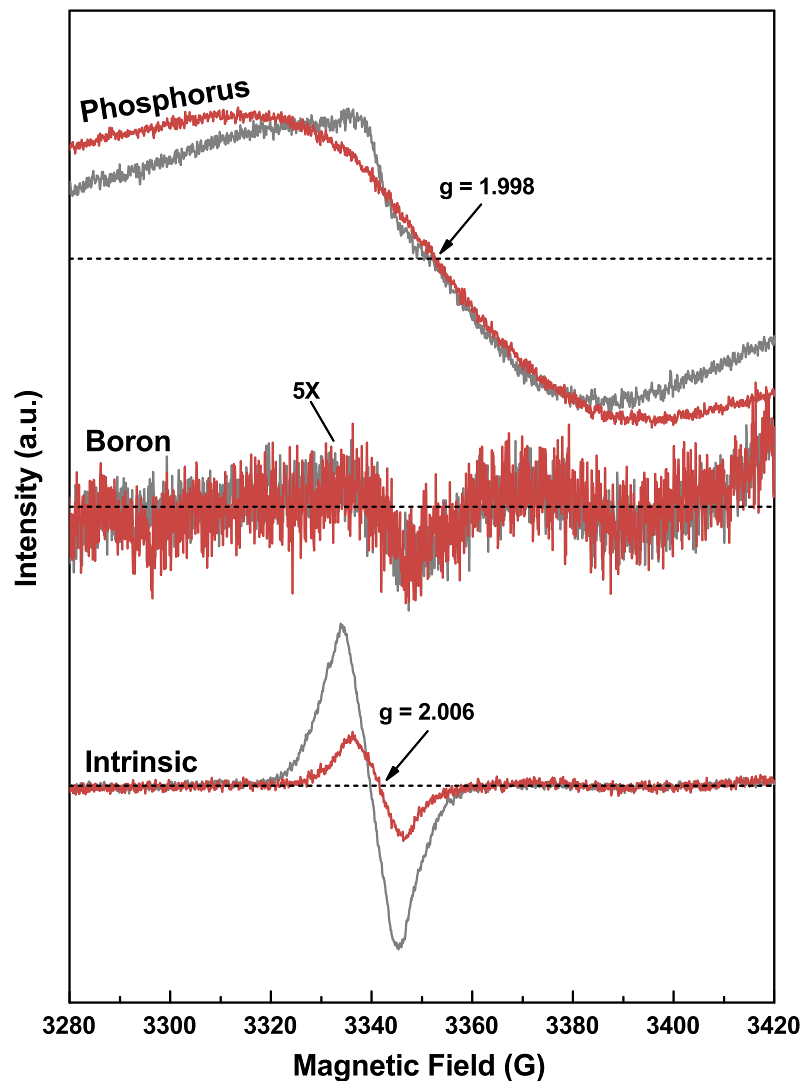

Figure 5.6: **EPR on annealed Si NCs.** Electron Paramagnetic Resonance (EPR) spectra for as-produced (gray) and annealed (red) Si NCs. A reduction in signal is observed for annealed intrinsic NCs as a result of surface restructuring and defect reduction. A feature is also removed from the phosphorus-doped spectra, likely caused by a similar reduction in defects. The boron-doped spectrum does not change significantly after annealing.

5.3 Conclusion

Here we studied the plasmonic properties and dopant dynamics of phosphorus-doped and boron-doped Si NCs. While the synthesis and doping method are identical, phosphorus-doped and boron-doped Si NCs show very different plasmonic behavior which is strongly influenced by their surface properties. We observed LSPRs for as-produced phosphorus-doped Si NCs with high doping concentrations. Furthermore, as-produced boron-doped Si NCs did not have a plasmonic response. This can be attributed to the dopant position and dynamics during NC synthesis. The majority of phosphorus and boron dopants are expected to reside on the surface of the Si NC where they are inactive. Additionally, computational results have shown that a larger fraction of phosphorus atoms are incorporated into the Si NC core than boron atoms, which agrees with the observed plasmonic behavior.

The importance of the surface characteristics was studied in detail using oxidation and low-temperature annealing treatments. Oxidation of the particles again shows opposite dopant behavior, where a LSPR is present in oxidized boron-doped Si NCs, while it is removed for oxidized phosphorus-doped Si NCs. This behavior can be reversed by removing the oxide, showing the importance of the presence of an oxide shell.

For phosphorus-doped Si NCs, EPR measurements showed a significant increase in defects after oxidation. We also observed a strong increase in phosphorus-oxide formation from XPS measurements. As a result, the increase in trap states and formation of phosphorus-oxide are likely responsible for the elimination of the LSPR.

Boron-doped Si NCs behave different and show evidence of surface doping after oxidation. XPS and EPR both show only minor changes to the boron and silicon composition after oxidation. This indicates that the Si NCs do not form a traditional silicon-oxide, but instead form a thin boron-oxide shell around the core. After oxidation this shell provides the free carriers that lead to the LSPRs that are observed. Therefore the doping of the NCs is a surface effect. This is in contrast to traditional doping mechanisms, in which the dopants need to be placed within the core of the nanocrystal.

Finally the significance of post-synthesis annealing treatments is shown. Plasmonic behavior for both phosphorus and boron dopants was observed, indicating that annealing is able to generate additional free-carriers for both cases. This is likely caused by

NC surface restructuring and defect passivation. These results give valuable insight into plasmonic and dopant dynamics of Si NCs, and depict the importance of NC surface properties on the plasmonic properties of NCs.

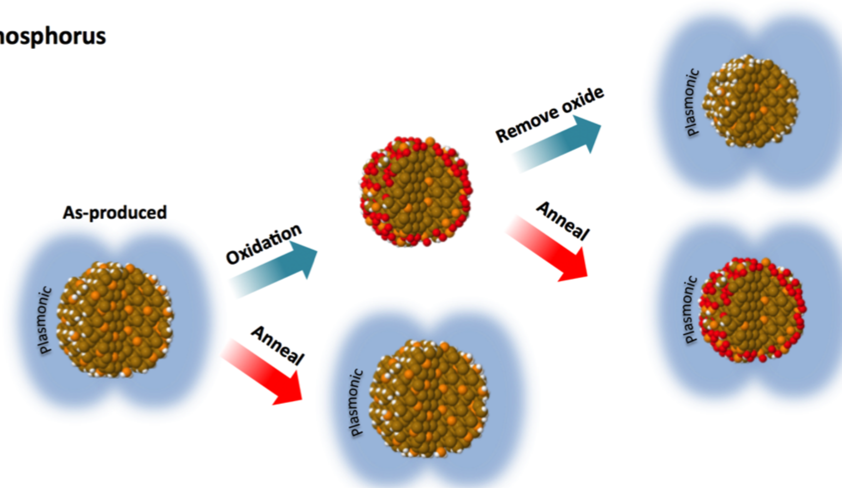

Figure 5.7: **Phosphorus-doped silicon nanocrystal plasmonic overview.** Summary for the plasmonic behavior of phosphorus-doped silicon nanocrystals. A plasmon resonance is observed for as-produced nanocrystals once the doping concentrations exceeds 5%. Post-synthesis treatments allow for further tuning of the resonance position.

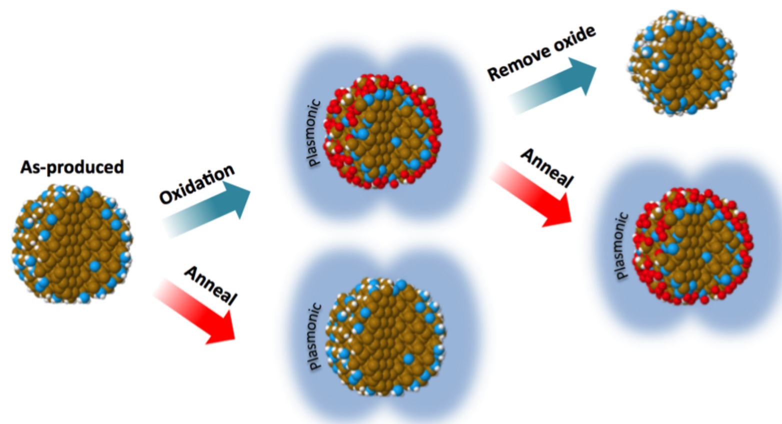

Figure 5.8: **Boron-doped silicon nanocrystal plasmonic overview.** Plasmonic behavior of boron-doped silicon nanocrystals. As-produced nanocrystals do not exhibit a plasmon resonance, but after a post-synthesis annealing or oxidation treatment the plasmonic resonance emerges.

5.4 Future work

The possibility of producing air-stable plasmonic materials makes these nanomaterials interesting for applications. Research is ongoing by Dr. Jihua Yang to apply these plasmonic materials in transmission window systems. However, there is an array of applications where the plasmonic properties of these materials can be applied which would be interesting to explore further.

Tuning of these plasmonics will be critical for successful use in applications. An unexplored area is tuning of the plasmon resonance position by charge injection. First plasmonic nanomaterials are deposited on substrates that contain electrodes. Then by applying a voltage to the film of nanoparticles the number of charges is increased, and as a result the plasmonic resonance is expected to shift as well. Such an approach was successfully applied by the Milliron group at UT Austin,[117] and should also be pursued for plasmonic Si NCs.

While the behavior of boron dopants in silicon nanocrystals has been extensively studied in this work, there are still questions that remain unanswered. A collaboration with the Mkoyan group is underway to study the particles using high resolution transmission electron microscopy (TEM) and a collection of analysis attachments. Interesting behavior was observed in Electron Energy Loss Spectroscopy (EELS). A significant shift ($\sim$10 eV) was observed in the onset energy of oxidized and annealed boron-doped nanoparticles. Such a drastic shift has never been observed and will be studied in more detail as it might provide further insight in the activation mechanism of the dopants in the nanoparticles.

A greater understanding of the dopant positions is needed as well. A collaboration with The National Institute of Standards and Technologies (NIST) is initiated to use high-energy X-Ray Diffraction (HE-XRD) to obtain the atomic pair distribution function of phosphorus-doped and boron-doped nanoparticles. This technique allows us to obtain a better understanding of the dopant positions and what the dopants are bonded to.

So far all the measurements have been done on nanocrystals in film form. It would be interesting to investigate the interaction between nanocrystals and the surrounding lattice. The density of the film can have a direct impact on the interaction of the

plasmonic resonances between nanocrystals. This effect has so far been neglected but is important to better understand to properties of these nanocrystals. The boron-doped nanocrystals can also be studied in solution form, where the interaction is minimized even further.

Finally an interesting experiment would be to look into the strain of the nanoparticle crystal structure. Using XRD, the peak shift of silicon can be investigated to determine the amount of strain in the lattice. It is expected that the addition of dopants to the lattice will cause a measurable increase in strain. This amount of strain can tell us more about the incorporation of dopants in nanocrystals.

5.5 Experimental methods

Nanoparticle Synthesis. Silicon nanocrystals are synthesized in a continuous-flow, low-pressure plasma reactor from an argon-silane (SiH_4) gas mixture. Dopants are introduced by addition of phosphine (PH_3) or diborane (B_2H_6) to the gas mixture. The reactor consists of a borosilicate glass tube through which the reactant gases are flown. Typical flow rates are 30 - 50 standard cubic centimeters per minute (sccm) of argon, 0.4 - 0.6 sccm of silane, 0 - 2 sccm of diborane diluted in hydrogen (10%) and 0 - 2 sccm of phosphine diluted in hydrogen (15%). Radio frequency (rf) power is supplied at 110 W and 13.56 MHz to ring electrodes to form crystalline silicon nanoparticles in the plasma. The NCs are collected directly onto glass substrates, silicon wafers, or aluminum-coated silicon wafers and transferred air-free to a nitrogen-purged glovebox using a push-rod assembly.

FTIR. Fourier Transform Infrared Spectroscopy (FTIR) experiments were conducted in either a nitrogen-purged glovebox or directly in air using a Bruker Alpha FTIR spectrometer in DRIFTS mode or transmission mode. Spectra were collected by averaging 20 scans at 2 cm^{-1} resolution.

Oxide Etching. Hydrofluoric acid (HF) vapor etching (50% in water) of oxidized Si NCs was performed in a room-temperature container. The oxide was removed after exposing the Si NCs to the vapor for 2 to 4 hours. After etching, the samples were transferred air-free to a nitrogen-purged glovebox for further analysis.

XPS. X-ray Photoelectron Spectroscopy (XPS) spectra are acquired on a Surface Science Laboratories, Inc. SSX-100 XPS with a monochromatic Al Kα X-ray source. A X-ray power of 200 W with a 1 mm^2 spot size was used. Si NC samples are prepared by directly impacting a $<$50 nm thin film of Si NCs onto a gold-coated Si wafer. B1s and P1p peaks were obtained by integrating scans for 2.5 hours. Peaks are assigned by using the C1s peak as a reference at 285 eV.

EPR. Electron Paramagnetic Resonance (EPR) measurements were taken using a Bruker Continuous Wave Elexsys E500 electron paramagnetic resonance spectrometer. For the measurements, a few milligrams of Si NC powder was pressed into the bottom of sample tubes (suprasil quartz), and the open end of the tubes was sealed with epoxy glue in order to enable their transport from the glovebox to the EPR spectrometer without exposing the NCs to air. The spectra were normalized to the weight of the nanoparticles.

XRD. X-ray Diffraction (XRD) from nanoparticles was collected using a Bruker-AXS Microdiffractometer with a 2.2 kW sealed Cu x-ray source. The nanoparticle diameter is calculated from the Scherrer equation.

TEM. Transmission Electron Microscope (TEM) images of the doped nanoparticles were collected on lacy-carbon grids and examined with a Tecnai G2 F30 transmission electron microscope.

EDX. Energy Dispersive X-ray Spectroscopy (EDX) data was collected using a JSM-6610LV SEM with an Oxford Instruments Inca X-Act EDS system. Doped Si NCs were deposited on conductive carbon tape for atomic concentration measurement.

Acknowledgements

The work of N.J.K. and U.R.K. was supported by the DOE Plasma Science Center for Predictive Control of Plasma Kinetics. The work of K.S.S. and U.R.K. was supported by the Army Office of Research under MURI Grant W911NF-12-1-0407. Part of this work was carried out in the College of Science and Engineering Characterization Facility,

University of Minnesota, which has received capital equipment funding from the NSF through the UMN MRSEC program. Part of this work also used the College of Science and Engineering Minnesota Nanocenter, University of Minnesota, which receives partial support from NSF through the NNIN program.

Chapter 6

Boron-Doped Silicon Nanocrystals in Media Spanning from Hexane to Water[‡]

6.1 Introduction

More than three decades of research has launched colloidal NCs from the laboratory to a viable optoelectronic technology platform. As the industry grows, so does the need for non-toxic alternatives to Cd and Pb-based NCs. In opposition to typical solution-based techniques,[149] nonthermal plasmas have emerged as the most prolific synthetic method for abundant and non-toxic group IV NCs.[12] However, the resulting nanopowder remains difficult to process without a secondary step to bind an alkane ligand to the surface to render them dispersible in nonpolar solvents.[150] The strength of the Si-C bond makes ligand exchange strategies[151,152] championed by metal-based NCs ineffective. Encouraging results have emerged recently that circumvent the need of a ligand. Plasma-synthesized Si[153] and Ge[154] NCs terminated with chlorine have shown colloidal stability in relatively polar solvents. The electron-withdrawing nature of chlorine renders Si or Ge NC surface atoms Lewis acidic and able to engage in "hypervalent" three-center two-electron bonds with Lewis basic solvent molecules. This

[‡]Portions of this chapter are in preparation for publication under the authorship of Lance M. Wheeler, Nicolaas J Kramer and Uwe R. Kortshagen.

hypervalent interaction was found to be critical to colloid stability. In this chapter we build on previous synthesis and doping results to form novel ligand-less Si NC inks, and demonstrate the possibilities of these inks by forming conductive thin-films using cheap and convenient deposition techniques.

6.2 Boronated surface

So far we have applied dopants for tuning of the electronic properties of nanocrystals. However, boron dopant atoms are also found to be highly beneficial for the formation of incredibly versatile nanocrystal inks. To accomplish this we employ a strategy to produce a Lewis acidic surface using boron atoms. Monodisperse 8 nm (within ~15%) Si NCs with a boronated surface are produced by introducing a boron precursor (B_2H_6) with SiH_4 during plasma synthesis. Identical nanocrystals were also applied in Chapters 4 and 5. Figure 6.1a shows a XPS spectrum of the B(1s) peak of the as-synthesized Si NCs. The spectrum is deconvolved into four peaks wherein the sharpest blue peak at ~188 eV corresponds to tetravalent boron (B(IV)) that is incorporated into the NC. The two smaller high binding energy peaks are also boron in the B(IV) state but bonded to oxygen atoms at the Si NC surface.[146] This is validated by the Fourier transform infrared (FTIR) spectra in Figure 6.1b, as the peak corresponding to ν(Si-B-O) increases in relative intensity after brief air exposure.

The broad peak centered at ~185 eV (red) is the trivalent state of boron (B(III)).[146] Peak integration of the XPS spectrum reveals ~65% of the boron is in the B(III) state, which resides on the Si NC surface. First principles calculations show B atoms to energetically favor surface segregation to the Si NC surface in a trivalent coordination as opposed to substitutional incorporation.[155] In this state, boron has only three valence electrons, while there are four valence orbitals, 2s, $2p_x$, $2p_y$, and $2p_z$. The extra vacant valence orbital make boron a Lewis acid in the classical sense.

The Lewis acidic Si NC surface is now analogous to that of a metal-based NC. As such, we are able to demonstrate oleylamine ligand coordination to the boron surface sites. After binding ligands to the surface, they can be dispersed in the nonpolar solvents typically used in these systems such as hexane or toluene. Figure 6.1d shows a photograph of a biphasic solution of oleylamine-capped Si NCs dispersed in hexane

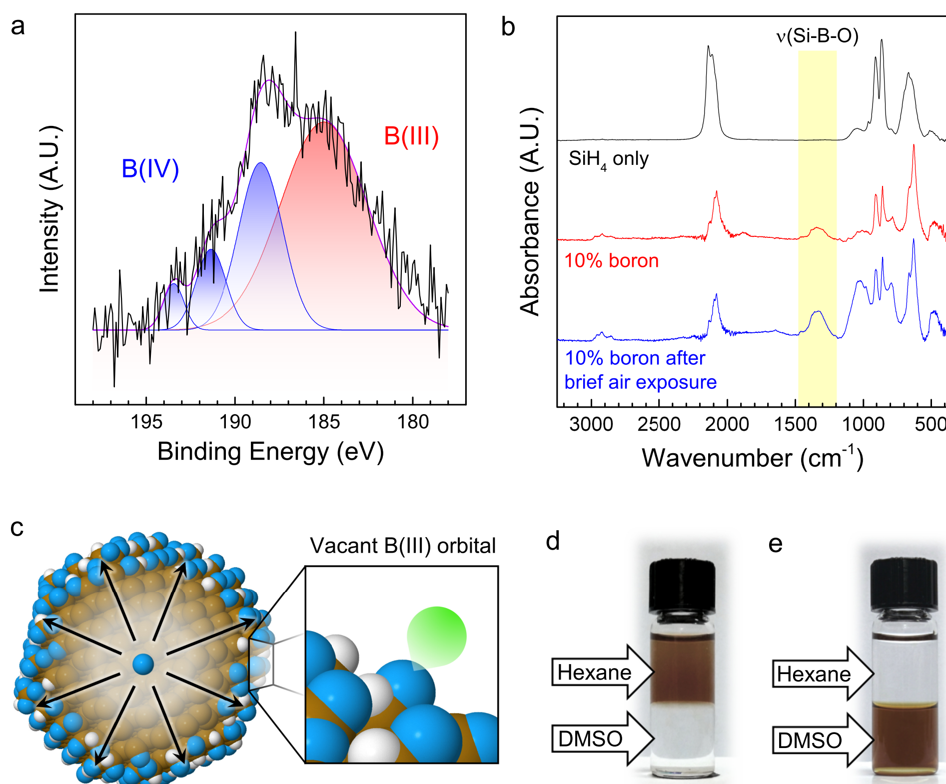

Figure 6.1: **Lewis acidic Si NC surface.** **(a)** XPS B1s spectrum of Si NCs as they are produced from the plasma reaction. Surface B(III) accounts for ∼60% of the boron in the sample. **(b)** FTIR spectra of Si NCs synthesized from SiH_4 only (black), from SiH_4 and 10 atomic percent boron (red), and Si NC sample produced from 10 atomic percent boron after a brief exposure to air. **(c)** Cartoon representation of B segregation to the Si NC surface to form Lewis acidic B(III) groups. **(d, e)** Photographs of biphasic solutions of hexane and DMSO. In (d), oleylamine-capped Si NCs are stable in hexane, and in (e) Si NCs are stable in DMSO without a ligand. (Figure adapted from Lance Wheeler)

over dimethylsulfoxide (DMSO). The oleylamine-capped Si NCs are dramatically different from what has been previously demonstrated with covalent Si-C-R[150] or Si-O-R[156] ligands; the ligands are bound by an acid-base complex, not covalent bond.

Boronated Si NCs will form extremely dense colloids (>50 mg/ml) when dispersed into strong Lewis basic solvents such DMSO, N-methylpyrrolidone (NMP), or dimethylacetamide (DMA) without any secondary chemical treatment to the NC surface. There has been significant attention within the NC community in developing ligand-stripped NCs[157,158] or NCs with bound ionic ligand.[152,159–162]

In the case for Boronated Si NCs a strongly bound layer of solvent is present on the NC surface. However, unlike ligand treated Si NCs, this layer of solvent can simply be removed using an annealing treatment or under vacuum. This strongly bound solvent layer allows for another interesting phenomenon. When a solvent that provides colloidal stability is first added, the Si NCs can now be diluted with solvents such as water, nitromethane, pyridine, and toluene, even though these solvents would not provide stability by themselves. This covers relative permittivities from ϵ=80.3 (water) down to ϵ=2.3 (toluene). For example, Si NCs first stabilized in DMSO are stable in 95% toluene. It would seem the characteristics of the cosolvent are of negligible importance to the solvent interacting with the NC surface. Interestingly, this observation was actually briefly reported previously by Dong *et al.* who noticed NCs would stabilize in water only if dimethylformamide is added as well.[158]

The FTIR spectra of Figure 6.2c illustrate a particularly attractive cosolvent system of NMP and water. Water-stable NCs are desirable for biocompatibility and cost reasons. We can demonstrate Si NC stability in solutions of 94% water by first forming a highly concentrated solution in NMP, then diluting with water. Even at high volume fractions of water, signal from NMP molecules can be prominently observed in the FTIR spectrum. Interestingly, even at 10% water by volume, The surface of the Si NCs remain unoxidized. It appears the boronated NC surface in addition to the NMP molecules bound to the surface through an acid-base complex actually protect the Si NCs from oxidation. This is observed by a lack of Si-O-Si vibration at 1090 cm^{-1}. Si NCs are typically extremely reactive in ambient air atmosphere,[138] but these solutions were stored in ambient condition for weeks before FTIR was measured. Moreover, Figure 6.2d shows that simply pulling modest vacuum ($\sim 10^{-3}$ torr) will remove adsorbed

water from the surface of the NC. This will be an important attribute for further development of optoelectronics device-quality thin films cast from these colloids.

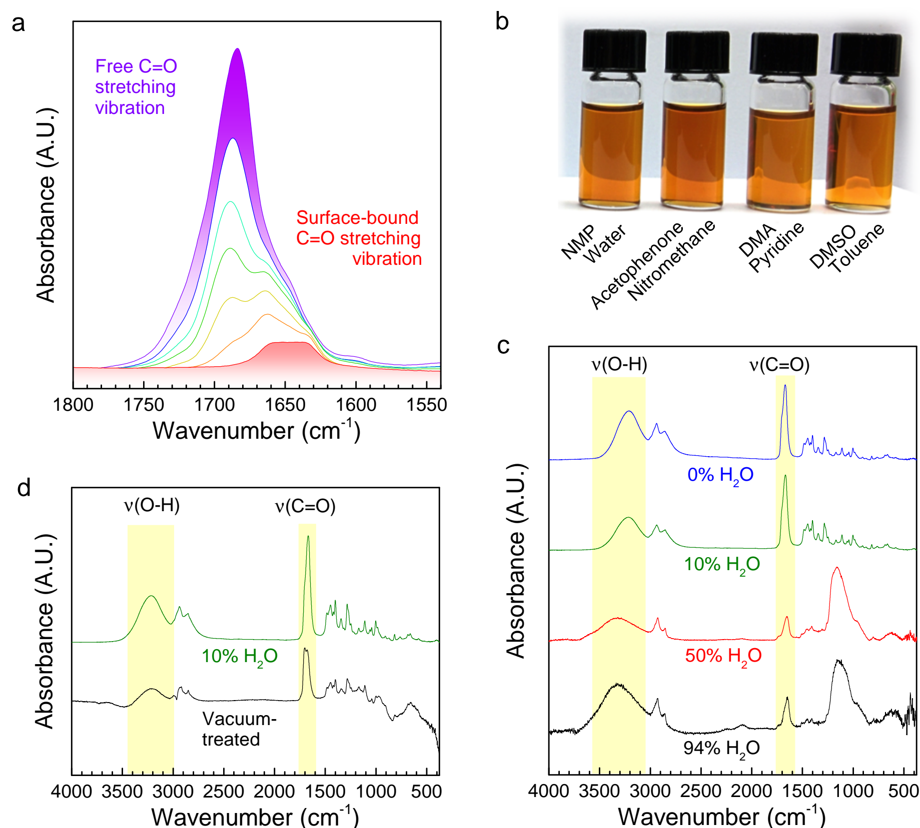

Figure 6.2: **Cosolvent effects on colloidal stability.** **(a)** FTIR spectra of the C=O stretching vibration of NMP taken as a function of time as NMP evaporates from Si NC colloid. **(b)** A photograph of 50% volume mixtures of a variety of cosolvent systems. **(c)** FTIR spectra for films of Si NCs cast from NMP/water mixture of varying volume fractions. Spectra are normalized and offset for clarity. **(d)** FTIR spectra of Si NC film cast from a solution of NMP and 10% water by volume before (green) and after (black) vacuum-treating the sample. Spectra are offset. (Figure adapted from Lance Wheeler)

6.3 Spray coating

Now that dense Si NC colloids can be formed, the next step is to explore alternative deposition techniques for nanocrystal thin films. Solution-processed semiconductors offer the promise of low-cost, production-scale optoelectronic devices such as solar cells. Unfortunately, most reports are limited to lab-scale, batch-processing methods such as spin coating and dip coating. Spray coating allows for large scale thin film deposition and has been previously successfully applied for organic and quantum dot solar cells.[9,163–165] Its ease of use in combination with the ability to coat large surfaces make this a very attractive deposition tool.

The boron-doped Si NC inks are an excellent candidate for spray coated thin films. This is mainly due to their flexibility in terms of solvent choice and robustness against oxidation. Here we explore the thin film formation of boron-doped Si NCs using spray coating and determine the optimal conditions for uniform and dense thin films. To explore the effect of the solvent properties on the thin films we used DMSO and methanol as the solvent for Si NC inks.

We found a strong dependence of the film morphology on the substrate temperature, solvent choice and the Si NC ink flow rate through the gun. An example of undesirable films are shown in Figure 6.3. Large “web-like” structures (Figure 6.3a) are formed when substrate temperatures are relatively high. For DMSO, these webbed structures appear once substrates temperatures exceed 130°C. To explain this we have to consider the drying process of these films. As the substrate temperature will affect the evaporation rate of the solvent, it is expected that rapid solvent evaporation gives rise to such structures. At low temperatures, the nanocrystals are given more time to arrange into a uniform film, leading to smoother depositions.

At certain conditions we also observed micrometer-sized spheres on top of the nanocrystal film, as is shown in Figure 6.3b. Further investigation confirms that the spheres consist of a collection of agglomerated Si NCs. We found that the agglomerates form when using lean spraying conditions, in which the ratio of NC ink to nitrogen gas is low. The agglomerates are likely a result of in-flight solvent evaporation and subsequent agglomeration of NCs.[166] This process is enhanced for smaller droplet and can therefore be tuned using the NC ink flow rate or solution concentration. It also strongly depends

on the solvent evaporation rate. A significant increase in the agglomerate density was found when methanol was used instead of DMSO. This provides further evidence for the in-flight drying process, as methanol will evaporate significantly faster compared to DMSO. By increasing the NC ink flow rate and decreasing the NC concentration in the solvent, the agglomerates were eliminated. While these agglomerates are undesirable for thin-film applications, they are potentially interesting for certain applications that require high surface areas such as batteries.

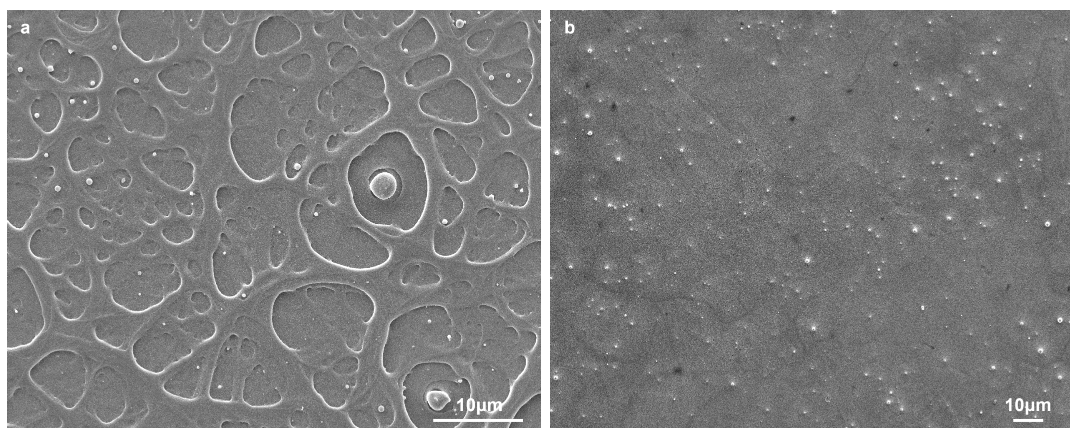

Figure 6.3: **Film morphology for spray coated films. (a)** Top-view SEM image of web-like film structures resulting from fast solvent evaporation. **(b)** Spherical Si NC agglomerates deposited on top of the NC films during spray coating.

After optimization of the spray coating process we were able to deposit smooth and uniform films with a thickness of 100 nm. Thicker films can be produced by simply increasing the number of coatings. An example of such an optimized film is shown in Figure 6.4. The film thickness is uniform across the substrate and no agglomerates are observed. Making such films requires a high NC ink flow rate combined with a substrate temperature of approximately 80°C. This allows the droplets to coalesce on the substrate and evaporate slowly while the NCs arrange themselves and form a thin film. Sufficient time between sprays is necessary, as large droplets might form on the substrate leading to uneven film deposition.

Finally we were not only able to apply thin films onto silicon wafer substrates, but also apply our knowledge to flexible substrates as well. Flexible electronics are

interesting for a variety of applications and an increasing number of flexible electronic devices are entering the market place these days. The first step in the fabrication of such a device is the deposition of a thin semiconductor films, which is what we explored here. Kapton substrates were coated with our boron-doped Si NC inks, and similar to the silicon substrates,we were able to produce very uniform films. As the Kapton itself has some surface roughness, the resulting films are slightly rougher compared to films on silicon substrates. Also, bending of the Kapton substrates did not significantly affect the film properties.

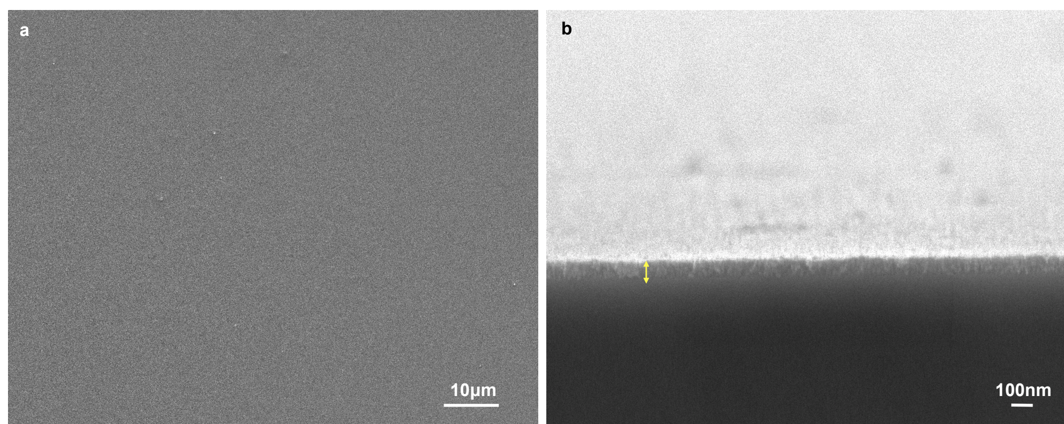

Figure 6.4: **Uniform thin-film of Si NCs deposited using the spray coating technique.** **(a)** Top-view SEM image of the NC film on a silicon wafer substrate. **(b)** Side-view profile of a ∼100 nm thick Si NC thin film.

6.4 Conclusion

The boronated silicon surface provides a robust new stabilization route for Si NC colloids. The lack of ligands, protection against oxidation, the ability to use a wide array of solvents and concentrations that exceed 50 mg/ml make these colloids an exciting new frontier in silicon-based inks. Not only does the boron act as a Lewis acid on the surface of the nanoparticle, it also acts as a dopants in the NC as shown in Chapters 4 & 5, making these films conductive as well.

Using these NC inks, we showed that uniform NC thin films can be produced on large

scales using spray coating techniques. Not only is this method very simple and cost-effective, it also produces high-quality films that are comparable with more advanced deposition techniques. However, finding the appropriate spray coating conditions is essential for uniform films. It was found that high substrate temperatures lead to web-like structures, while large NC agglomerates were produced when the NC ink flow rate was low. Both effects are caused by evaporation of the solvent, and are therefore dependent on the type of solvent that is used.

6.5 Future Work

Boron-doped silicon NCs offer a great platform for silicon-based electronic inks. However, the exact mechanism for stabilization is still unclear and is being investigated in more detail by Lance Wheeler. Understanding these colloids is essential for moving to field of electronic inks forward. Once understood, other materials such as germanium or silicon-germanium alloys should also be explored. These can then by applied in FET as was described in Chapter 4.

Another area of interest in the optoelectronic properties of the boron-coated silicon nanocrystals. Now that dense solutions can be formed, the luminescence of these particles should be investigated and optimized. Ideally, the boron surface chemistry would be decoupled from dopant incorporation, as dopants will strongly quench the luminescence.

The spray coating experiments proved that high-quality films of Si NCs can be produced. So far these films have been made by hand, and while this produces excellent films after some training, an automated system would be highly desirable to improve the consistency even further. Designing such an automated system should not be complex, as the number of movements is limited.

Other deposition systems besides spray coating should also be used. An interesting area of research is printing of electronic inks. A very fine control of the deposition can be achieved which is desirable for certain applications, especially if the luminescent properties can be improved. The control might also be of interest for plasmonic applications.

Finally the electronic performance of spray coated films needs to be investigated. Ideally a comparison should be made with traditional spin coated films or FETs to

understand how the spray coating affects the nanocrystal film. This can be combined with ellipsometry measurements to characterize the film density. This work should be extended to flexible substrates as well. We have shown that uniform films can be produced on flexible Kapton substrates, and it would be interesting to produce FETs out of these flexible films.

6.6 Experimental methods

Si NC synthesis. Si NCs are synthesized in a continuous-flow nonthermal plasma reactor from gas mixture of argon, silane, and diborane. The gas flows through a borosilicate glass tube with a pair of copper ring electrodes secured to it. Typical flow rates are 30–50 standard cubic centimetres per minute (sccm) of argon, 0.4–0.6 sccm of silane, 0–2 sccm of diborane diluted in hydrogen (10%). 13.56 MHz radiofrequency power at 110 to 130 W is supplied to the ring electrodes to strike a plasma and yield crystalline Si NCs. A rectangular nozzle controls the gas pressure in the plasma region by restricting the flow. Adjusting the width of the nozzle opening allows for the pressure to change independently of the gas flow. This method is used to produce nanocrystals at reactor pressures ranging from 90 to 150 Pa. As a result, the nanoparticle size can be precisely controlled between 5 and 15 nm. 8 nm Si NCs are used throughout this study.

Si NC collection and colloid formation. Powder samples of silicon nanocrystals are collected directly from the gas-phase by impacting them onto a substrate mounted onto a manual feed-through located inside the reactor. A rectangular nozzle is placed in between the deposition and plasma region to accelerate the particles and impact them directly onto the substrate. The substrate is then retracted into a portable loadlock and transferred air-free to a N_2-purged glovebox for further processing. Si NCs are weighed and dispersed in various solvents.

XPS. XPS spectra are acquired on a Surface Science Laboratories, Inc. SSX-100 XPS with a monochromatic Al K_α X-ray source. A X-ray power of 200 W with a 1×1 mm^2 spot size was used. Si NC samples are prepared by directly impacting a $<$50 nm thin film of Si NCs onto a Au-coated Si wafer. B1s peaks were obtained taken by integrating

scans for ∼6 hours. Peaks are assigned by using the C1s peak as a reference at 285 eV.

Chemicals. The following solvents were purchased from Sigma Aldrich (purity and grade are included if available): triethylamine (99%, ACS), tetrahydrofuran (≥99.9%, anhydrous), pyridine (≥99.8%, puriss), 1,4-dioxane (99.8%, anhydrous), dimethylacetamide (99.9%, puriss), dimethyl sulfoxide (≥99.9%, ACS), benzonitrile (99%, Reagent Plus), ethanol (99%, anhydrous), methanol (99%, anhydrous), propylene carbonate (PC) (99.9%, HPLC), formamide (≥99.5%, ACS), water (deionized), 1,2-dicholorobenzene, (99%, anhydrous), nitromethane (≥98.5%, puriss), toluene (99.9%, HPLC), hexane (≥95%, spetrophotometric). The following solvents were purchased from Acros Organics: N-methyl-2-pyrrolidone (99%), acetophenone (98%, extra pure) Sodium Iodide (ACS) was purchased from J.T. Baker and dehydrated by pulling vacuum on a schlenkline and heating to 150°C. Cesium Iodide (99.998%, ultra-dry) was purchased form Alfa Aesar and used as received. 1.5 M stock solutions of DMSO electrolyte were prepared in a N_2-purged glovebox by stirring the salt with a magnetic stir bar until the solution turned clear.

FTIR. FTIR experiments were done on a diamond ATR crystal or using the diffuse reflectance attachment on a Bruker Alpha FTIR spectrometer inside a N_2-atmosphere glovebox. Spectra were typically collected by averaging 20 scans at 2 cm^{-1} resolution.

Spray Coating. The spray coating system was placed in a small glovebox to eliminate exposure to solvents. The airbrush was connected directly to a nitrogen tank and pressures were varied using a gas regulator. The airbrush was positioned horizontally, and directed at a vertically placed hot plate, onto which the substrate was taped onto. Five main variables were studied in this work: distance between airbrush and substrate, nitrogen pressure, hot plate temperature, Si NC colloid flow rate and solvents.

- Distance: The distance is defined as the distance between the tip of the airbrush to the substrate surface. The range of distances tested was 1-25 centimeters.
- Nitrogen pressure: This is the nitrogen pressure that flows through the airbrush allowing the colloid to be atomized and forced out of the airbrush. The pressure

range for this experiment was set at 15 - 50 psi using a gas regulator.

- Hot Plate Temperature: The substrate was placed directly onto the hot plate to control the temperature of the substrate, which controlled the evaporation rate of the solvent. The temperature ranged from room temperature up to 200°C depending on the solvent used for the ink. The substrate was allowed to warm up for 15 mins for the temperature to reach equilibrium.
- Si NC Ink flow rate: This is defined as the amount of ink in microliters exiting the airbrush per second. The flow rate ranged from 3 - 170 μL/s. The flow rate of 170 μL was the maximum flow rate for the airbrush.
- Solvent: Two different solvents were used: Methanol and Dimethyl Sulfoxide (DMSO). The solvents used for this experiment were chosen for their ability to disperse the silicon nanoparticles and create a clear and stable colloid. A nanoparticle concentration of 3 mg/ml was used.

Substrate Preparation. Before each spray coating experiment the silicon substrates were cleaned using a heated piranha solution for 15 minutes, rinsed with deionized water, and then placed in a UV Ozone chamber for 30 minutes. Kapton substrates were also used but could not be cleaned using the piranha solution. Instead the Kapton substrates were cleaned with acetone and isopropanol and then rinsed with deionized water, followed by 30 minute UV ozone exposure.

SEM. Silicon and Kapton substrates were analyzed using a JEOL 6500 scanning electron microscope to determine the film morphology and thickness. A 5 nm platinum coating was applied to the samples to reduce charging.

Acknowledgements

The authors thank Jeff Pietryga, Chris Hogan, and Chris Sorensen for helpful and stimulating discussion. The spray coating experiments were conducted by Reid Herd.

References

[1] U S Energy Information Administration. International Energy Outlook 2013. 2013.

[2] Frost & Sullivan. Total Printed Electronics Market. 2010.

[3] X D Pi, R W Liptak, J Deneen Nowak, N P Wells, C B Carter, S A Campbell, and U Kortshagen. Air-stable full-visible-spectrum emission from silicon nanocrystals synthesized by an all-gas-phase plasma approach. *Nanotechnology*, 19(24):245603–6, 2008.

[4] A J Labelle, S M Thon, S Masala, M M Adachi, H Dong, M Farahani, A H Ip, A Fratalocchi, and E H Sargent. Colloidal Quantum Dot Solar Cells Exploiting Hierarchical Structuring. *Nano Letters*, 15(2):1101–1108, 2015.

[5] QD Vision - http://www.qdvision.com.

[6] O Neumann, A S Urban, J Day, S Lal, P Nordlander, and N J Halas. Solar Vapor Generation Enabled by Nanoparticles. *ACS Nano*, 7(1):42–49, 2013.

[7] M G Panthani and B A Korgel. Nanocrystals for Electronics. *Annual Review of Chemical and Biomolecular Engineering*, 3(1):287–311, 2012.

[8] L E Brus. Electron–electron and electron-hole interactions in small semiconductor crystallites: The size dependence of the lowest excited electronic state. *The Journal of Chemical Physics*, 80(9):4403–8, 1984.

[9] I J Kramer, J C Minor, G Moreno-Bautista, L Rollny, P Kanjanaboos, D Kopilovic, S M Thon, G H Carey, K W Chou, D Zhitomirsky, A Amassian, and E H Sargent.

Efficient Spray-Coated Colloidal Quantum Dot Solar Cells. *Advanced Materials*, 27(1):116–121, 2014.

[10] L Mangolini and U Kortshagen. Plasma-Assisted Synthesis of Silicon Nanocrystal Inks. *Advanced Materials*, 19(18):2513–2519, 2007.

[11] H Kamiya and M Iijima. Surface modification and characterization for dispersion stability of inorganic nanometer-scaled particles in liquid media. *Science and Technology of Advanced Materials*, 11(4):044304–8, 2010.

[12] U R Kortshagen. Nonthermal Plasma Synthesis of Semiconductor Nanocrystals. *Journal of Physics D-Applied Physics*, 42(11):113001, 2009.

[13] D J Rowe and U R Kortshagen. Boron- and phosphorus-doped silicon germanium alloy nanocrystals—Nonthermal plasma synthesis and gas-phase thin film deposition. *APL Materials*, 2(2):022104–6, 2014.

[14] P Roura, J Farjas, A Pinyol, and E Bertran. The crystallization temperature of silicon nanoparticles. *Nanotechnology*, 18(17):175705, 2007.

[15] T Lopez and L Mangolini. Low activation energy for the crystallization of amorphous silicon nanoparticles. *Nanoscale*, 6(3):1286–1294, 2014.

[16] M Hirasawa, T Orii, and T Seto. Size-dependent crystallization of Si nanoparticles. *Applied Physics Letters*, 88(9):093119–093119–3, 2006.

[17] R N Carlile, S Geha, J F O'Hanlon, and J C Stewart. Electrostatic trapping of contamination particles in a process plasma environment. *Applied Physics Letters*, 59(10):1167–4, 1991.

[18] U Kortshagen and U Bhandarkar. Modeling of particulate coagulation in low pressure plasmas. *Physical Review E*, 60(1):887, 1999.

[19] S J Choi and M J Kushner. The role of negative ions in the formation of particles in low-pressure plasmas. *Journal of Applied Physics*, 74(2):853–861, 1993.

[20] Z C Holman and U R Kortshagen. A Flexible Method for Depositing Dense Nanocrystal Thin Films: Impaction of Germanium Nanocrystals. *Nanotechnology*, 21(33):335302, 2010.

[21] R J Anthony, K Y Cheng, Z C Holman, R J Holmes, and U R Kortshagen. An all-gas-phase approach for the fabrication of silicon nanocrystal light-emitting devices. *Nano Letters*, 2012.

[22] D J Norris, A L Efros, and S C Erwin. Doped Nanocrystals. *Science*, 319(5871):1776–1779, 2008.

[23] S C Erwin, L Zu, M I Haftel, A L Efros, T A Kennedy, and D J Norris. Doping semiconductor nanocrystals. *Nature*, 436(7047):91–94, 2005.

[24] G Dalpian and J Chelikowsky. Self-Purification in Semiconductor Nanocrystals. *Physical Review Letters*, 96(22):226802–4, 2006.

[25] F V Mikulec, M Kuno, M Bennati, D A Hall, R G Griffin, and M G Bawendi. Organometallic Synthesis and Spectroscopic Characterization of Manganese-Doped CdSe Nanocrystals. *Journal of the American Chemical Society*, 122(11):2532–2540, 2000.

[26] D J Rowe, J S Jeong, K A Mkhoyan, and Uwe Kortshagan. Phosphorus-doped silicon nanocrystals exhibiting mid-infrared localized surface plasmon resonance. *Nano Letters*, 2013.

[27] S Zhou, X Pi, Z Ni, Q Luan, Y Jiang, C Jin, T Nozaki, and D Yang. Boron- and phosphorus-hyperdoped silicon nanocrystals. *Particle & Particle Systems Characterization*, 2014.

[28] X Pi. Doping Silicon Nanocrystals with Boron and Phosphorus. *Journal of Nanomaterials*, 2012(12):1–9, 2012.

[29] H Sugimoto, M Fujii, K Imakita, S Hayashi, and K Akamatsu. Codoping n- and p-Type Impurities in Colloidal Silicon Nanocrystals: Controlling Luminescence Energy from below Bulk Band Gap to Visible Range. *The Journal of Physical Chemistry C*, 117(22):11850–11857, 2013.

[30] H Sugimoto, M Fujii, K Imakita, S Hayashi, and K Akamatsu. Phosphorus and Boron Codoped Colloidal Silicon Nanocrystals with Inorganic Atomic Ligands. *The Journal of Physical Chemistry C*, 117(13):6807–6813, 2013.

[31] J M Luther, P K Jain, T Ewers, and A P Alivisatos. Localized surface plasmon resonances arising from free carriers in doped quantum dots. *Nature materials*, 10(5):361–366, 2011.

[32] A Comin and L Manna. New materials for tunable plasmonic colloidal nanocrystals. *Chemical Society Reviews*, 43(11):3957–3975, 2014.

[33] Y Zhao, H Pan, Y Lou, X Qiu, J Zhu, and C Burda. Plasmonic CuS Nanocrystals: Optical and Structural Properties of Copper-Deficient Copper(I) Sulfides. *Journal of the American Chemical Society*, 131(12):4253–4261, 2009.

[34] D J de Aberasturi, A B Serrano-Montes, and L M Liz-Marzán. Modern Applications of Plasmonic Nanoparticles: From Energy to Health. *Advanced Optical Materials*, 2015.

[35] H Tan, R Santbergen, A H M Smets, and M Zeman. Plasmonic Light Trapping in Thin-film Silicon Solar Cells with Improved Self-Assembled Silver Nanoparticles. *Nano Letters*, 12(8):4070–4076, 2012.

[36] J N Anker, W P Hall, O Lyandres, N C Shah, J Zhao, and R P Van Duyne. Biosensing with plasmonic nanosensors. *Nature materials*, 7(6):442–453, 2008.

[37] X Huang, P K Jain, I H El-Sayed, and M A El-Sayed. Plasmonic photothermal therapy (PPTT) using gold nanoparticles. *Lasers in Medical Science*, 23(3):217–228, 2007.

[38] V Giannini, A I Fernández-Domínguez, S C Heck, and S A Maier. Plasmonic Nanoantennas: Fundamentals and Their Use in Controlling the Radiative Properties of Nanoemitters. *Chemical reviews*, 111(6):3888–3912, 2011.

[39] L Mangolini, E Thimsen, and U Kortshagen. High-yield plasma synthesis of luminescent silicon nanocrystals. *Nano Letters*, 5(4):655–659, 2005.

[40] X D Pi, R W Liptak, J Deneen Nowak, N P Wells, C B Carter, S A Campbell, and U Kortshagen. Air-stable full-visible-spectrum emission from silicon nanocrystals synthesized by an all-gas-phase plasma approach. *Nanotechnology*, 19(24):245–603, 2008.

[41] U R Kortshagen. Nonthermal plasma synthesis of semiconductor nanocrystals. *Journal of Physics D-Applied Physics*, 42(11):113001, 2009.

[42] A Bapat, M Gatti, Y Ding, S A Campbell, and U R Kortshagen. A plasma process for the synthesis of cubic-shaped silicon nanocrystals for nanoelectronic devices. *Journal of Physics D-Applied Physics*, 40(8):2247–2257, 2007.

[43] Z C Holman and U R Kortshagen. A flexible method for depositing dense nanocrystal thin films: impaction of germanium nanocrystals. *Nanotechnology*, 21(33):335302, 2010.

[44] R Gresback, T Nozaki, and K Okazaki. Synthesis and oxidation of luminescent silicon nanocrystals from silicon tetrachloride by very high frequency nonthermal plasma. *Nanotechnology*, 22(30):305605, 2011.

[45] R Gresback, R Hue, W L Gladfelter, and U R Kortshagen. Combined plasma gas-phase synthesis and colloidal processing of InP/ZnS core/shell nanocrystals. *Nanoscale Research Letters*, 6(1):68, 2011.

[46] M A Lieberman and A J Lichtenberg. *Principles of plasma discharges and materials processing.* New York:Wiley, 1994.

[47] J Goree. Charging of particles in a plasma. *Plasma Sources Science and Technology*, 3(3):400–406, 1999.

[48] T Matsoukas and M Russell. Particle charging in low-pressure plasmas. *Journal of Applied Physics*, 77(9), 1995.

[49] F Galli and U R Kortshagen. Charging, coagulation, and heating model of nanoparticles in a low-pressure plasma accounting for ion-neutral collisions. *IEEE Transactions on Plasma Science*, 38(4):803–809, 2010.

[50] V A Schweigert and I V Schweigert. Coagulation in a low-temperature plasma. *Journal of Physics D-Applied Physics*, 29(3):655–659, 1996.

[51] U Kortshagen and U Bhandarkar. Modeling of particulate coagulation in low pressure plasmas. *Physical Review E*, 60(1):887–898, 1999.

[52] G S Selwyn. Trapping and behavior of particulates in a radio frequency magnetron plasma etching tool. *Journal of Vacuum Science & Technology A: Vacuum, Surfaces, and Films*, 11(4):1132, 1993.

[53] R J Anthony and U R Kortshagen. Photoluminescence quantum yields of amorphous and crystalline silicon nanoparticles. *Physical Review B*, 80(11):115407, 2009.

[54] D J Rowe, J S Jeong, K A Mkhoyan, and U R Kortshagen. Phosphorus-doped silicon nanocrystals exhibiting mid-infrared localized surface plasmon resonance. *Nano Letters*, 13(3):1317–1322, 2013.

[55] S C Erwin, L Zu, M I Haftel, A L Efros, and T A Kennedy. Doping semiconductor nanocrystals. *Nature*, 436(7047):91–94, 2005.

[56] A N Goldstein. The melting of silicon nanocrystals: submicron thin-film structures derived from nanocrystal precursors. *Applied Physics A Materials Science & Processing*, 62(1):33–37, 1996.

[57] J E Daugherty and D B Graves. Particulate temperature in radio frequency glow discharges. *Journal of Vacuum Science & Technology A: Vacuum, Surfaces, and Films*, 11(4):1126, 1993.

[58] G H P M Swinkels, H Kersten, H Deutsch, and G M W Kroesen. Microcalorimetry of dust particles in a radio-frequency plasma. *Journal of Applied Physics*, 88(4):1747–1755, 2000.

[59] E Stoffels, W W Stoffels, H Kersten, G H P M Swinkels, and G M W Kroesen. Surface processes of dust particles in low pressure plasmas. *Plasma Sources Science and Technology*, T89(1):168, 2001.

[60] L Mangolini and U R Kortshagen. Selective nanoparticle heating: another form of nonequilibrium in dusty plasmas. *Physical Review E*, 79(2):026405, 2009.

[61] H R Maurer and H Kersten. On the heating of nano- and microparticles in process plasmas. *Journal of Physics D-Applied Physics*, 44(17):174029, 2011.

[62] T Hawa and M Zachariah. Coalescence kinetics of bare and hydrogen-coated silicon nanoparticles: A molecular dynamics study. *Physical Review B*, 71(16):165434, 2005.

[63] N St J Braithwaite, J-P Booth, and G Cunge. A novel electrostatic probe method for ion flux measurements. *Plasma Sources Science and Technology*, 5:667–684, 1996.

[64] M C Petcu, A C Bronneberg, A Sarkar, M A Blauw, M Creatore, and M C M van de Sanden. A capacitive probe with shaped probe bias for ion flux measurements in depositing plasmas. *Review of Scientific Instruments*, 79(11):115104, 2008.

[65] M Malyshev and V Donnelly. Trace rare gases optical emission spectroscopy: Nonintrusive method for measuring electron temperatures in low-pressure, low-temperature plasmas. *Physical Review E*, 60(5):6016–6029, 1999.

[66] H R Maurer, R Basner, and H Kersten. Temperature of particulates in low-pressure rf-plasmas in Ar, Ar/H2 and Ar/N2 mixtures. *Contributions to Plasma Physics*, 50(10):954–961, 2010.

[67] J Goree and C Cui. Fluctuations of the charge on a dust grain in a plasma. *IEEE Transactions on Plasma Science*, 22:151–158, 1994.

[68] C Kendrick, G Klafehn, T Guan, I Anderson, H Shen, J Redwing, and R Collins. Controlled growth of SiNPs by plasma synthesis. *Solar Energy Materials and Solar Cells*, 124:1–9, 2014.

[69] E Thimsen, U R Kortshagen, and E S Aydil. Plasma synthesis of stoichiometric Cu_2S nanocrystals stabilized by oleylamine. *Chemical Communications*, 50(61):8346–8349, 2014.

[70] P Felbier, J Yang, J Theis, R W Liptak, A Wagner, A Lorke, G Bacher, and U R Kortshagen. Highly luminescent ZnO quantum dots made in a nonthermal plasma. *Advanced Functional Materials*, 24(14):1988–1993, 2014.

[71] İ Doğan, N J Kramer, R H J Westermann, K Dohnalová, A H M Smets, M A Verheijen, T Gregorkiewicz, and M C M van de Sanden. Ultrahigh throughput plasma processing of free standing silicon nanocrystals with lognormal size distribution. *Journal of Applied Physics*, 113(13):134306, 2013.

[72] A R Stegner, R N Pereira, K Klein, R Lechner, R Dietmueller, M S Brandt, M Stutzmann, and H Wiggers. Electronic transport in phosphorus-doped silicon nanocrystal networks. *Physical Review Letters*, 100(2), 2008.

[73] X D Pi, R Gresback, R W Liptak, S A Campbell, and U Kortshagen. Doping efficiency, dopant location, and oxidation of Si nanocrystals. *Applied Physics Letters*, 92(12), 2008.

[74] A R Stegner, R N Pereira, R Lechner, K Klein, H Wiggers, M Stutzmann, and M S Brandt. Doping efficiency in freestanding silicon nanocrystals from the gas phase: Phosphorus incorporation and defect-induced compensation. *Physical Review B*, 80(16), 2009.

[75] R Gresback, N J Kramer, Y Ding, T Chen, U R Kortshagen, and T Nozaki. Controlled doping of silicon nanocrystals investigated by solution-processed field effect transistors. *ACS Nano*, 8(6):5650–5656, 2014.

[76] U R Kortshagen, E J Thimsen, L Mangolini, A Bapat, and D Jurbergs. Process and apparatus for forming nanoparticles using radiofrequency plasmas. *U.S. Patent 7,446,335*, 2008.

[77] N J Kramer, R J Anthony, M Mamunuru, E S Aydil, and U R Kortshagen. Plasma-induced crystallization of silicon nanoparticles. *Journal of Physics D-Applied Physics*, 47(7):075202, 2014.

[78] F Galli and U R Kortshagen. Charging, coagulation, and heating model of nanoparticles in a low-pressure plasma accounting for ion–neutral collisions. *IEEE Transactions on Plasma Science*, 38(4):803–809, 2010.

[79] H R Maurer and H Kersten. On the heating of nano- and microparticles in process plasmas. *Journal of Physics D-Applied Physics*, 44(17), 2011.

[80] S Askari, I Levchenko, K Ostrikov, P Maguire, and D Mariotti. Crystalline Si nanoparticles below crystallization threshold: Effects of collisional heating in non-thermal atmospheric-pressure microplasmas. *Applied Physics Letters*, 104(16):163103, 2014.

[81] T Nozaki, K Sasaki, T Ogino, D Asahi, and K Okazaki. Microplasma synthesis of tunable photoluminescent silicon nanocrystals. *Nanotechnology*, 18(23):235603, 2007.

[82] L G D'yachkov, A G Khrapak, S A Khrapak, and G E Morfill. Model of grain charging in collisional plasmas accounting for collisionless layer. *Physics of Plasmas*, 14(4):042102, 2007.

[83] M Lampe, V Gavrishchaka, G Ganguli, and G Joyce. Effect of trapped ions on shielding of a charged spherical object in a plasma. *Physical Review Letters*, 86(23):5278–5281, 2001.

[84] V Fortov, A Ivlev, S Khrapak, A Khrapak, and G Morfill. Complex (dusty) plasmas: Current status, open issues, perspectives. *Physics reports*, 421(1-2):1–103, 2005.

[85] R Gopalakrishnan and C J Hogan. Coulomb-influenced collisions in aerosols and dusty plasmas. *Physical Review E*, 85(2):026410, 2012.

[86] R Gopalakrishnan, T Thajudeen, H Ouyang, and C J Hogan. The unipolar diffusion charging of arbitrary shaped aerosol particles. *Journal of Aerosol Science*, 64:60–80, 2013.

[87] M Gatti and U R Kortshagen. Analytical model of particle charging in plasmas over a wide range of collisionality. *Physical Review E*, 78(4):046402, 2008.

[88] J E Allen. Probe theory - the orbital motion approach. *Physica Scripta*, 45(5):497–503, 1992.

[89] S Khrapak, S Ratynskaia, A Zobnin, A Usachev, V Yaroshenko, M Thoma, M Kretschmer, H Höfner, G Morfill, O Petrov, and V Fortov. Particle charge in the bulk of gas discharges. *Physical Review E*, 72(1):016406, 2005.

[90] J E Daugherty, R K Porteous, M D Kilgore, and D B Graves. Sheath structure around particles in low-pressure discharges. *Journal of Applied Physics*, 72(9):3934–3942, 1992.

[91] R N Varney. Mean free paths, ion drift velocities, and the poisson distribution. *American Journal of Physics*, 39(5):534–538, 1971.

[92] D J Norris, A L Efros, and S C Erwin. Doped Nanocrystals. *Science*, 319(5871):1776–1779, 2008.

[93] A Sahu, M S Kang, A Kompch, C Notthoff, A W Wills, D Deng, M Winterer, C D Frisbie, and D J Norris. Electronic Impurity Doping in CdSe Nanocrystals. *Nano Letters*, 12(5):2587–2594, 2012.

[94] D K Kim, A T Fafarman, B T Diroll, S H Chan, T R Gordon, C B Murray, and C R Kagan. Solution-Based Stoichiometric Control over Charge Transport in Nanocrystalline CdSe Devices. *ACS Nano*, 7(10):8760–8770, 2013.

[95] A W Wills, M S Kang, Katherine M Wentz, Sophia E Hayes, A Sahu, Wayne L Gladfelter, and D J Norris. Synthesis and characterization of Al- and In-doped CdSe nanocrystals. *Journal of Materials Chemistry*, 22(13):6335–6342, 2012.

[96] M S Kang, A Sahu, C D Frisbie, and D J Norris. Influence of Silver Doping on Electron Transport in Thin Films of PbSe Nanocrystals. *Advanced Materials*, 25(5):725–731, 2013.

[97] S J Oh, N E Berry, J Choi, E A Gaulding, T Paik, S-H Hong, C B Murray, and C R Kagan. Stoichiometric Control of Lead Chalcogenide Nanocrystal Solids to Enhance Their Electronic and Optoelectronic Device Performance. *ACS Nano*, 7(3):2413–2421, 2013.

[98] L Mangolini, E Thimsen, and U Kortshagen. High-yield plasma synthesis of luminescent silicon nanocrystals. *Nano Letters*, 5(4):655–659, 2005.

[99] R Gresback, N J Kramer, Y Ding, T Chen, U R Kortshagen, and T Nozaki. Controlled Doping of Silicon Nanocrystals Investigated by Solution-Processed Field Effect Transistors. *ACS Nano*, 8(6):5650–5656, 2014.

[100] J M Luther, M Law, Qing Song, C L Perkins, Matthew C Beard, and A J Nozik. Structural, Optical, and Electrical Properties of Self-Assembled Films of PbSe Nanocrystals Treated with 1,2-Ethanedithiol. *ACS Nano*, 2(2):271–280, 2008.

[101] Y Liu, M Gibbs, James Puthussery, Steven Gaik, R Ihly, Hugh W Hillhouse, and M Law. Dependence of Carrier Mobility on Nanocrystal Size and Ligand Length in PbSe Nanocrystal Solids. *Nano Letters*, 10(5):1960–1969, 2010.

[102] M J Powell, S C Deane, and W I Milne. Bias-stress-induced creation and removal of dangling-bond states in amorphous silicon thin-film transistors. *Applied Physics Letters*, 60(2):207–209, 1992.

[103] S Deane, R Wehrspohn, and M Powell. Unification of the time and temperature dependence of dangling-bond-defect creation and removal in amorphous-silicon thin-film transistors. *Physical Review B*, 58(19):12625–12628, 1998.

[104] S M Sze and Kwok K Ng. *Physics of Semiconductor Devices*. Sze/Physics. John Wiley & Sons, Inc., Hoboken, NJ, USA, 2006.

[105] A Stegner, R Pereira, R Lechner, K Klein, H Wiggers, M Stutzmann, and M Brandt. Doping efficiency in freestanding silicon nanocrystals from the gas phase: Phosphorus incorporation and defect-induced compensation. *Physical Review B*, 80(16):165326, 2009.

[106] A L Efros and B I Shklovskii. Critical Behaviour of Conductivity and Dielectric Constant near the Metal-Non-Metal Transition Threshold. *physica status solidi (b)*, 76(2):475–485, 1976.

[107] J Clerc, G Giraud, S Alexander, and E Guyon. Conductivity of a mixture of conducting and insulating grains: Dimensionality effects. *Physical Review B*, 22(5):2489–2494, 1980.

[108] H Lepage, A Kaminski-Cachopo, A Poncet, and G le Carval. Simulation of Electronic Transport in Silicon Nanocrystal Solids. *The Journal of Physical Chemistry C*, 116(20):10873–10880, 2012.

[109] K Seino, F Bechstedt, and P Kroll. Tunneling of electrons between Si nanocrystals embedded in a SiO2 matrix. *Physical Review B*, 86(7):075312, 2012.

[110] D C Hannah, J Yang, N J Kramer, G C Schatz, U R Kortshagen, and R D Schaller. Ultrafast Photoluminescence in Quantum-Confined Silicon Nanocrystals Arises from an Amorphous Surface Layer. *ACS Photonics*, 1(10):960–967, 2014.

[111] L R Hirsch, R J Stafford, J A Bankson, S R Sershen, B Rivera, R E Price, J D Hazle, N J Halas, and J L West. Nanoshell-mediated near-infrared thermal therapy of tumors under magnetic resonance guidance. *PNAS*, 100(23):13549–13554, 2003.

[112] P K Jain, X Huang, I H El-Sayed, and M A El-Sayed. Review of Some Interesting Surface Plasmon Resonance-enhanced Properties of Noble Metal Nanoparticles and Their Applications to Biosystems. *Plasmonics*, 2(3):107–118, 2007.

[113] E C Dreaden, A M Alkilany, X Huang, C J Murphy, and M A El-Sayed. The golden age: gold nanoparticles for biomedicine. *Chemical Society Reviews*, 41(7):2740–2779, 2012.

[114] S Pillai, K R Catchpole, T Trupke, and M A Green. Surface plasmon enhanced silicon solar cells. *Journal of Applied Physics*, 101(9):093105, 2007.

[115] E Ozbay. Plasmonics: Merging photonics and electronics at nanoscale dimensions. *Science*, 311(5758):189–193, 2006.

[116] C Clavero. Plasmon-induced hot-electron generation at nanoparticle/metal-oxide interfaces for photovoltaic and photocatalytic devices. *Nature Photonics*, 8(2):95–103, 2014.

[117] A Llordes, G Garcia, J Gazquez, and D J Milliron. Tunable near-infrared and visible-light transmittance in nanocrystal-in-glass composites. *Nature*, 500(7462):323–326, 2013.

[118] X Liu and M T Swihart. Heavily-doped colloidal semiconductor and metal oxide nanocrystals: an emerging new class of plasmonic nanomaterials. *Chemical Society Reviews*, 43(11):3908–3920, 2014.

[119] M Vollmer and U Kreibig. *Optical properties of metal clusters*. Springer Ser. Mat. Sci, 1995.

[120] M Kanehara, H Koike, T Yoshinaga, and T Teranishi. Indium Tin Oxide Nanoparticles with Compositionally Tunable Surface Plasmon Resonance Frequencies in the Near-IR Region. *Journal of the American Chemical Society*, 131(49):17736–17737, 2009.

[121] R Buonsanti, A Llordes, S Aloni, B A Helms, and D J Milliron. Tunable Infrared Absorption and Visible Transparency of Colloidal Aluminum-Doped Zinc Oxide Nanocrystals. *Nano Letters*, 11(11):4706–4710, 2011.

[122] D J Rowe, J S Jeong, K A Mkhoyan, and U R Kortshagen. Phosphorus-Doped Silicon Nanocrystals Exhibiting Mid-Infrared Localized Surface Plasmon Resonance. *Nano Letters*, 13(3):1317–1322, 2013.

[123] S Zhou, X Pi, Z Ni, Y Ding, Y Jiang, C Jin, Christophe Delerue, D Yang, and T Nozaki. Comparative Study on the Localized Surface Plasmon Resonance of Boron- and Phosphorus-Doped Silicon Nanocrystals. *ACS Nano*, page 150105153003007, 2015.

[124] D Dorfs, T Härtling, K Miszta, N C Bigall, M R Kim, A Genovese, A Falqui, M Povia, and L Manna. Reversible Tunability of the Near-Infrared Valence Band Plasmon Resonance in Cu 2– xSe Nanocrystals. *Journal of the American Chemical Society*, 133(29):11175–11180, 2011.

[125] L Liu, H Zhong, Z Bai, T Zhang, W Fu, L Shi, H Xie, L Deng, and B Zou. Controllable Transformation from Rhombohedral Cu 1.8S Nanocrystals to Hexagonal CuS Clusters: Phase- and Composition-Dependent Plasmonic Properties. *Chemistry of Materials*, 25(23):4828–4834, 2013.

[126] L M Wheeler, N R Neale, T Chen, and U R Kortshagen. Hypervalent surface interactions for colloidal stability and doping of silicon nanocrystals. *Nature Communications*, 4, 2013.

[127] I Kriegel, C Jiang, J Rodríguez-Fernández, R D Schaller, D V Talapin, E da Como, and J Feldmann. Tuning the Excitonic and Plasmonic Properties of Copper Chalcogenide Nanocrystals. *Journal of the American Chemical Society*, 134(3):1583–1590, 2012.

[128] E Thimsen, Melissa Johnson, Xin Zhang, Andrew J Wagner, K A Mkhoyan, U R Kortshagen, and E S Aydil. High electron mobility in thin films formed via supersonic impact deposition of nanocrystals synthesized in nonthermal plasmas. *Nature Communications*, 5:5822–5822, 2014.

[129] X Chen, X Pi, and D Yang. Critical Role of Dopant Location for P-Doped Si Nanocrystals. *The Journal of Physical Chemistry C*, 2010.

[130] J Ma, S-H Wei, N R Neale, and A J Nozik. Effect of surface passivation on dopant distribution in Si quantum dots: The case of B and P doping. *Applied Physics Letters*, 98(17):173103, 2011.

[131] J Ma and S-H Wei. Chemical trend of the formation energies of the group-III and group-V dopants in Si quantum dots. *Physical Review B*, 87(11):115318, 2013.

[132] R Guerra and S Ossicini. Preferential Positioning of Dopants and Co-Dopants in Embedded and Freestanding Si Nanocrystals. *Journal of the American Chemical Society*, 136(11):4404–4409, 2014.

[133] X Pi, X Chen, and D Yang. First-Principles Study of 2.2 nm Silicon Nanocrystals Doped with Boron. *The Journal of Physical Chemistry C*, 115(20):9838–9843, 2011.

[134] J Ristein. Surface transfer doping of semiconductors. *Science*, 313(5790):1057–1058, 2006.

[135] Wei Chen, Dongchen Qi, Xingyu Gao, and Andrew Thye Shen Wee. Surface transfer doping of semiconductors. *Progress in Surface Science*, 84(9-10):279–321, 2009.

[136] N Cabrera and N F Mott. Theory of the oxidation of metals. *Reports on Progress in Physics*, 12(1):163–184, 1949.

[137] S Niesar, A R Stegner, R N Pereira, M Hoeb, H Wiggers, M S Brandt, and M Stutzmann. Defect reduction in silicon nanoparticles by low-temperature vacuum annealing. *Applied Physics Letters*, 96(19):193112–193112–3, 2010.

[138] R N Pereira, D J Rowe, R J Anthony, and U Kortshagen. Oxidation of freestanding silicon nanocrystals probed with electron spin resonance of interfacial dangling bonds. *Physical Review B*, 83(15):155327, 2011.

[139] J Quirt and J Marko. Absolute Spin Susceptibilities and Other ESR Parameters of Heavily Doped n-Type Silicon. I. Metallic Samples. *Physical Review B*, 5(5):1716–1728, 1972.

[140] K Sumida, K Ninomiya, M Fujii, K Fujio, S Hayashi, M Kodama, and H Ohta. Electron spin-resonance studies of conduction electrons in phosphorus-doped silicon nanocrystals. *Journal of Applied Physics*, 101(3):033504, 2007.

[141] K Fujio, M Fujii, K Sumida, S Hayashi, M Fujisawa, and H Ohta. Electron spin resonance studies of P and B codoped Si nanocrystals. *Applied Physics Letters*, 93(2):021920, 2008.

[142] A Stegner, R Pereira, K Klein, R Lechner, R Dietmueller, M Brandt, M Stutzmann, and H Wiggers. Electronic Transport in Phosphorus-Doped Silicon Nanocrystal Networks. *Physical Review Letters*, 100(2):026803, 2008.

[143] S Zhou, Y Ding, X Pi, and T Nozaki. Doped silicon nanocrystals from organic dopant precursor by a SiCl4-based high frequency nonthermal plasma. *Applied Physics Letters*, 105(18), 2014.

[144] B Puthen Veettil, Lingfeng Wu, Xuguang Jia, Ziyun Lin, Tian Zhang, Terry Yang, Craig Johnson, Dane McCamey, Gavin Conibeer, and Ivan Perez-Würfl. Passivation effects in B doped self-assembled Si nanocrystals. *Applied Physics Letters*, 105(22):222108, 2014.

[145] M Perego, C Bonafos, and M Fanciulli. Phosphorus doping of ultra-small silicon nanocrystals. *Nanotechnology*, 21(2):025602, 2009.

[146] T Kazahaya and M Hirose. Coordination-Number of Doped Boron Atoms in Photochemically-Deposited Amorphous-Silicon Studied by X-Ray Photoelectron-Spectroscopy. *Japanese Journal of Applied Physics Part 2-Letters*, 25(1):L75–L77, 1986.

[147] K Tsutsui, T Matsuda, M Watanabe, C-G Jin, Y Sasaki, B Mizuno, E Ikenaga, K Kakushima, A Ahmet, T Maruizumi, H Nohira, T Hattori, and H Iwai. Activated boron and its concentration profiles in heavily doped Si studied by soft x-ray

photoelectron spectroscopy and Hall measurements. *Journal of Applied Physics*, 104(9):093709, 2008.

[148] J Yamauchi, Y Yoshimoto, and Y Suwa. Identification of boron clusters in silicon crystal by B1s core-level X-ray photoelectron spectroscopy: A first-principles study. *Applied Physics Letters*, 99(19):191901, 2011.

[149] Y Yin and A P Alivisatos. Colloidal nanocrystal synthesis and the organic–inorganic interface. *Nature*, 437(7059):664–670, 2004.

[150] R J Anthony, D J Rowe, M Stein, J Yang, and U R Kortshagen. Routes to Achieving High Quantum Yield Luminescence from Gas-Phase-Produced Silicon Nanocrystals. *Advanced Functional Materials*, 21(21):4042–4046, 2011.

[151] M Law, J M Luther, Q Song, B K Hughes, C L Perkins, and A J Nozik. Structural, optical, and electrical properties of PbSe nanocrystal solids treated thermally or with simple amines. *Journal of the American Chemical Society*, 130(18):5974–5985, 2008.

[152] M V Kovalenko, M Scheele, and D V Talapin. Colloidal nanocrystals with molecular metal chalcogenide surface ligands. *Science*, 324(5933):1417–1420, 2009.

[153] L M Wheeler, N R Neale, T Chen, and U R Kortshagen. Hypervalent surface interactions for colloidal stability and doping of silicon nanocrystals. *Nature Communications*, 4, 2013.

[154] Z C Holman and U R Kortshagen. Nanocrystal Inks without Ligands: Stable Colloids of Bare Germanium Nanocrystals. *Nano Letters*, 11(5):2133–2136, 2011.

[155] X Pi, X Chen, and D Yang. First-principles study of 2.2 nm silicon nanocrystals doped with boron. *The Journal of Physical Chemistry C*, 115(20):9838–9843, 2011.

[156] J D Holmes, K J Ziegler, R C Doty, L E Pell, K P Johnston, and B A Korgel. Highly luminescent silicon nanocrystals with discrete optical transitions. *Journal of the American Chemical Society*, 123(16):3743–3748, 2001.

[157] E L Rosen, R Buonsanti, A Llordes, A M Sawvel, D J Milliron, and B A Helms. Exceptionally Mild Reactive Stripping of Native Ligands from Nanocrystal Surfaces

by Using Meerwein's Salt. *Angewandte Chemie International Edition*, 51(3):684–689, 2012.

[158] A Dong, X Ye, J Chen, Y Kang, T Gordon, J M Kikkawa, and C B Murray. A generalized ligand-exchange strategy enabling sequential surface functionalization of colloidal nanocrystals. *Journal of the American Chemical Society*, 133(4):998–1006, 2010.

[159] Maksym V Kovalenko, Maryna I Bodnarchuk, Jana Zaumseil, Jong-Soo Lee, and D V Talapin. Expanding the Chemical Versatility of Colloidal Nanocrystals Capped with Molecular Metal Chalcogenide Ligands. *Journal of the American Chemical Society*, 132(29):10085–10092, 2010.

[160] A Nag, M V Kovalenko, J S Lee, W Liu, B Spokoyny, and D V Talapin. Metal-free Inorganic Ligands for Colloidal Nanocrystals. *Journal of the American Chemical Society*, 133(27):10612–10620, 2011.

[161] A Nag, D S Chung, D S Dolzhnikov, N M Dimitrijevic, S Chattopadhyay, T Shibata, and D V Talapin. Effect of Metal Ions on Photoluminescence, Charge Transport, Magnetic and Catalytic Properties of All-Inorganic Colloidal Nanocrystals and Nanocrystal Solids. *Journal of the American Chemical Society*, 134(33):13604–13615, 2012.

[162] A T Fafarman, W-K Koh, B T Diroll, D K Kim, D-K Ko, S J Oh, X Ye, V Doan-Nguyen, M R Crump, D C Reifsnyder, C B Murray, and C R Kagan. Thiocyanate-Capped Nanocrystal Colloids: Vibrational Reporter of Surface Chemistry and Solution-Based Route to Enhanced Coupling in Nanocrystal Solids. *Journal of the American Chemical Society*, 133(39):15753–15761, 2011.

[163] T Wang, N W Scarratt, H Yi, A D F Dunbar, A J Pearson, D C Watters, T S Glen, A C Brook, J Kingsley, A R Buckley, M W A Skoda, A M Donald, R A L Jones, A Iraqi, and D G Lidzey. Fabricating High Performance, DonorAcceptor Copolymer Solar Cells by Spray-Coating in Air. *Advanced Energy Materials*, 3(4):505–512, 2013.

[164] W Nie, R C Coffin, J Liu, Y Li, E D Peterson, C M MacNeill, R E Noftle, and D L Carroll. High efficiency organic solar cells with spray coated active layers comprised of a low band gap conjugated polymer. *Applied Physics Letters*, 100(8), 2012.

[165] G Susanna, L Salamandra, T M Brown, A Di Carlo, F Brunetti, and A Reale. Airbrush spray-coating of polymer bulk-heterojunction solar cells. *Solar Energy Materials and Solar Cells*, 95(7):1775–1778, 2011.

[166] J Bahadur, D Sen, S Mazumder, B Paul, A Khan, and G Ghosh. Evaporation-induced self assembly of nanoparticles in non-buckling regime: Volume fraction dependent packing. *Journal of Colloid and Interface Science*, 351(2):357–364, 2010.

Appendix A

Copyright permissions

Chapters 2 and 3 were published in Journal of Physics D: Applied Physics. IOP Publishing grants authors permission to include the article in a dissertation. Chapter 4 was published in an American Chemical Society (ACS) journal. The ACS copyright policy states: "ACS extends blanket permission to students to include in their theses and dissertations their own articles, or portions thereof, that have been published in ACS journals or submitted to ACS journals for publication, provided that the ACS copyright credit line is noted on the appropriate page(s)".

Appendix B

Self-Assembled Silicon Microstructures from Silicon Nanoparticles

Inertial impaction of nanoparticles allows for fine control of the nanocrystal film morphology. As was described in Chapter 1, nanoparticles are impacted due to the pressure difference between the synthesis and depositions regions, which are separated by an orifice. By changing the downstream conditions such as pressure, distance between the substrate and the orifice and the size and shape of the orifice, the structure of the deposited film can be varied from very dense films to porous depositions. In this work this morphology control was exploited to form ”tree-like” microstructures from silicon nanoparticles. The following table gives an overview of the used experimental conditions. The resulting change in film structure is displayed in Figure B.1 for several deposition conditions.

Figure B.1c shows the formation of porous ”tree-like” structures, caused by shadowing effects during deposition. The formation of these silicon microstructures requires deposition of porous structures by impaction of silicon nanoparticles. The self-assembly of nanoparticles into microstructures has several advantages over traditional microstructure formation mechanisms, and is of interest for use in applications such as solar cells. This is due their reduction in light scattering and large surface area.

Table B.1: Overview of the synthesis conditions for microwire arrays.

	Unit	Value	Notes
Ar Flow Rate	sccm	40 - 110	
SiH_4 Flow Rate	sccm	0.5	
PH_3 Flow Rate	sccm	0 - 1	15% in H_2
B_2H_6 Flow Rate	sccm	0 - 1	10% in H_2
Pressure	Torr	1 - 2	Synthesis Pressure
Orifice	mm	1 - 5	Circular orifice
Power	W	110	RFX
Electrode Distance	cm	2.5 - 5	Measured from bottom flange
Substrate to Orifice Distance	cm	8	Fixed position
Tube Diameter	inch	1	Outer Diameter
Deposition time	minutes	0.5 - 2	Keep substrate stationary during deposition

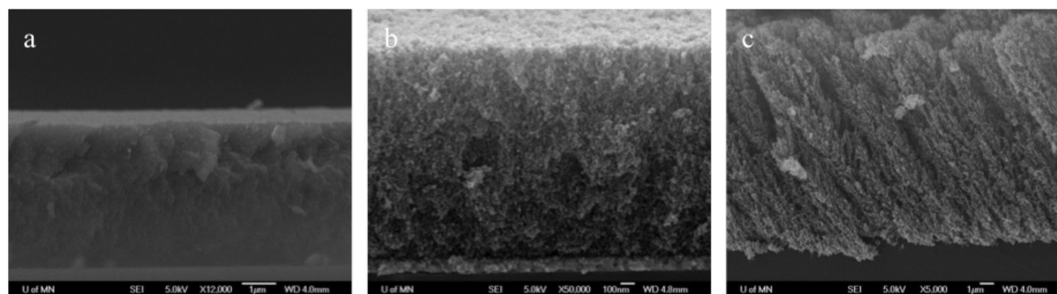

Figure B.1: **Film structure dependence on deposition conditions.** Change in film structure for three deposition conditions. **(a)** A small distance (0.5 cm) between orifice and substrate creates dense nanoparticles films. **(b)** By increasing the distance to 1 cm a more porous structure is formed. **(c)** Using a pinhole orifice placed at a distance of 5 cm from the substrate creates very porous structures.

An annealing treatment allows for further densification to form freestanding structures. This is shown in Figure B.2, where the samples are quickly annealed to temperatures ranging from 700°C up to 1000°C for 10 seconds. While exposure to oxygen cannot be avoided when using RTA, it is minimized by annealing in an argon environment. The chamber is purged with Argon for 2 minutes before the annealing process starts, which is followed by a 10 second ramp to temperatures of up to 1000°C. This temperature is then held for another 10 seconds, followed by a cool-down of approximately 5 minutes. Figure B.2 clearly shows the effect of increasing temperatures on the microstructures, where higher temperatures lead to increased densification.

When the as-deposited and annealed samples are compared, it can be seen that

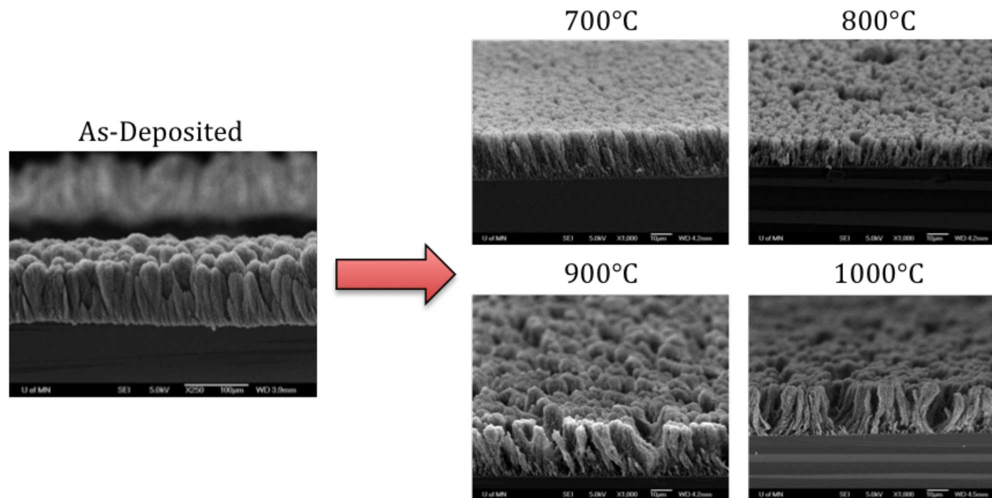

Figure B.2: **Effect of annealing.** Significant densification of the as-deposited structures occurs during annealing. Temperatures of up to 1000°C are reached in the rapid thermal annealer for 10 seconds.

the thickness decreases by a factor of 5 to 10. This shows the significant effect of the annealing on the structures. The length of the wires can be changed by simply varying of the deposition time, allowing for relatively precise control of the wire length. Typical wire lengths after annealing are 10 μm for 2 minutes of nanoparticle deposition.

Besides the distance from the orifice to the substrate, the size of the orifice is also of importance. This is shown in Figure B.3, where three different conditions are compared after annealing. Here the orifice was placed at a distance of 8 cm from the substrate, and the orifice diameter was increased from 1 mm to 3 mm. The samples were all annealed with identical conditions.

While the change in orifice diameter is very minor, very different structures are formed. Several effects could lead to this. When the orifice diameter is increased, the pressure is reduced in the particle formation region. To compensate for this, additional gas has to be flown to increase the pressure. This changes both the particle size and the pressure drop between the particle formation region and deposition region. Also, the Stokes number will be affected when the orifice diameter is changed. Therefore, the exact mechanism is difficult to determine and requires further research.

Dopants can be introduced by mixing doping precursors with argon and silane gasses.

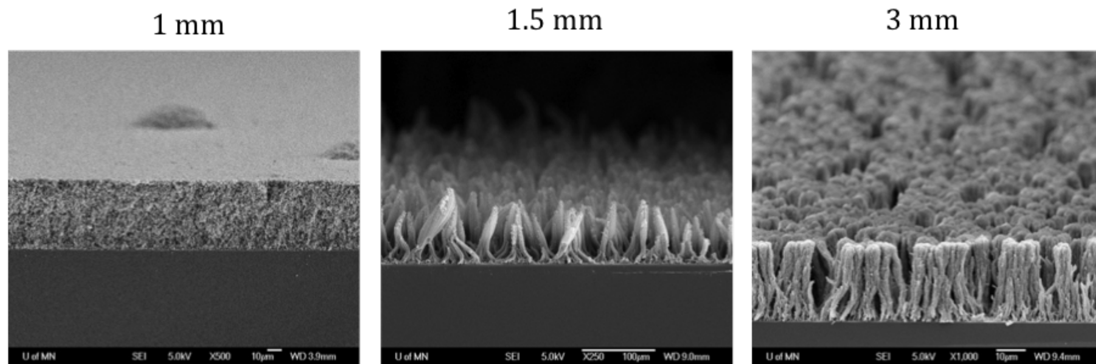

Figure B.3: **Orifice dependence.** The effect on the deposition structures after annealing for different orifice diameters.

This allows for both n-type and p-type doped particles by introducing either phosphine (PH_3) or diborane (B_2H_6) to the plasma, where it will be incorporated into the nanoparticles during growth. The silane to dopant precursor ratio will determine the final dopant concentration in the nanoparticle. This way, doped wire-like structures can be formed with shapes that are similar to structures from intrinsic nanoparticles. The ability to form doped structures is crucial for many applications and specifically for the formation of photovoltaic cells.

The strength of this technique is the separate nanoparticle creation and deposition regimes. The nanoparticle properties, such as size and doping concentration, can be changed while the deposition properties can be held constant. Other materials than silicon, such as germanium, show similar densification behavior and wire formation. It also allows for freedom of the substrate, since the nanoparticle can be deposited on any substrate of choice. Therefore cheaper substrates such as steel can be used for the production of solar cells instead of silicon wafers, which are relatively expensive.

It would be interesting to study the electrical properties of these microwire arrays as well as individual wires. This could be achieved using AFM or a probe in SEM. Several conditions such as wire length, doping and annealing conditions should be investigated to obtain a better understanding of the transport through these wires. The next step is to apply the interesting properties of these wire structures for application. A solar cell could be made by forming p-type microwire structures and coating it with a layer of

n-type amorphous silicon. For optimal performance it is essential that these wires have good conductive properties in order to overcome the 10 μm distance to the substrate.

Appendix C

Nanoparticle Heating Code

Matlab code for nanoparticle heating model

```
%Time-dependent Nanoparticle Heating Model
%Nicolaas Kramer

clear
clc

%Initial conditions & constants, all in m^-3

a_p=2.5E-9;               %Particle radius
kb=1.38E-23;             %Boltzmann Constant
M_gas=40*1.66E-27;       %Mass Argon
n_i=1E20;                %Ion density
T_gas=400;               %Gas temperature
T_e=33000;               %Electron temperature
e=1.6E-19;               %electron charge
m_e=9.11E-31;            %electron mass
epsilon_0=8.85E-12;      %epsilon 0
alpha=2*1.22;
P=1E6;                   %Pressure
n_gas=P/(kb*T_gas);      %Gas density
n_p=1E14;                %Nanoparticle density
n_H=1E18;                %Hydrogen Density
```

```
m_H=1*1.66E-27;            %Mass hydrogen
T_H=T_gas;                 %Hydrogen temperature
C=710;                     %Specific Heat
ro_p=2330;                 %Density
sigma_i=40.9*10^-20;       %Ion-neutral collision cross-section
dt=1E-12;                   %Time step

Heat_EI=0;
Heat_H=0;


T_Particle(1) = T_gas;
T_i=T_gas;
m_i=M_gas;
Z=0;
Charge(1)=0;
time=0;
t=2;
Total_time(1)=0;
time_2=0;
time_3=0;
N_H=0;
P_abs=0.11;

%Silicon Surface sites

r_Si=0.21E-9;
vol_Atom=(4/3)*pi*(r_Si^3);
vol_Particle=(4/3)*pi*(a_p^3);
n_atoms=vol_Particle/vol_Atom;
n_sites=(4*(n_atoms^(2/3)));

%Generate intial random numbers

r_1=rand();
r_2=rand();
```

```
r_3=rand();
r_4=rand();
r_5=rand();
r_6=rand();

while time < ((5e-6)-2*dt)

%Particle potential

Vp=-Z*e/(4*pi*epsilon_0*a_p);
n_e=n_i-Z*n_p;

lambda_De=sqrt((epsilon_0*kb*T_e)/((e^2)*n_e));
lambda_Di=sqrt((epsilon_0*kb*T_gas)/((e^2)*n_i));
lambda_DL=sqrt(1/((1/lambda_De^2)+(1/lambda_Di^2)));

R_0=(e*abs(Vp)*a_p*(1+(a_p/lambda_DL)))/(((3/2)*kb*T_gas)+
                                        (e*abs(Vp)*(a_p/lambda_DL)));
lambda_i=(kb*T_i)/(P*sigma_i);
D_i=((3*pi)/(16*sqrt(2)))*sqrt((8*kb*T_i)/(pi*m_i))*lambda_i;
mu_i=(e*D_i)/(kb*T_i);


P_0=exp((-alpha*R_0)/lambda_i);
P_1=((alpha*R_0)/lambda_i)*exp((-alpha*R_0)/lambda_i);
P_2=1-P_0-P_1;



if Vp >= 0

   v_i_oml=pi*(a_p^2)*n_i*sqrt((8*kb*T_i)/(pi*m_i))*(1+((e*abs(Vp))/(kb*T_i)));
   v_i_cec=(1/4)*n_i*4*pi*(R_0^2)*sqrt((8*kb*T_gas)/(pi*M_gas));
   v_i_cont=4*pi*(a_p)*n_i*mu_i*abs(Vp);

   v_i=P_0*v_i_oml+P_1*v_i_cec+P_2*v_i_cont;
```

```
else

    v_i_oml=pi*(a_p^2)*n_i*sqrt((8*kb*T_i)/(pi*m_i))*(1+((e*abs(Vp))/(kb*T_i)));
    v_i_cec=(1/4)*n_i*4*pi*(R_0^2)*sqrt((8*kb*T_gas)/(pi*M_gas));
    v_i_cont=4*pi*(a_p)*n_i*mu_i*abs(Vp);

    v_i=P_0*v_i_oml+P_1*v_i_cec+P_2*v_i_cont;

end


if -e*Vp >= 0

    %v_e=pi*(a_p^2)*n_e*sqrt((8*kb*T_e)/(pi*m_e))*(1-((e*abs(Vp))/(kb*T_e)));
    v_e=pi*(a_p^2)*n_e*sqrt((8*kb*T_e)/(pi*m_e))*exp(-e*abs(Vp)/(kb*T_e));

else

    %v_e=pi*(a_p^2)*n_e*sqrt((8*kb*T_e)/(pi*m_e))*(1-((e*abs(Vp))/(kb*T_e)));
    v_e=pi*(a_p^2)*n_e*sqrt((8*kb*T_e)/(pi*m_e))*exp(-e*abs(Vp)/(kb*T_e));
end

%Charging

dt_charge=-log(r_1)/(v_e+v_i);

if time_2 < dt_charge

    G_1=0;
    time_2=time_2+dt;

else

    if r_2 > abs(v_e/(abs(v_e+v_i)))
```

```
    G_1=15.76*e;                        %Collision with ion
    Z=Z-1;

    else

    Z=Z+1;                              %Collision with electron
    G_1=0;

    end

    time_2=0;
    r_1=rand();
    r_2=rand();

end

%Hydrogen

v_h=(1/4)*n_H*4*pi*((a_p)^2)*sqrt((8*kb*T_gas)/(pi*m_H));

dt_hydrogen=-log(r_3)/v_h;

f_s=N_H/(2*round(n_sites));

if time_3 < dt_hydrogen

    G_2=0;
    G_3=0;
    time_3=time_3+dt;

else

    r_3=rand();
    r_4=rand();
    r_5=rand();
    r_6=rand();
```

```
if r_4 > f_s

N_H=N_H+1;
G_2=3.1*e;
G_3=0;

else

    if r_5 < P_abs

    N_H=N_H-1;
    G_3=1.41*e;
    G_2=0;



    else

    E_D=0.1*e;
    D_0=2.27E-8;
    D=D_0*exp(-E_D/(kb*T_Particle(t-1)));

        if f_s>=1

            L_D=1E30;

        else

            L_D=0.5*(1.48E-10)/(1-f_s);

        end

        v_D=D/(L_D^2);
        tau_d=-log(r_6)/v_D;
```

```
            if tau_d < dt_hydrogen

            N_H=N_H+1;
            G_2=3.2*e;
            G_3=0;

            else

            N_H=N_H;
            G_2=4.51*e;
            G_3=0;

    end

    end

    end

    time_3=0;

end

%Hydrogen desorption due to high temperatures
%Arrhenius function

k_hydrogen(t)=(2.2E12)*exp(-(1.86*1.6E-19)/(kb*T_Particle(t-1)))
                                                  *(f_s*2*n_sites)*dt;

N_H=N_H-2*round(k_hydrogen(t));
f_s=N_H/(2*round(n_sites));
L_2=2*round(k_hydrogen(t))*1.69*e;

%Calculate Temperature

G(t)=G_1+G_2+G_3;
```

```
L(t)=(1/4)*n_gas*(4*pi*(a_p)^2)*sqrt((8*kb*T_gas)/(pi*M_gas))*(3/2)*kb*
          (T_Particle(t-1)-T_gas)*dt;

delta_T(t)=((G(t)-(L(t))))/(((4/3)*pi*(a_p^3)*ro_p*C));

%Individual components

delta_T_Ion(t)=G_1/(((4/3)*pi*(a_p^3)*ro_p*C));
delta_T_H(t)=(G_2+G_3)/(((4/3)*pi*(a_p^3)*ro_p*C));
delta_T_Loss(t)=-L(t)/(((4/3)*pi*(a_p^3)*ro_p*C));

T_Particle(t)=T_Particle(t-1)+delta_T(t);

time=time+dt;
Total_time(t)=time;
Charge(t)=Z;
H_Coverage(t)=f_s;
t=t+1;
test(t)=v_i;

Heat_EI=Heat_EI+G_1;
Heat_H=Heat_H+G_2+G_3;
Heat_Total=Heat_EI+Heat_H;

end

T_Particle_2=T_Particle';
Total_Time_2=Total_time';
Charge_2=Charge';
Ion_current=test';

save T_Particle.txt T_Particle_2 -ascii
save Charge.txt Charge_2 -ascii
save Time.txt Total_Time_2 -ascii
save IC.txt Ion_current -ascii
```